

~~COMPLIMENTARY COPY~~

AUSTRALIAN JOURNAL OF PHYSICS

VOLUME 13, NUMBER 2, JUNE 1960

REGISTERED IN AUSTRALIA FOR TRANSMISSION BY POST AS A PERIODICAL

AUSTRALIAN JOURNAL OF PHYSICS

Published by the Commonwealth Scientific and Industrial Research Organization. Volumes 1 to 5 of the Australian Journal of Physics and the Australian Journal of Chemistry issued as the Australian Journal of Scientific Research, Series A : Physical Sciences. Issued quarterly, £2 per annum.

BOARD OF STANDARDS

The Board of Standards for this Journal is appointed by the Commonwealth Scientific and Industrial Research Organization and the Australian Academy of Science and consists of Professor Sir Macfarlane Burnet (Chairman), Dr. N. S. Noble (Editor), Professor N. S. Bayliss, Dr. J. L. Pawsey, Professor W. P Rogers, and Professor J. S. Turner.

ADVISORY COMMITTEE

Acceptance of papers for this Journal is in the hands of an Advisory Committee appointed by the Board of Standards in consultation with the Institute of Physics (Australian Branch) and consisting of Dr. N. S. Noble (Chairman and Editor), Dr. G. H. Briggs, Emeritus Professor L. G. H. Huxley, Dr. J. L. Pawsey, and Professor H. C. Webster.

OTHER JOURNALS PUBLISHED BY C.S.I.R.O.

| | | |
|--|---|---|
| Australian Journal of Chemistry | } | Issued quarterly, £2 per annum |
| Australian Journal of Biological Sciences | | |
| Australian Journal of Applied Science | | |
| Australian Journal of Agricultural Research | } | Issued six times a year, £2 per annum |
| Australian Journal of Marine and Freshwater Research | | |
| Australian Journal of Botany | } | Not issued at regular intervals, 10/- per issue |
| Australian Journal of Zoology | | |

The Organization is a signatory to the Fair Copying Declaration, details of which may be obtained from the office of the Royal Society, London.

All enquiries and manuscripts should be forwarded to :

The Editor,
Australian Journal of Physics,
Commonwealth Scientific and Industrial Research Organization,
314 Albert Street, East Melbourne, C.2, Victoria

MELBOURNE

MEASUREMENTS OF $n\gamma$ COINCIDENCES IN THE REACTION
 $^{10}\text{B}(d,n\gamma)^{11}\text{C}$ [†]

By J. A. McDONELL,[‡] D. G. SARGOOD,[‡] J. R. MORONEY,[‡] and
J. R. PRESCOTT[§]

[Manuscript received February 29, 1960]

Summary

The energies of some neutron groups leading to low excited states of ^{11}C in the reaction $^{10}\text{B}(d,n\gamma)^{11}\text{C}$ have been measured. These lead to values of 4.3 ± 0.3 MeV and 6.53 ± 0.02 MeV for the energies of the second and fourth excited states respectively. γ -Ray spectra have also been studied in coincidence with different neutron groups. Ground state transitions were observed from the second, third, and fourth excited states, together with cascade decays of the fourth excited state through each of the second and third. Deductions from these γ -ray spectra considerably reduce the number of spin possibilities which have been found for these levels by other workers.

I. INTRODUCTION

A good deal of information about the energy levels of a nucleus can be obtained from the observation of γ -ray transitions between such levels. In the case of ^{11}C , the parities of the first few levels are known, and measurements of the relative intensities of the possible γ -ray transitions between these levels make it possible to deduce the most probable multipolarities of the γ -rays and hence to select the most probable spin values from the many alternatives which have been provided from other measurements.

The current knowledge regarding the energies, spins, and parities of the levels of ^{11}C is listed fully in the compilation of Ajzenberg-Selove and Lauritsen (1959), and the information relevant to the work described in this paper is reproduced, together with the equivalent data on the mirror nucleus ^{11}B , in Figure 1. The parities of all these levels are known to be odd from the $l_p=1$ stripping patterns found by Cerineo (1956) and Maslin, Calvert, and Jaffe (1956) for the neutron groups in the reaction $^{10}\text{B}(d,n)^{11}\text{C}$. These stripping data also restrict the spins of all these levels to $3/2$, $5/2$, $7/2$, or $9/2$, and in the case of the ground state, the β^+ decay evidence restricts the spin to $1/2$, $3/2$, or $5/2$. The value $3/2$ is considered the most likely, this being the spin of the ^{11}B ground state.

Apart from the 2 MeV γ -ray from the first excited state, the only γ -rays which have been observed from ^{11}C are those observed by Bent *et al.* (1955) and Sample *et al.* (1955) in the presence of all other γ -rays following the deuteron bombardment of ^{10}B , and the only certain assignment is the ground state

[†] Supported in part by a grant from the Australian Atomic Energy Commission.

[‡] Physics Department, University of Melbourne.

[§] Australian Atomic Energy Commission; present address: University of British Columbia, Vancouver.

transition from the 6.50 MeV state. In the work to be described below, the spectra of γ -rays involved in the decay of individual levels are examined separately, their observation being in coincidence with the emission of selected neutron groups in the $^{10}\text{B}(d,n\gamma)^{11}\text{C}$ reaction.

The situation in the mirror nucleus, ^{11}B , where the ground state spin is known to be $3/2^-$, is a little clearer. The $l_n=1$ stripping patterns found by Evans and Parkinson (1954) in the reaction $^{10}\text{B}(d,p)^{11}\text{B}$ place the same restrictions on the spins and parities of the low levels of ^{11}B as the $l_p=1$ patterns did in the case of ^{11}C , but these spin possibilities have been considerably reduced in most cases by the angular distribution and angular correlation measurements of Thirion (1953),

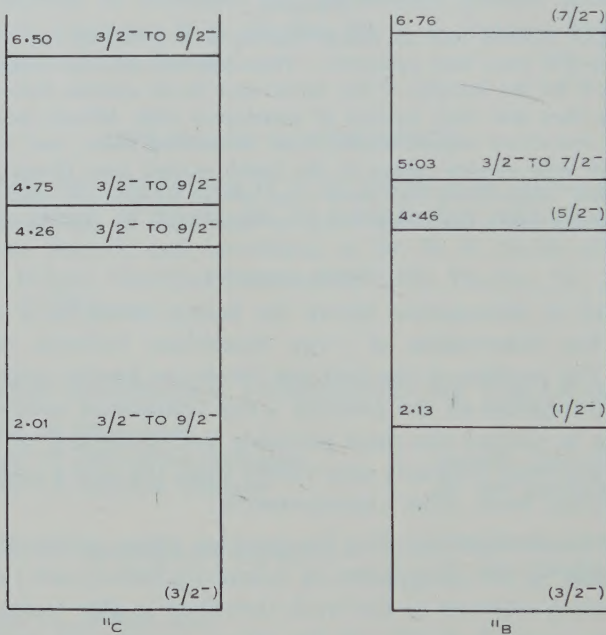


Fig. 1.—Accumulated data concerning the energies and spins of excited states of ^{11}C and ^{11}B .

Bair, Kington, and Willard (1955), and Ferguson *et al.* (1958). Of particular interest is the conclusion that the spin of the 2.13 MeV level is $1/2$, in agreement with the intermediate coupling model, but in contradiction to the $l_n=1$ stripping data, the contradiction being resolved by Wilkinson (1957) by postulating spin flip stripping. Since the situation in the case of the 2.01 MeV level of ^{11}C is exactly analogous, it would be reasonable to consider spin $1/2$ as a possibility for this level also.

Our experiment concerns only ^{11}C , consisting of measurements on the reaction $^{10}\text{B}(d,n\gamma)^{11}\text{C}$. Two types of measurement have been made: firstly, the energies of the neutron groups were measured by a time-of-flight method, and secondly, the γ -ray spectra in coincidence with the individual neutron groups were observed.

II. EXPERIMENTAL DETAILS

A beam of deuterons from the 750 kV electrostatic generator struck a separated boron target (99 per cent. ^{10}B , supplied by A.E.R.E., Harwell) deposited on a nickel backing. Two target thicknesses were used: 90 $\mu\text{g cm}^{-2}$ for the neutron energy measurements and 260 $\mu\text{g cm}^{-2}$ for the γ -ray measurements. γ -Rays were detected by a NaI(Tl) crystal placed as close as possible to the target and at 90° to the direction of the deuteron beam. This crystal was coupled to an RCA 6342 photomultiplier tube. Two crystal sizes, 1½ in. diameter by 1 in. and 3 in. diameter by 3 in. were used. The neutron detector consisted of a 3 in. diameter by $\frac{3}{4}$ in. thick cylinder of "Pamelon" plastic scintillator (manufactured by Isotope Developments Ltd.) coupled via a "Perspex" light pipe

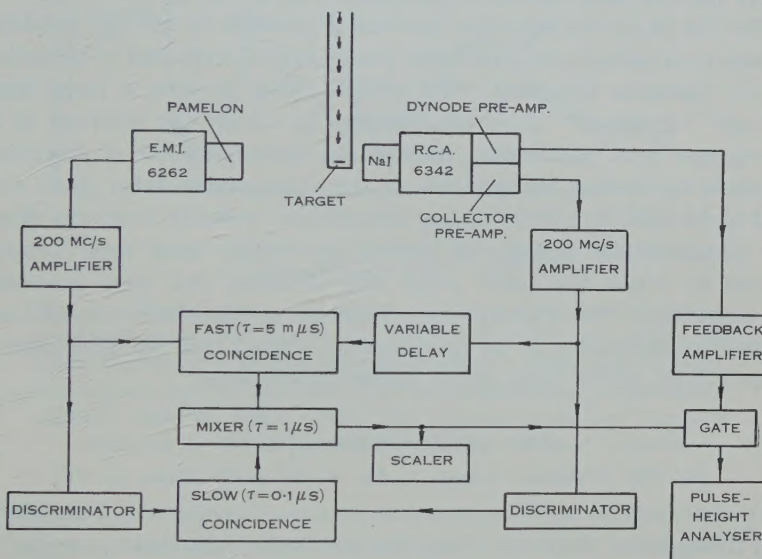


Fig. 2.—Block diagram of delayed coincidence circuit.

to an EMI 6262 photomultiplier. This counter was surrounded by a lead and paraffin wax shield with a collimator defining the directions of the fast neutrons incident on the scintillator. The whole of this assembly could be moved so that both the length and direction of the neutron flight path were easily varied.

While the neutron counter was always located in the horizontal plane containing the incident beam direction, different locations were used for the two NaI(Tl) crystals. The 1½ by 1 in. crystal was placed with its axis in this same horizontal plane but, when the 3 by 3 in. crystal was used, it was located below the target with its axis vertical.

The block diagram (Fig. 2) shows the time-of-flight circuitry. By using the largest recommended value of the high voltage applied to the 6342 photomultiplier and a small (1200Ω) collector load, a pulse from the γ -counter could be obtained which was fast enough to operate the fast coincidence unit (Harwell type 1153A) at its shortest resolving time of $5 \mu\text{s}$. With this arrangement, the delay

distribution used for testing—that obtained with the counters close together and a source of ^{22}Na between them—had a width at half height of 7 m μ s.

The interpretation of a delay distribution for a given neutron flight path requires a knowledge of the location, on the variable delay axis, of the "zero delay" position, i.e. the setting of the variable delay for which pulses from events in the two scintillators that are truly prompt are brought into coincidence. In our case, because of the severe differentiation of the collector pulses from the γ -counter, the rise time of these pulses varied with their magnitude. This resulted in a small variation in the inherent delay of such pulses, so that the zero delay position was dependent on the energies of the γ -rays involved in the coincidences. For this reason, it was not possible to use the position of the peak observed in the test delay distributions taken with a ^{22}Na source as the zero delay position for the (n, γ) coincidences, nor was it possible to use the position of the prompt peak in an actual run, this latter peak being contributed to by coincidences such as $\gamma\gamma$ cascades following $^{10}\text{B}(d,p)^{11}\text{B}^*$ which involve a large range of γ energies, and "inverted" (n, γ) coincidences in which the neutron is detected in the γ -counter and vice versa. Hence the measurements of neutron energy were obtained by finding the position of the appropriate delay peak at various lengths of flight path and determining the neutron velocity from the slope of the resulting distance-time graph, all points on which were then produced by coincidences in which the same γ -ray was involved and were measured with identical circuitry. The discriminator settings in the slow coincidence circuit were chosen to eliminate, as far as possible, events due to coincidences, both random and true, other than those under observation.

III. DELAY DISTRIBUTIONS

(a) The Neutron Group to the 6.50 MeV State of ^{11}C

Delay distributions were measured at neutron directions of 0 and 90° relative to that of the incident deuteron beam and at effective deuteron energies, allowing for a mean energy loss of 20 keV in the target, of 580 and 630 keV. The neutrons of this group are of low energy (about 0.5 MeV) so that the pulses produced by them in the neutron detector were of the same order of size as the noise pulses. Thus the lowest available setting of the discriminator in the neutron channel had to be used. In the γ -channel, the discriminator was set to exclude pulses produced by electrons of energy up to 2 MeV from the ^{128}I activity in the NaI (see Section IV (a)), thereby favouring the detection of coincidences associated with the relatively intense 6.5 MeV radiation (Bent *et al.* 1955). In this way a true-to-random ratio of about 1 was obtained. A typical delay distribution is shown in Figure 3. Figure 4 shows the delay versus distance relationship for one set of delay distributions, and the results obtained from these measurements are shown in Table 1.

(b) The Neutron Group to the 4.26 MeV State of ^{11}C

For the 0° direction and a deuteron energy of 580 keV the neutron groups to the 2.01, 4.26, and 4.75 MeV states of ^{11}C should have energies of approximately 4.9, 2.8, and 2.3 MeV respectively, with the corresponding flight times

per metre of 33, 44, and 48 m μ s. With delay distributions having a width at half height of 10 m μ s, rather long flight paths would be required to resolve these groups. Under these conditions the count rates in our detector would be pro-

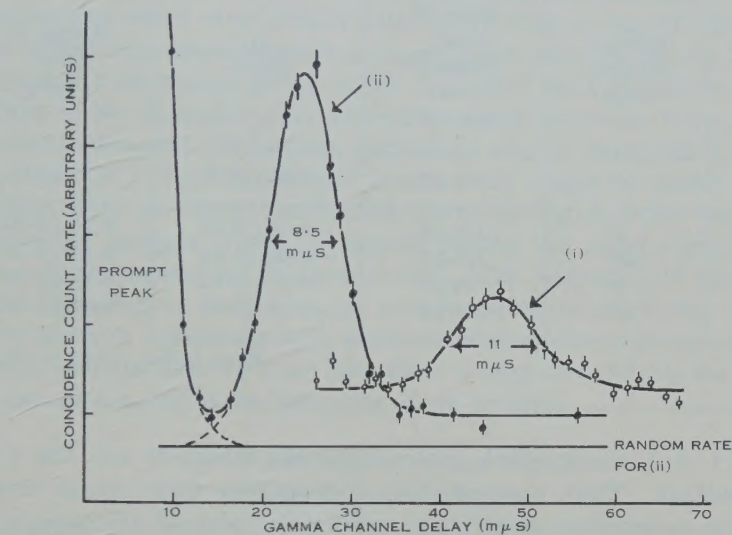


Fig. 3.—Typical delay distributions. Curve (i) neutron group to 6.50 MeV state (90° direction; flight path 33.6 cm). Curve (ii) neutron group to 4.26 MeV state (0° direction; flight path 50.8 cm). The random rate was measured by inserting a large delay in the neutron channel, and the higher count rate at large γ -channel delays is attributed to true coincidences involving scattered neutrons.

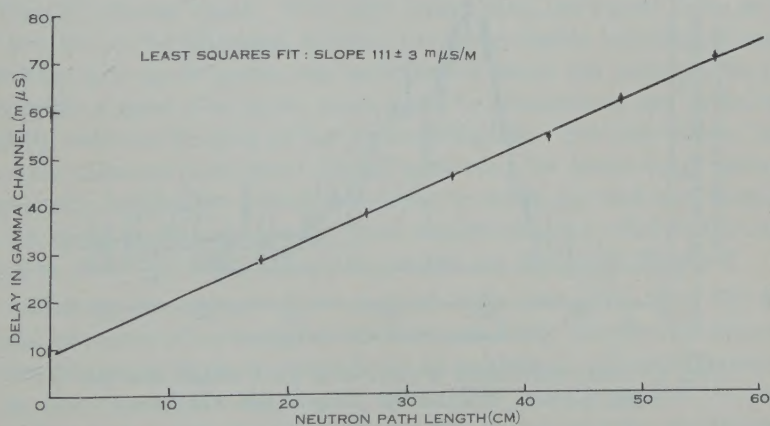


Fig. 4.—Delay $v.$ flight path measurement for neutron group to the 6.50 MeV state (neutron direction 90° ; beam energy 650 keV).

hibitively small for a series of delay distributions of the type hitherto described. However, the neutron yield measurements of Paris and Endt (1954) indicate that at this energy the intensities of the groups in the 0° direction should be in

TABLE I
RESULTS OF DELAY DISTRIBUTION MEASUREMENTS FOR THE SECOND AND FOURTH EXCITED STATES OF ^{11}C

| Deuteron Energy (keV) | Neutron Counter Angle | Slope of Delay-Distance Curve ($\mu\text{s m}^{-1}$) | Q (MeV) | Energy of Level (MeV) |
|-----------------------|-----------------------|--|--------------|-----------------------|
| 580 | 0° | 44 ± 2 | 2.16 ± 0.27 | 4.3 ± 0.3 |
| 580 | 0° | 104 ± 4 | -0.08 ± 0.04 | 6.55 ± 0.04 |
| 580 | 90° | 115 ± 5 | -0.04 ± 0.04 | 6.51 ± 0.04 |
| 630 | 0° | 98 ± 2 | -0.07 ± 0.02 | 6.54 ± 0.02 |
| 630 | 90° | 111 ± 3 | -0.06 ± 0.03 | 6.53 ± 0.03 |

Mean Value : 6.53 ± 0.02

the ratio $6:1:0.3$, the 2.8 MeV group being the strongest and the 4.9 MeV group the weakest. Thus, a set of delay distributions taken under these conditions can be interpreted as giving a reasonable value of the energy of the 4.26 MeV state only.

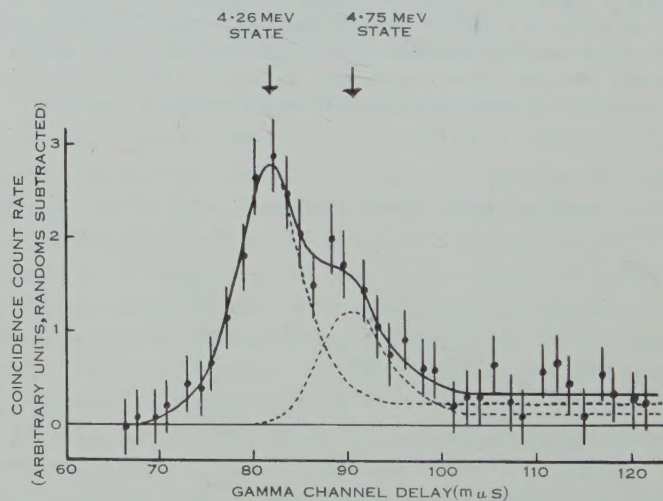


Fig. 5.—Delay distribution of neutrons to the 4.26 and 4.75 MeV states (neutron direction 90°; flight path 171.5 cm).

In this case, the discriminator setting in the neutron channel could be increased to remove noise pulses and also those due to the annihilation radiation of the ^{11}O . The resulting improvement in the true-to-random ratio and in resolution is evident in Figure 3. Table 1 includes the results of the single set of delay distributions made on this group.

(c) *The Neutron Group to the 4.75 MeV State of ^{11}C*

In the interpretation of the coincidence γ -ray spectra (Section IV (c)) it is desirable to have an estimate of the relative intensities of the neutron groups to the 4.26 and 4.75 MeV states. To provide such an estimate, a single delay distribution was taken over a flight path of 171.5 cm in the 90° direction. The angular distribution measurements of Graue (1956) indicate that in this direction the intensity of the weaker group (to the 4.75 MeV state) should be a maximum, while that of the stronger group should be at its minimum value. The result of this measurement (a 30-hr run), performed with a 260 $\mu\text{g cm}^{-2}$ target and a beam current of 0.5 μA at 600 keV bombarding energy, is shown in Figure 5. Comparison with the delay distribution shown in Figure 3 for the (effectively) monoenergetic neutron group of approximately the same energy shows the presence of two unresolved neutron groups. The separation of their two delay peaks is estimated to be $9 \pm 2 \text{ m}\mu\text{s}$, corresponding to an energy difference of $0.5 \pm 0.1 \text{ MeV}$, in agreement with other determinations of the energies of these two levels, and the ratio of their intensities is approximately 2, the group going to the second excited state being the more intense.

IV. COINCIDENCE γ -RAY SPECTRA(a) *Energy Calibration*

The spectra of the γ -rays in coincidence with the various neutron groups were recorded in a 100 channel pulse-height analyser (Sunny type PHA2). Calibration points were obtained from the spectra of the 2.62 MeV γ -ray of ^{208}Pb (from a radiothorium source) and the 4.43 MeV γ -ray of ^{12}C (from a Po-Be source). With the beam striking the target the count rate in the γ -counter was very high, with large contributions from the ^{11}C (20-min half-life) annihilation radiation from the target and the neutron-induced ^{128}I (25-min half-life) activity in the NaI(Tl) crystal itself. This high count rate, estimated to be in excess of 10^5 per sec, had to be tolerated in order to obtain usable coincidence count rates. The resultant pile-up of pulses was sufficient to make the pulse-height resolution of the counter a good deal worse than could be obtained at low count rates, and also slightly reduced the gain of the photomultiplier. For this reason, calibration spectra were taken several times during each run, the beam being removed from the target only for the few minutes required to insert the radioactive sources and record the spectra, so that, under these conditions, the total count rate in the counter was still very high. Typical spectra are shown in Figure 6.

In addition, the energy of the ground state transition from the 6.50 MeV state could be regarded as being known from our delay distribution measurements to a better accuracy than we could hope to achieve in our scintillation spectra. Hence, in the coincidence spectra in which this γ -ray appeared, it provided a further calibration point, obtained during the actual running conditions for the coincidence spectrum. The fact that this point, together with the two obtained from radiothorium and Po-Be, gave a pulse-height versus energy relation which was linear within the experimental accuracy was regarded as a check on the validity of the calibration procedure using the radioactive sources described above.

(b) γ -Rays from the 4.26 MeV Level of ^{11}O

With the neutron counter in the 0° direction and a short flight path, the γ -rays in coincidence with the unresolved neutron groups to the 4.26 and 4.75 MeV states will be principally those due to de-excitation of the second excited state. A spectrum obtained using the small NaI(Tl) crystal is shown in Figure 7. Comparison of this figure with Figure 6 (b) clearly suggests the presence

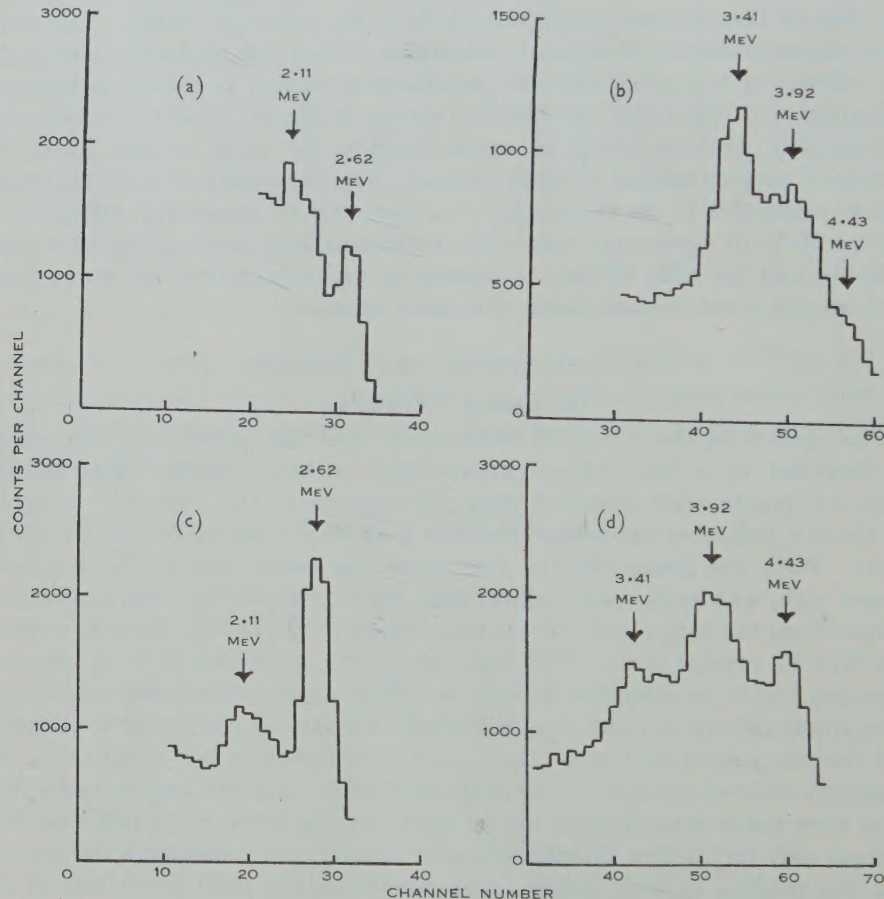


Fig. 6.—Calibration γ -ray spectra. (a) RdTh, 1½ by 1 in. crystal, (b) Po-Be, 1½ by 1 in. crystal, (c) RdTh, 3 by 3 in. crystal, (d) Po-Be, 3 by 3 in. crystal.

of only one γ -ray. The poorer resolution probably results from a combination of the higher count rate and small random drifts in gain during the run. For the runs reported here, no systematic drifts in the calibration spectra were observed, although random drifts of up to ± 1 channel did occur at times.

The main peak in Figure 7 is interpreted as the two-quantum escape peak of a γ -ray of energy 4.2 ± 0.1 MeV, and this is identified as the ground state transition from the 4.26 MeV state. A cascade from this level through the 2.01 MeV state would produce two γ -rays of energy in the vicinity of 2 MeV.

From Figure 7 we conclude that the intensity of any 2 MeV radiation which may be present is less than 10 per cent. of that of the 4.2 MeV γ -ray and hence the transition probability for de-excitation via the 2.01 MeV state is less than 5 per cent. of that for the ground state transition. However, it will be seen, in the following section, that this upper limit may be reduced to $2\frac{1}{2}$ per cent.

(c) γ -Rays from the 4.75 MeV State of ^{11}C

When the neutron counter is in the 90° position, our delay distribution measurements have shown that approximately one-third of the true coincidences in the composite delay peak of the neutron groups to the 4.26 and 4.75 MeV

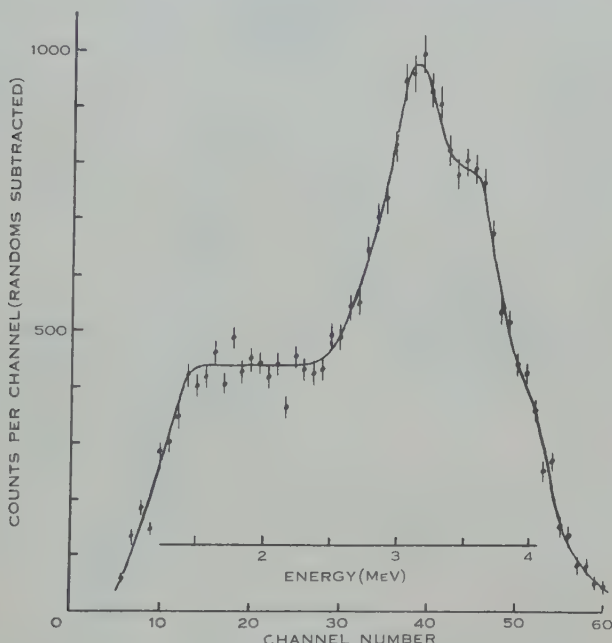


Fig. 7.— γ -Ray spectrum from 4.26 MeV state (small NaI(Tl) crystal).

states are associated with the 4.75 MeV state. Thus the γ -ray spectrum in coincidence with this composite delay peak may provide some information about the de-excitation of this level.

With a short flight path and using the small NaI(Tl) crystal the spectrum shown in Figure 8 was obtained. It is not possible to select either of the two curves shown in this figure as being a better fit to the experimental points than the other and it is clear that very good statistics indeed would be needed to be able to decide between them. Thus, from this measurement we are not able to discover whether or not the 4.75 MeV state is de-excited to any extent by a ground state transition.

A spectrum taken under the same conditions but using the large NaI(Tl) crystal is shown in Figure 9. The "smearing out" of the spectrum from a crystal of this size by the use of a high count rate is clearly seen by reference to

Figure 6 (*d*). It is also apparent from Figure 7 that this effect is less serious in the spectrum from the small crystal, partly due to the lower count rate and partly due to the nature of the latter spectrum in which the two-quantum escape peak is dominant at these energies.

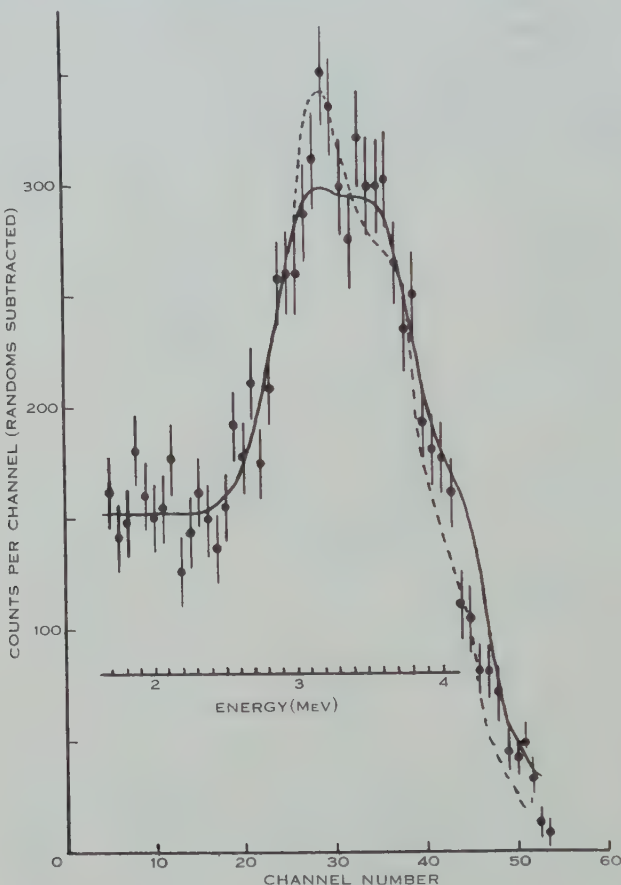


Fig. 8.— γ -Ray spectrum from 4.26 and 4.75 MeV states (small NaI(Tl) crystal). The full curve is the spectrum expected if one-third of the γ -rays were 4.75 MeV and two-thirds 4.26 MeV. The dotted curve is the spectrum for 4.26 MeV alone.

Figure 9 again provides no evidence for or against the presence of a 4.8 MeV γ -ray but does confirm the low intensity of any cascade through the 2.01 MeV state. One could perhaps suggest the presence of a peak having a height of the order of 5 per cent. of that of the main peak in the vicinity of 2 MeV, as shown by the dotted curve in Figure 9, but it would hardly be justified by the statistics of the points in this region. Thus it seems reasonable to set the upper limit for de-excitation of the 4.26 and 4.75 MeV states combined via the 2.01 MeV state as 2½ per cent. of the total probability of de-excitation of these levels either by direct ground state transitions or by cascade from the 4.75 MeV to the 4.26 MeV

state and thence to the ground state. Hence less than about $7\frac{1}{2}$ per cent. of the transitions from the 4.75 MeV excited state alone are from this level direct to the first excited state. However, the measurements provide no information

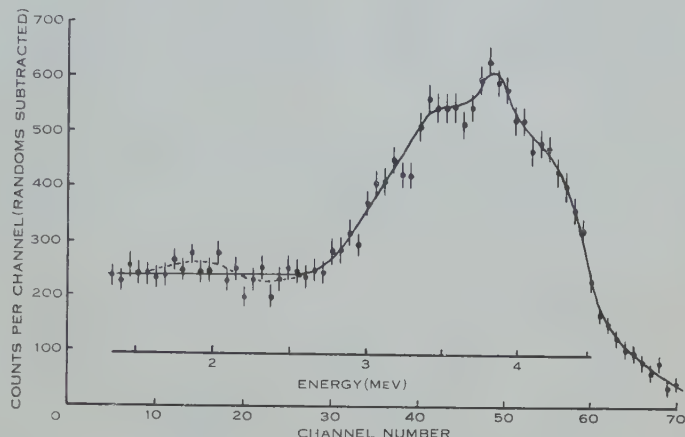


Fig. 9.— γ -Ray spectrum from 4.26 and 4.75 MeV states (large NaI(Tl) crystal).

about the probability of a cascade from the 4.75 MeV to the 4.26 MeV state. It was not possible to obtain any observations of neutrons in coincidence with a 0.5-MeV γ -ray (the first transition in such a cascade) because of the high annihilation radiation background.

TABLE 2
PEAKS IN THE SPECTRA OF γ -RAYS IN COINCIDENCE WITH THE NEUTRON GROUP TO THE FOURTH EXCITED STATE OF ^{11}C (SMALL NaI(Tl) CRYSTAL MEASUREMENTS)

| Peak Energy (MeV) | | | Identification |
|----------------------|----------------|------|--|
| Run 1 | Run 2 | Mean | |
| * | 1.7 (?) | | |
| * | 2.3 ± 0.1 | 2.3 | 2.3 MeV; full energy peak |
| 3.2 ± 0.1 | 3.4 ± 0.1 | 3.3 | 4.3 MeV; double escape peak |
| 3.7 ± 0.1 | 3.9 ± 0.1 | 3.8 | { 4.3 MeV; single escape peak 4.8 MeV; double escape peak |
| 4.3 ± 0.2 | 4.3 ± 0.15 | 4.3 | 4.8 MeV; single escape peak† |
| 6.50 | 6.50 | | 6.50 MeV; double escape peak (calibration point) |

* Spectrum unreliable in this region due to electronic fault.

† Plus a small contribution from the 4.3 MeV full energy peak.

(d) γ -Rays from the 6.50-MeV State

The spectrum of γ -rays in coincidence with the low energy neutron group was observed with both the small and large NaI(Tl) crystals. The small crystal results are shown in Table 2, and one of the small crystal spectra is shown in

Figure 10. It will be seen that there is clear evidence for a cascade of two γ -rays of approximate energies 2.3 and 4.3 MeV. Using the best available level energies as shown in Figure 1, the two possible cascades which might fit this description are

- (i) 4.49 MeV followed by 2.01 MeV, through the first excited state, and
- (ii) 2.24 MeV followed by 4.26 MeV, through the second excited state.

We believe that the accuracy of our γ -ray measurements is sufficient to exclude the first of these possibilities. The peak falling at 2.3 MeV in Figure 10 is well defined and appears at the same energy in the coincidence spectrum obtained with the large NaI(Tl) crystal (Fig. 11). Our energy calibration seems

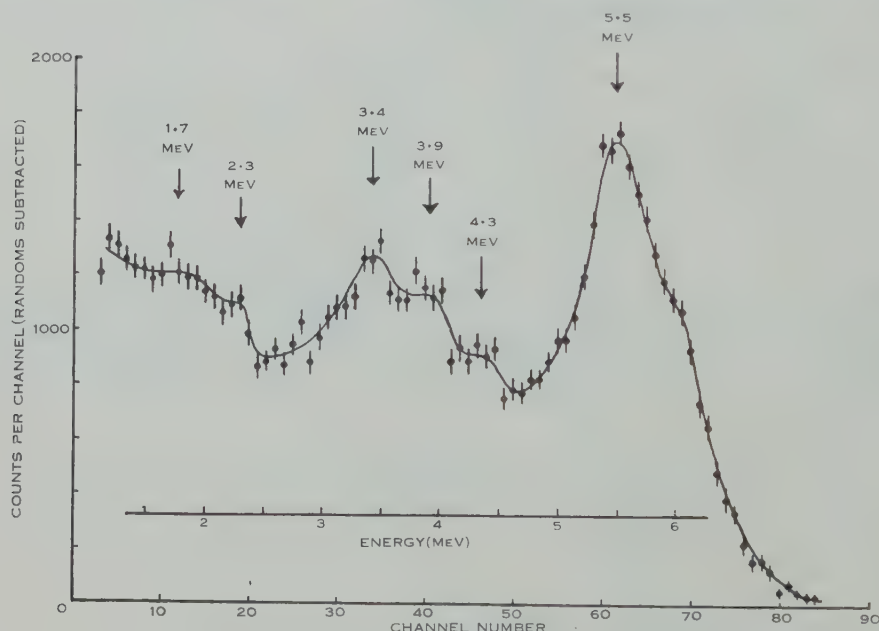


Fig. 10.— γ -Ray spectrum from 6.50 MeV state (small NaI(Tl) crystal).

reliable enough to exclude the possibility that this peak could be due to a 2.0 MeV γ -ray. In the same way, the peaks in the middle energy range cannot be fitted to a 4.5 MeV γ -ray, particularly in view of the proximity of our 4.43 MeV calibration points. Thus it seems that the predominating cascade from the fourth excited state is via the second excited state, and that the probability of occurrence of this cascade is somewhat less than, but of the same order of magnitude as that of the direct ground state transition.

There is also evidence, more particularly from the small crystal spectra, for the presence of a 4.8 MeV γ -ray, corresponding to the 4.75 MeV ground state transition from the third excited state. The main evidence for this is the presence of the peak at 4.3 MeV which is identified as the one-quantum escape peak of a 4.8 MeV γ -ray. Comparison with Figure 7 indicates that a 4.3 MeV γ -ray

would not produce such a full energy peak. The lack of structure in the 3–5 MeV region of the large crystal spectrum precludes any definite identification of a 4.8 MeV γ -ray in this case. There is some evidence in both the small and large crystal spectra for the presence of a 1.75 MeV γ -ray which must precede the 4.75 MeV transition. However, the spectra in this region cannot be regarded as very reliable since, in order to obtain pulses of this magnitude, the necessary

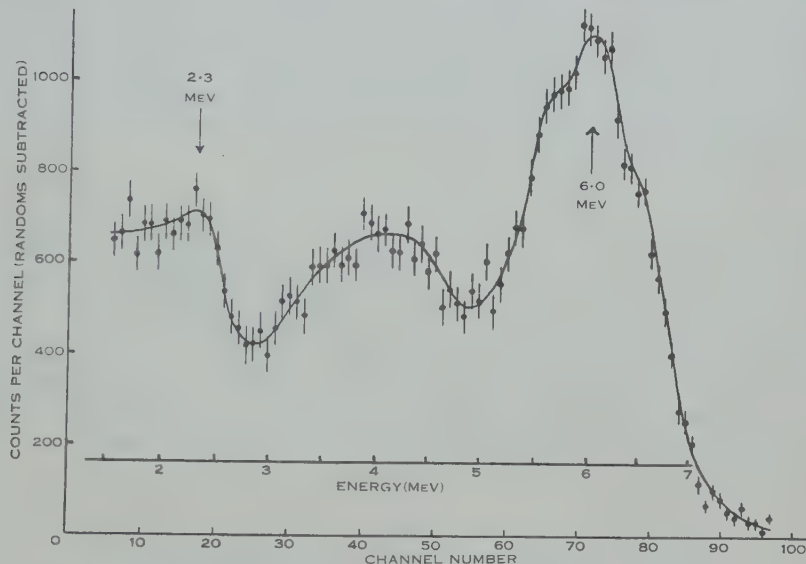


Fig. 11.— γ -Ray spectrum from 6.50 MeV state (large NaI(Tl) crystal).

discriminator setting in the γ -channel was low enough to admit a large number of background pulses from the ^{128}I activity in the crystal. Hence the absence of a sharp peak at 1.75 MeV cannot be taken as definite evidence against the presence of a 1.75 MeV γ -ray.

From these coincidence γ -ray spectra we conclude that the principal γ -ray transitions between the low-lying levels of ^{11}C are those shown in Figure 12 below.

V. DISCUSSION

(a) Energies of Excited States of ^{11}C

Our time-of-flight measurement of the energy of neutrons to the 6.50 MeV state of ^{11}C is our most precise estimate of the excitation energy of an ^{11}C level. Our value of 6.53 ± 0.02 MeV is in agreement with the values of 6.50 ± 0.03 MeV found by Bent *et al.* (1955), and 6.52 ± 0.05 MeV by Sample *et al.* (1955), from γ -ray energy measurements, but is not in agreement with the value of 6.40 ± 0.04 MeV found by both Johnson (1952) and Cerineo (1956) from measurements of the energy of this same neutron group, using photographic plates, nor with the value of 6.476 ± 0.020 MeV found by Neilson, Dawson, and Johnson (1959), also using a time-of-flight technique, although the disagreement, in this case, is not large. The accuracy of our determination depends only on the

accuracy of measurement of the neutron flight path and of calibration of the variable delay. Flight paths could be readily measured to better than 0.5 per cent. and the variable delay was known at all settings to within 0.5 m μ s, by comparison with the period of a BC221 oscillator. We have been unable to detect any systematic error in our measurements to account for these discrepancies between our result and those of other workers.

The other estimates of excitation energies from our results are the value of 4.2 ± 0.1 MeV for the 4.26 MeV state, from a γ -ray measurement, and an energy difference of 0.50 ± 0.05 MeV between the 4.26 and 4.75 MeV states from a delay distribution of neutrons. Both of these values are in agreement with those given by Ajzenberg-Selove and Lauritsen (1959), but are not sufficiently precise to influence their values in any way.

(b) γ -Rays

Since the transition probabilities for the γ -rays observed are not among those calculated by Kurath (1957) on the intermediate coupling model, we have been tempted to apply the cruder estimates of Weisskopf (1951) to find the most probable multipolarities of the observed transitions. In doing this we have been encouraged by the work of Lane and Radicati (1954) on $A=13$ nuclei, which showed that the intermediate coupling and experimental values of the transition probabilities differed from the Weisskopf estimates by a factor of only about 10. Table 3 lists the Weisskopf transition probabilities of interest.

TABLE 3
WEISSKOPF ESTIMATES FOR TRANSITION PROBABILITIES IN ^{11}C

| E (MeV) | $T(M1)$ (sec $^{-1}$) | $T(E2)$ (sec $^{-1}$) | $T(M3)$ (sec $^{-1}$) |
|--------------|---------------------------|---------------------------|---------------------------|
| 0.5 | 5×10^{12} | 10^8 | 4 |
| 1.75 | 2×10^{14} | 6×10^{10} | 3×10^4 |
| 2.25 | 4×10^{14} | 2×10^{11} | 2×10^6 |
| 2.74 | 7×10^{14} | 6×10^{11} | 6×10^5 |
| 4.26 | 3×10^{15} | 5×10^{12} | 10^7 |
| 4.75 | 4×10^{15} | 9×10^{12} | 3×10^7 |
| 6.50 | 10^{16} | 5×10^{13} | 3×10^8 |

Since the $l_p=1$ stripping patterns fix the parities of the ground and first four excited states of ^{11}C as odd, the only possible multipole transitions to be observed between these levels are $M1$, $E2$, and $M3$. $E4$ and higher order multipoles have mean lives too long to be observed by our technique.

The comparable intensities of the 6.5 MeV and 1.75 or 2.25 MeV γ -rays in the decay of the 6.50 MeV state is readily accountable if, and only if, the 6.5 MeV transition is $E2$ and the lower energy transition $M1$, particularly since at least some $E2$ enhancement is to be expected. Now in Section I it was pointed out that the most likely value of the ground state spin is $3/2$; this value will be assumed throughout the following discussion. In this case the spin of the

6.50 MeV state would be $7/2^-$ which is the assignment given by Ferguson *et al.* (1958) to the corresponding level in ^{11}B . The possibility that the 6.5 MeV γ -ray is *M1* or *M3* is very remote in view of the comparable intensity of the lower energy component.

The existence of the 2.3 and 4.8 MeV γ -rays in this decay scheme would indicate that both the 1.75 and 2.25 MeV transitions occur, and, since both would have to be *M1* to compete with the 6.5 MeV *E2* transition, the spins of the 4.75 and 4.26 MeV states would be restricted to $5/2$, $7/2$, or $9/2$. Also, if both the 4.75 and 4.26 MeV ground state transitions are observed they cannot be *M3*, since this would correspond to a mean life of about 50 m μ s which would

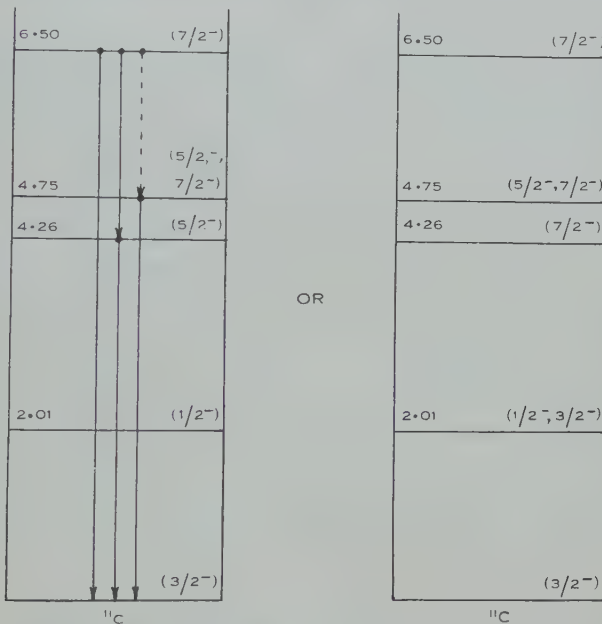


Fig. 12.—Spin assignments for low excited states of ^{11}C .

have shown up as a considerable distortion of the delay peaks. This would then eliminate $9/2$ as a possible spin for either the 4.75 or 4.26 MeV levels. While the presence of the 4.26 MeV γ -ray is certain, so that for this case these conclusions are valid, the evidence for the 4.75 MeV γ -ray is certainly less strong. However, it should be noted that the absence of this γ -ray would not affect the argument as to the spin of any level other than that at 4.75 MeV.

The absence of any evidence in the decay scheme of the 6.50 MeV level for a cascade through the 2.01 MeV level suggests that this transition, if it occurs, is not *M1*, and consequently that the spin of the 2.01 MeV level is not $5/2$, $7/2$, or $9/2$. However, the expected intensity for *E2* or *M3* is so low that neither of these would be observed, and so spin values of $1/2$ or $3/2$ are possible. If the spin of this level is $3/2$ then the 4.26 MeV and possible 2.25 MeV transitions in the decay of the 4.26 MeV state would be both *M1* or both *E2*. Since an upper

limit of $2\frac{1}{2}$ per cent. is placed on the intensity of the 2.25 MeV component relative to the 4.26 MeV component, and the theoretical relative intensities for $M1$ and $E2$ transitions are 1/10 and 1/20 respectively, it is unlikely that both are $M1$, but both $E2$ is possible; i.e. if the 2.01 MeV state is $3/2^-$, then the 4.26 MeV state would be $7/2^-$. However, if the 2.01 MeV state is $1/2^-$ then the 4.26 MeV state could be $5/2^-$ or $7/2^-$, the unobserved 2.25 MeV transition being of higher multipole order than the 4.26 MeV transition in either case. Thus a spin of $7/2^-$ for the 4.26 MeV state may be associated with $1/2^-$ or $3/2^-$ for the 2.01 MeV state, while $5/2^-$ for the 4.26 MeV state is associated with only $1/2^-$ for the 2.01 MeV state. All these spin conclusions are summarized in Figure 12, in which are also shown the γ -ray transitions observed (firm lines) and inferred (dotted line).

In conclusion, it is interesting to note the extent to which the spin values found here for ^{11}C agree with those found for ^{11}B and those predicted by the intermediate coupling model. The assignment of $1/2^-$ for the first excited state in ^{11}B seems fairly definite, while $5/2^-$ and $7/2^-$ for the second and fourth excited states respectively are found by Ferguson *et al.* (1958). Our results are in complete agreement with these assignments, but in the third excited state there is an anomaly. Ferguson *et al.* (1958) have observed a 12 per cent. decay of the third excited state through the first, from which they conclude spin $3/2^-$ for the third state. However, Wilkinson and Alburger (1959) are unable to reconcile a spin value of less than $5/2^-$ for this level with their measurements on the β decay of ^{11}Be . Our results for ^{11}C make a spin of $3/2^-$ for the third excited state of ^{11}C seem unlikely also. The intermediate coupling model requires spins of $5/2^-$ and $7/2^-$ for the second and third excited states (or vice versa), and whilst Wilkinson and Alburger's results for ^{11}B and also our results for ^{11}C are in accord with this requirement, it has not yet been shown whether the model is capable of predicting the $E2$ enhancement necessary to account for the cascade through the first excited state observed by Ferguson *et al.*

VI. ACKNOWLEDGMENTS

The authors wish to thank Professor Sir Leslie Martin for his interest in this work. They would also like to make particular mention of the assistance given by Ghias-ud-Din and Mr. G. M. Bailey in the early stages of the project.

VII. REFERENCES

- AJZENBERG-SELOVE, F., and LAURITSEN, T. (1959).—*Nuclear Phys.* **11**: 1.
- BAIR, J. K., KINGTON, J. D., and WILLARD, H. B. (1955).—*Phys. Rev.* **100**: 21.
- BENT, R. D., BONNER, T. W., McCRARY, J. H., RANKEN, W. A., and SIPPET, R. F. (1955).—*Phys. Rev.* **99**: 710.
- CERINEO, M. (1956).—*Physica* **22**: 1154A.
- EVANS, N. T. S., and PARKINSON, W. C. (1954).—*Proc. Phys. Soc. A* **67**: 684.
- FERGUSON, A. J., GOVE, H. E., KUEHNER, J. A., LITHERLAND, A. E., ALMQVIST, E., and BROMLEY, D. A. (1958).—*Phys. Rev. Letters* **1**: 414.
- GRAUE, A. (1956).—*Phil. Mag.* **1**: 1027.
- JOHNSON, V. R. (1952).—*Phys. Rev.* **86**: 302.
- KURATH, D. (1957).—*Phys. Rev.* **106**: 975.
- LANE, A. M., and RADICATI, L. A. (1954).—*Proc. Phys. Soc. A* **67**: 167.

- MASLIN, E. E., CALVERT, J. M., and JAFFE, A. A. (1956).—*Proc. Phys. Soc. A* **69** : 754.
NEILSON, G. C., DAWSON, W. K., and JOHNSON, F. A. (1959).—*Rev. Sci. Instrum.* **30** : 963.
PARIS, C. H., and ENDT, P. M. (1954).—*Physica* **20** : 585.
SAMPLE, J. T., NEILSON, G. C., CHADWICK, G. B., and WARREN, J. B. (1955).—*Canad. J. Phys.* **33** : 828.
THIRION, J. (1953).—*Ann. Phys., Lpz.* **8** : 489.
WEISSKOPF, V. F. (1951).—*Phys. Rev.* **83** : 1073L.
WILKINSON, D. H. (1957).—*Phys. Rev.* **100** : 666.
WILKINSON, D. H., and ALBURGER, D. E. (1959).—*Phys. Rev.* **113** : 563.

ALPHA-PARTICLES FROM THE REACTION ${}^7\text{Li}(p,\gamma){}^8\text{Be}^*(\alpha){}^4\text{He}$

By D. S. GEMMELL†

[*Manuscript received February 5, 1960*]

Summary

The α -particle spectrum from the reaction ${}^7\text{Li}(p,\gamma){}^8\text{Be}^*(\alpha){}^4\text{He}$ has been determined in coincidence with γ -rays. The results indicate that, apart from the broad 2.9 MeV level, there are no additional levels between the ground state and 7 MeV with intensities greater than 3 per cent. of the 2.9 MeV level. It is shown that the shape of the 2.9 MeV level can be fitted satisfactorily by a dispersion formula if a large value for the reduced width of the level is assumed.

I. INTRODUCTION

Several states in ${}^8\text{Be}$ at excitations up to 15 MeV have been reported by various observers; but, so far, the only ones which seem to be present with any degree of certainty (Ajzenberg and Lauritsen 1959) are the narrow 0^+ ground state ($\Gamma \sim 5$ eV), the broad 2^+ level at 2.9 MeV ($\Gamma \sim 1.2$ MeV), and a broad 4^+ level at 11.6 MeV ($\Gamma \sim 6.7$ MeV). These levels correspond well with the only three states expected in this region of excitation on the basis of either a simple shell model or an α -particle model of ${}^8\text{Be}$.

Nevertheless, the evidence for other even states in ${}^8\text{Be}$ at 4.1, 5.3, and 7.5 MeV is considerable (Titterton 1954; Ajzenberg and Lauritsen 1955), and it was with a view to obtaining further evidence on the possible existence of these levels that the present experiment was performed.

II. APPARATUS

Alpha-particles from the 441 keV resonance in the ${}^7\text{Li}(p,\gamma){}^8\text{Be}^*(\alpha){}^4\text{He}$ reaction were detected in coincidence with γ -rays using the apparatus shown in Figure 1. A 20 keV thick target of separated ${}^7\text{Li}$ on a water-cooled copper backing was bombarded by a collimated beam of 450 keV protons from the Canberra 600 keV Cockcroft-Walton accelerator. The α -particles were detected at 90° to the proton beam by a $1\frac{1}{8}$ by $\frac{1}{2}$ in. CsI crystal which had been thinned down to 0.005 in. in order to avoid an excessive background count arising from the passage of high energy electrons. To reach this detector, α -particles from the target had to pass through a slit 1 mm wide, after which they were deflected by a magnetic field of 5400 G produced by a set of six permanent magnets of the magnetron type. The purpose of the magnetic field was to prevent the intense 8.8 MeV α -particle group from the ${}^7\text{Li}(p,\alpha){}^4\text{He}$ reaction, and also direct light from the target, from reaching the detector. Furthermore, scattered protons were sufficiently deflected not to reach the crystal. To protect the phototube

† Research School of Physical Sciences, Australian National University, Canberra.

from the stray field of these magnets it was necessary to introduce a 7 in. long by 1½ in. diameter "Perspex" light pipe and to surround the cathode end of the phototube with a soft-iron shield.

The γ -ray detector used was a 5 in. diameter by 4 in. long NaI(Tl) crystal coupled to an EMI 6099 phototube. This crystal was placed opposite the α -particle counter and adjacent to the "Perspex" window shown in Figure 1.

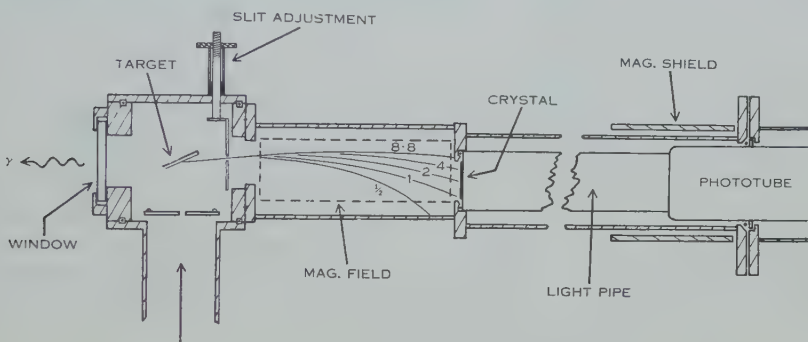


Fig. 1.—Diagram of apparatus.

III. EXPERIMENTAL

Pulses from the two detectors were fed through amplifiers into a Garwin-type coincidence unit (Garwin 1950) with a resolving time of 0.1 μsec , which responded to γ -ray pulses of greater than 4 MeV, and α -particle pulses of greater than $\frac{1}{2}$ MeV. The output from this unit was used to operate the gate circuit in a 70 channel Sunvic kicksorter, thus enabling the coincident α -particle spectrum to be determined. To avoid the effects of deterioration in the target after prolonged bombardment the target backing was moved slightly every 2 hr so that the beam struck an unused section. The procedure adopted was to run for an hour and then obtain a background count under the same conditions by inserting a 2.4 μsec delay in the γ -ray channel. Then the target was raised and, before the next run, the gain of the α -counter checked by moving the slit inwards a short distance and determining the pulse height of the 8.8 MeV α -particles from the $^7\text{Li}(p,\alpha)^4\text{He}$ reaction. In all, seven separate targets were used and the final result comprises spectra recorded over a total bombardment time of 82 hr using a beam current of 5 μA . Except at very low α -particle energies the background count was small compared to the total number of coincidences and the resultant spectrum obtained after subtraction of this background is shown in Figure 2.

The calibration of the α -particle energy scale was determined by substituting a ThC" α -source for the target and recording the spectra obtained when various thicknesses of aluminium foil were interposed between the source and the slit. In this way it was also possible to determine the resolution of the α -particle counter as a function of α -particle energy. The use of a long light pipe limited the resolution obtainable, which was found to vary between 25 per cent. at $E_\alpha=1$ MeV and 15 per cent. at $E_\alpha=4$ MeV. The detection efficiency of the crystal was constant between these limits of α -particle energy.

IV. RESULTS

A statistical analysis of the data in Figure 2 indicates that no additional levels with widths less than 0.5 MeV are present in ${}^8\text{Be}$ at excitations between 2 and 7 MeV with intensities of more than 3 per cent. of the total number of excited ${}^8\text{Be}$ nuclei.

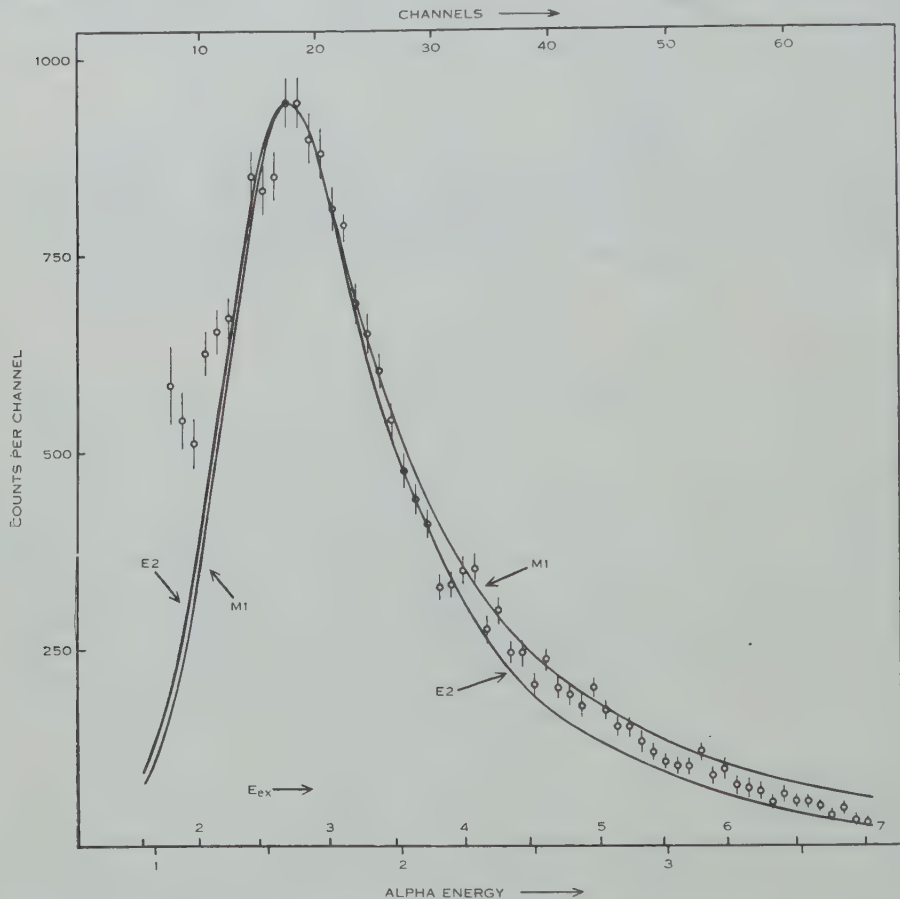


Fig. 2.—Coincident α -particle spectrum with background subtracted. The full curves are theoretical fits to the data, assuming $M1$ and $E2$ radiation is involved.

The 2.9 MeV state appears to have a significant high energy tail, and an attempt was made to account for this by fitting the data with a Wigner-Eisenbud single-level dispersion formula (Wigner and Eisenbud 1947) of the form

$$N(E) = \text{const.} \frac{[17.6 - E]^{2l+1} \Gamma(E)}{[E_0 + \Delta(E) - E]^2 + [\Gamma(E)/2]^2},$$

where E is the energy of excitation in ${}^8\text{Be}$ and E_0 is a constant. The first term in the numerator of this expression is proportional to the probability of γ -ray transitions from an initial state at 17.6 MeV to a final state at E MeV ($l=1$ for magnetic dipole and $l=2$ for electric quadrupole radiation). The variation of

the functions Γ and Δ with energy cannot be neglected in such a broad resonance at low excitation (Thomas 1951). Both Γ and Δ were calculated from tables of Coulomb wave-functions (Bloch *et al.* 1951) assuming a value of the ${}^8\text{Be}$ radius of 4.48×10^{-13} cm (Christy and Latter 1948). In order to fit the data it was necessary to assume in these calculations a value for the reduced width of $\gamma = 11.9 \times 10^{-13}$ MeV cm and a value of $E_0 = 5.95$ MeV. By using these values and by numerically folding the experimental resolution into the theoretical curves (a small correction in such a broad peak) the two curves shown in Figure 2 for $M1$ and $E2$ radiation were obtained. The fit is satisfactory and the results are consistent with other evidence (Boyle 1956) that mixed $M1$ and $E2$ transitions are involved. The value of the reduced width is considerably larger ($\theta^2 = 3.4$) than the Wigner single-particle limit ($3\hbar^2/2\mu R$) in agreement with results found in the ${}^{10}\text{B}(d,\alpha)$ reaction (Treacy 1953).

V. ACKNOWLEDGMENTS

The author wishes to thank Dr. P. B. Treacy for helpful discussions on these results and also Mr. N. F. Bowkett for his assistance in operating the High Tension Set.

VI. REFERENCES

- AJZENBERG, F., and LAURITSEN, T. (1955).—*Rev. Mod. Phys.* **27**: 77.
AJZENBERG, F., and LAURITSEN, T. (1959).—*Nuclear Phys.* **11**: 1.
BLOCH, I., HULL, M. M., BROYLES, A. A., BOURICUS, W. G., FREEMAN, B. E., and BREIT, G. (1951).—*Rev. Mod. Phys.* **23**: 147.
BOYLE, A. J. F. (1956).—*Nuclear Phys.* **1**: 581.
CHRISTY, R. F., and LATTER, R. (1948).—*Rev. Mod. Phys.* **20**: 185.
GARWIN, R. L. (1950).—*Rev. Sci. Instrum.* **21**: 569.
THOMAS, R. G. (1951).—*Phys. Rev.* **81**: 148.
TITTERTON, E. W. (1954).—*Phys. Rev.* **94**: 206.
TREACY, P. B. (1953).—*Phil. Mag.* **44**: 325.
WIGNER, E. P., and EISENBUD, L. (1947).—*Phys. Rev.* **72**: 29.

MEASUREMENTS OF CHANGES IN THE PHASE PATH OF RADIO WAVES REFLECTED FROM THE IONOSPHERE AT NORMAL INCIDENCE

By R. W. E. McNICOL* and J. A. THOMAS*

[*Manuscript received December 4, 1959*]

Summary

Fixed-frequency measurements were made at Brisbane, using pulse transmissions, of the changes in phase of radio waves received after reflection at normal incidence from the various ionospheric layers. Because of the homodyne detector used, such phase-path records have a very good signal-to-noise ratio. Also, due to the difference in behaviour of echoes of different polarization or from different ionospheric layers, the effective resolution is high. When the echoes had a well-defined phase, the rate of change of phase path with time was measured; the slowest rates were for smooth night-time E_s layers, when values as low as 1 m sec^{-1} were sometimes found, whereas for the night-time F_2 region the rates were usually in the range $10\text{--}40 \text{ m sec}^{-1}$. Records were also made of reflections from drifting E_s clouds, and of the effect of underlying E_s ionization on reflections from the F_2 region.

I. INTRODUCTION

Measurements of changes in the phase of a radio wave received after reflection from the ionosphere provide much information about the characteristics of the reflecting layer and the ionization along the path of the wave below the level of reflection. The changes are due to changes in the phase path P , where P is defined by the equation

$$P = 2 \int_0^h \mu dh,$$

μ being the refractive index corresponding to the element of height dh .

The present paper describes a simple experimental technique for recording such changes in phase path and gives a review of some of the results obtained at Brisbane (lat. $27\cdot5^\circ\text{S.}$, geomag. lat. $35\cdot7^\circ\text{S.}$). Some of the applications of the phase-path technique mentioned in this review have already been described incidentally in other papers, but it was considered desirable to bring them all together in one paper, and to discuss them explicitly, along with several additional features.

II. EXPERIMENTAL DETAILS

The Brisbane phase-path recording equipment employed a simplification of the techniques used by Findlay (1951) and Jones (1953). Pulse-modulated transmissions were used throughout, in order to resolve as well as possible the various echoes received.

* Physics Department, University of Queensland, Brisbane.

The complete phase-path recorder consisted of a normal fixed-frequency group-path recorder plus one extra unit, known as the "phase-path unit", a block diagram of which is given in Figure 1. This unit consisted essentially of a "phase-reference oscillator" (see below) and a mixer, in which beats were produced between the output of the phase-reference oscillator and the echo pulses coming from the receiver. These beats were then amplified and differentiated, and pips of one polarity were selected and fed to the output terminal of the unit. An isolating stage prevented the output of the phase-reference oscillator from leaking back into the receiver, which could thus be used simultaneously for making group-path records if desired.

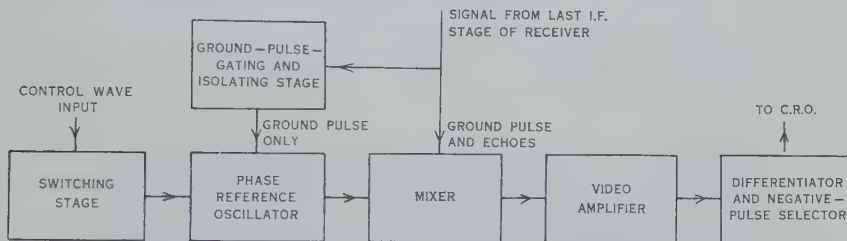


Fig. 1.—Block diagram of phase-path unit, used in conjunction with a fixed-frequency receiver, for making phase-path records.

To record changes in phase path, it is necessary to employ a suitable reference with which to compare the phase of the received signal. This reference was derived from an independent phase-reference oscillator (P.R.O.). Following Jones's technique, the P.R.O. was operated at a frequency near the intermediate frequency of the receiver, rather than near the actual signal frequency, since this allowed recording on any desired signal frequency merely by tuning the receiver to that frequency, no adjustments to the phase-path unit being necessary.

For convenience in recording, it was desirable that the P.R.O. should make several beats with the received signal within the duration of any given echo. As the duration of the transmitted pulse was about 70 μ sec, the P.R.O. was operated at a frequency about 30–40 kc/s above the intermediate frequency. The positive frequency difference caused downward-sloping fringes on the phase-path record to correspond to decreasing phase path and vice versa.

It was necessary for the phase of the oscillations generated in the P.R.O. to bear some fixed relation to the phase of the oscillations in the ground pulses. This was most conveniently done by causing the initial phase of the oscillations of the P.R.O. to be exactly locked to the phase of the intermediate frequency signal at the start of each ground pulse. The P.R.O. was switched on at the instant the transmitted pulse started and a phase-locking signal, derived from the ground pulse, was injected into the oscillator tuned circuit, the feedback in the oscillator circuit being adjusted so that, after each switch-on, oscillations started gradually. The P.R.O. was switched off after all wanted echoes had been received in each pulse-repetition cycle. It will be noted that, when synchronization of the P.R.O. is achieved in this way, it does not matter whether the trans-

mitter oscillator is itself pulse modulated or whether it runs continuously and only subsequent amplifier stages are pulsed.

A check on whether perfect synchronization has been achieved can be made by inspection of the fringes within the ground pulse. Whenever these fringes appear on the records, they should take the form of a series of straight lines parallel to the time axis of the record.

The output pips from the phase-path unit were fed to a cathode-ray display tube, where they produced brightness modulation. The pattern on the cathode-ray tube was photographed on continuously moving 35 mm film. A large enough rate of film advance was used to ensure that, even when the phase path of an echo was changing rapidly, the successive fringes on the record could be readily resolved when the film was examined in a viewer. A film speed of about 40 cm/hr was found satisfactory when the signal frequency was near 2 Mc/s, with proportionately higher speeds for higher frequencies.

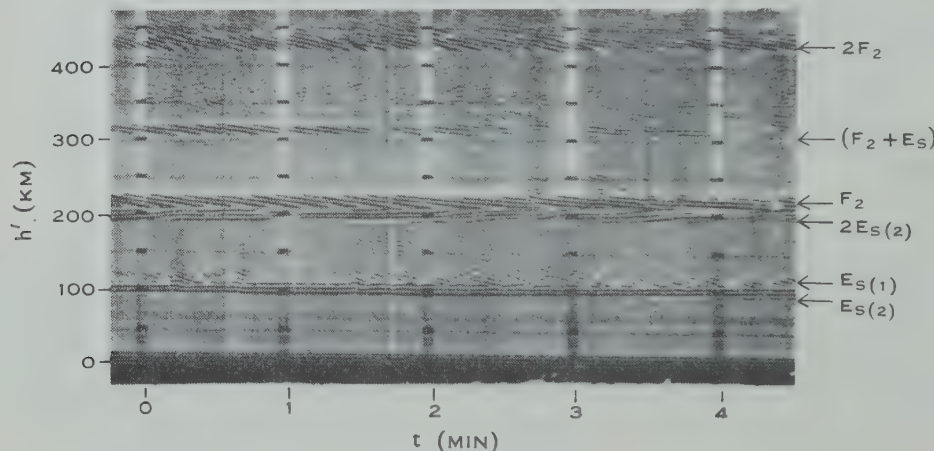


Fig. 2.—Phase-path record showing two E_s reflecting regions, at 95 and 110 km respectively, a double-hop E_s reflection at 190 km, an F_2 reflection at 210 km, an $(F_2 + E_s)$ reflection at 305 km, and a double-hop F_2 reflection at 420 km. Note the very slow rate of change of phase of the 95 km E_s reflection.

III. OUTLINE OF RESULTS AND DISCUSSION

(a) Phase Coherence and Phase Continuity

(i) *Description of These Phenomena.*—A phase-coherent echo is one in which the phase remains constant throughout the duration of the echo, i.e. the phase difference between the echo signal and a purely sinusoidal reference signal at the same frequency would be constant. In the case of a phase-incoherent echo, on the other hand, rapid, virtually discontinuous jumps in phase occur during the period of reception of the echo.

A good example of a phase-coherent echo is given in Figure 2, in the case of the echo from the E_s region at 95 km, whereas Figure 3 shows highly incoherent echoes in the case of the E_s and $2E_s$ echoes at 95 and 190 km respectively.

Another important property of echoes recorded with phase-path equipment is the phase continuity. This is determined by the faithfulness with which the phase at a given portion of any particular echo is repeated from one pulse-repetition cycle to the next (after an interval of 20 msec). The records show that all echoes, whether coherent or incoherent, show at least short-term phase continuity. Thus phase-coherent echo traces consist of well-defined fringes; and even phase-incoherent echo traces show short, slightly irregular, lines, approximately parallel to the time axis, the individual lines lasting for something between a few seconds and half a minute.

(ii) *Cause of Phase Incoherence.*—Phase incoherence occurs because the echo is the resultant of a number of randomly phased components, coming from scattering centres situated at varying ranges from the recording equipment and hence being received at varying time delays after the transmitted pulse. At the start of the received echo, only those components coming from the nearest

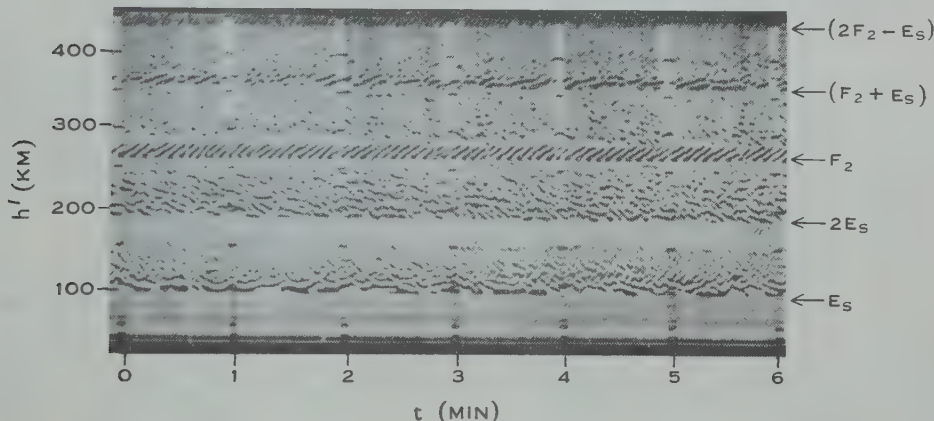


Fig. 3.—Phase-path record showing highly incoherent E_s reflections at 95 km (with a double hop at 190 km), with quite coherent F_2 -region reflections at 270 km and $(2F_2 - E_s)$ reflections at 455 km.

The incoherent trace at 365 km is an $(F_2 + E_s)$ reflection.

scatterers are received, but as time goes on during the period of reception of the echo, other components from the more remote scatterers begin to contribute to the resultant. The time required to change from the situation in which a given component is ineffective to the one in which it is effective is only the rise time of the received echo pulse from this particular scatterer, a time of only about 10 μ sec. If the amplitude of any particular new component is comparable with the amplitude of the resultant immediately prior to its arrival and if the two signals are in substantially different phase, there will be a significant and rapid jump in phase as the amplitude of the new component rises from zero to near its full value. Thus the phase of the resultant of all the components, i.e. the phase of the total received echo signal, can change substantially in only a few microseconds; this explains the rapid, virtually discontinuous jumps in phase mentioned above as characteristic of phase-incoherent echoes.

(iii) *Discussion of Short-term Phase Continuity.*—It is interesting to consider the probable reason why we find traces showing short-term phase continuity, even in the case of phase-incoherent echoes. In the case of such echoes, the total signal received at any instant is the vector sum of a large number of randomly phased components, coming from discrete, irregularly situated, scattering centres. The speed with which these centres are moving along the line of sight is believed to be only of the order of a few metres per second (McNicol 1949). The phase of the individual components of the total signal cannot change substantially in a time less than it takes the centres to move distances of the order of a tenth of a wavelength of the exploring wave, and this time is at least a few seconds. The resultant signal consequently cannot change phase substantially in less than several seconds, i.e. whatever the phase of an echo is at a given instant, that phase will in general persist for at least a few seconds, except on the special occasions when the amplitude is passing through zero, at which times the phase can reverse almost discontinuously.

(b) Time-rate-of-change of Phase Path

In the case of phase-coherent echoes, and only in this case, it is possible to make statements about the rate of change of phase path with time, e.g. the E_s -region echo at 95 km in Figure 2 above shows a change of only one fringe in several minutes, the F_2 -region echo (at 210 km) a change of about 4 fringes per minute, the (F_2+E_s) echo (at 305 km) a change of about 4 fringes per minute, and the $2F_2$ echo (at 420 km) a change of about 8 fringes per minute.*

Very slow rates of change—say less than one wavelength per minute—occur only for night-time E_s -region echoes, and then only rarely. More commonly the rates of change are of the order of several wavelengths per minute, occasionally increasing to values well in excess of this, e.g. at times of F_2 -region sudden height rises (see Section III (h) (ii) below).

(c) Correlation between Phase-path and "Swept-gain" Records

The degree of coherence or incoherence of phase-path records depends on the degree of regularity or irregularity of the reflecting region. We would, therefore, expect a close correlation between phase-path records and swept-gain records, i.e. records made by reducing the receiver gain periodically at a logarithmic rate from a very high value to a very low one (McNicol, Webster, and Bowman 1956). This correlation is in fact found to occur. An example is given, in Figure 4, of swept-gain records taken simultaneously with the phase-path records of Figure 3. As mentioned above, Figure 3 shows at 95 km an echo from the E_s region with highly incoherent phase-path fringes. On the corresponding swept-gain record the E_s echo takes the form of "triangular" patches which show a considerable spread in virtual height at the start of each period, where the receiver gain is high. Both these records indicate a high degree of

* It was usually observed that multiple-hop echoes, such as the $2F_2$ mentioned above, showed phase changing at approximately twice the rate of the corresponding single-hop case, and combination echoes, such as the (F_2+E_s) , showed changes corresponding to the sum of those present on the component echoes.

irregularity of the reflecting layer. On the other hand, the echo from the F_2 region, at 270 km in Figure 3, shows highly coherent phase-path fringes, and these correspond with the almost "rectangular" swept-gain patches at 270 km on Figure 4, which show almost no spread in virtual height, even at high gain. In this case the indications from both records are of reflections from a very smooth layer.

(d) Simultaneous Phase-path and Group-path Recording

It will be noted that the bottom edge of the recorded phase-path trace gives the value of the group path for the working frequency, albeit with slightly less precision than a normal group-path record would. Phase-path records thus offer the possibility of conveniently comparing changes in group path with

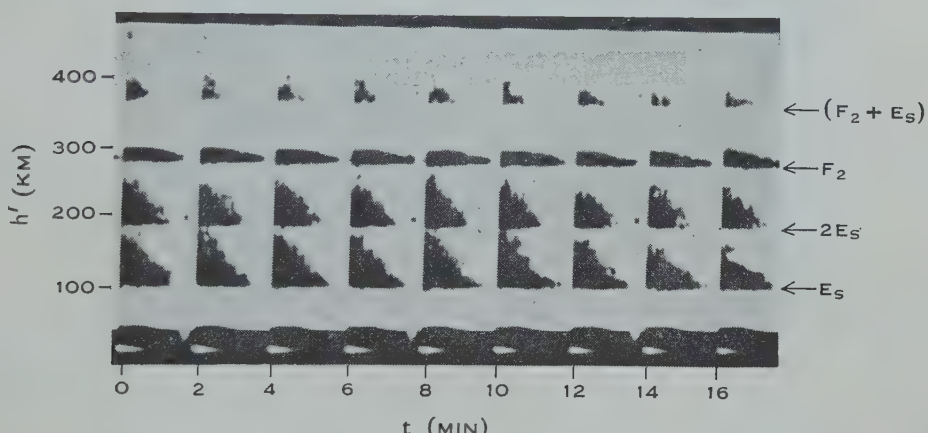


Fig. 4.—Swept-gain record corresponding to the phase-path record of Figure 3 showing reflections from irregular E_s region at 95 km (with a double hop at 190 km), reflections from a smooth F_2 region at 270 km, and weak irregular ($F_2 + E_s$) reflections at 365 km.

changes in phase path for any particular echo. Such comparisons are particularly valuable in determining, for example, whether observed changes in group path or phase path are due to real changes in range of the reflecting region, or to changes in the ionization density along the path, below the point of reflection.

(e) Improvement of Signal-to-noise Ratio

It was often observed that the phase-path records were more successful in recording very weak echoes than were group-path records made simultaneously, even when both recorders used the same transmitting and receiving systems. This was due to the fact that, for the phase-path records, the mixer stage in the phase-path unit was supplied with a relatively large signal from the phase-reference oscillator as well as with the output from the final intermediate frequency amplifier in the receiver. The output from a phase-reference oscillator is phase coherent with all of the components in the frequency spectrum of the wanted echo, but not with the noise pulses, which are in random phase. We thus have virtually a homodyne detector. Goldman (1948) points out that an

improvement in signal-to-noise ratio is characteristic of systems in which the coherence standard of the detector is maintained beyond its normal operating range. For the group-path records a linear amplitude-modulation detector is used and there is no corresponding improvement.

(f) Improvement in Resolution of Overlapping Traces

It frequently happens that traces which would be unresolved when using normal group-path techniques with a given pulse width may be effectively resolved on phase-path records, as, for example, the cases shown in Figures 2 and 9, because of the recognizable differences in the behaviour of the phase path of the various components of the composite echo.

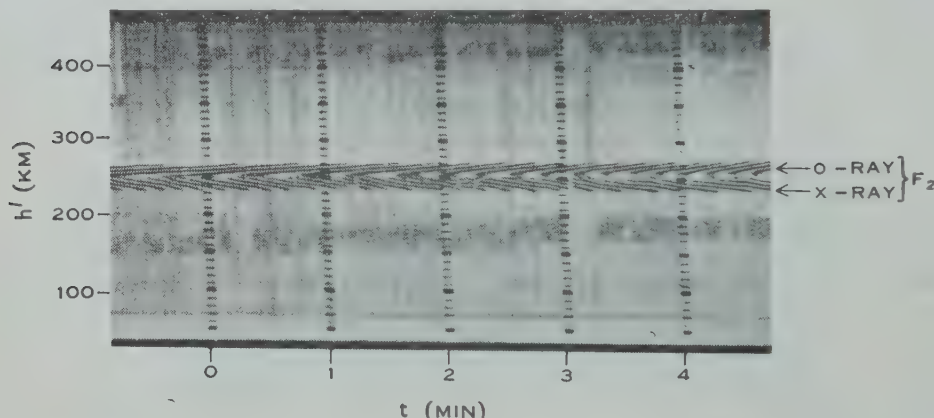


Fig. 5.—Phase-path record showing different behaviour of *o*- and *x*-reflections from F_2 region.

*(g) Independence of Phase Path of *o*- and *x*-Rays*

We may utilize the fact that the rate of change of phase path is often markedly different for the two magneto-ionic components, to give increased resolution above the normal $h't$ records. In Figure 5 for example the *o*-ray shows a phase-path increase whilst the *x*-ray simultaneously shows a decrease in phase path. Such "herring-bone" patterns are not at all uncommon.

(h) F-Region Phenomena

(i) *Extra Traces*.—Group-path records of F_2 -region night-time reflections often show spreading in range, and at times show a main trace and a number of discrete extra traces. Phase-path records have been made to find the rate of change of phase path of these traces (McNicol, Webster, and Bowman 1956).

(ii) *Sudden Height Rises*.—From time to time at night, travelling disturbances in the ionosphere cause distortion of the F_2 -region ionization contours. If a large disturbance occurs, it shows itself on group- or phase-path records as a fairly abrupt rise in the virtual height of the reflection level at any given frequency. The *o*-ray is affected first, followed after a short interval (of a few minutes) by the *x*-ray. If the working frequency is well below the critical frequency of the region, the *o*- and *x*-rays at quiet times are normally not

resolved at night on $h't$ records, so the effect of the disturbance is to produce a temporary separation of the o - and x -ray traces. A typical example of the phase-path behaviour during such an occurrence is shown in Figure 6. McNicol, Webster, and Bowman (1956) have made measurements on a number of such records and point out that the change in group path is always much more marked than the change in phase path of either the o - or x -rays.

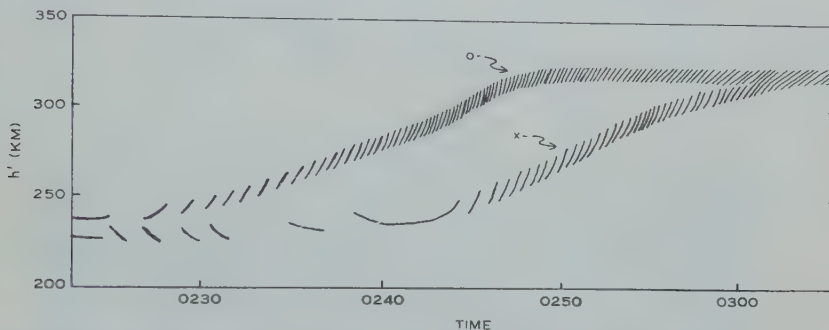


Fig. 6.—Phase-path record showing different behaviour of o - and x -reflections from F_2 region during an F_2 -region sudden height rise. (Only every fifth fringe is shown.)

(i) E_s -Region Phenomena

(i) *Isolated Clouds of Ionization.*—One of the most striking types of phase-path record is obtained when we have reflections from isolated patches (clouds) of E_s ionization drifting horizontally at a fixed height of about 100 km. Findlay (1951) has discussed such records, an example of which is given in Figure 7.

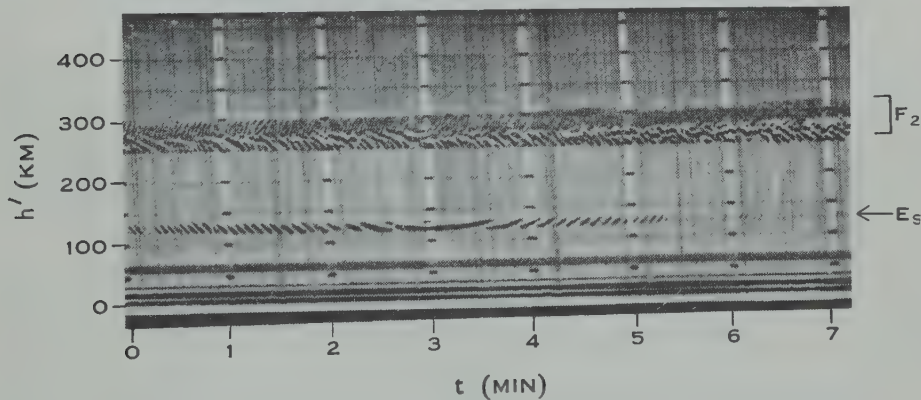


Fig. 7.—Phase-path record showing drifting E_s cloud at 120 km.

Measurements of the rate of change of phase path agree with the measured rates of decrease and increase of slant group path within the limits of error, and good estimates can thus be made of the speed of movement of such patches.

We might hope to find out something about the ionization density in E_s clouds by observing the effect the passage overhead of such clouds has on the

phase-path records of reflections from the F_2 region. In particular, if the ionization density in the cloud were greater than that of its surroundings, we would expect the phase path from a stationary F_2 region to show a temporary decrease as the E_s cloud passes overhead. In practice, however, the picture is considerably complicated by the fact that the F_2 -region echo is usually changing in phase path quite independently of the presence of any observable E_s region. Also, on many of the occasions on which we can be sure that an observed E_s cloud has passed exactly overhead (say, by direction of arrival measurements or by noting the behaviour of multiple E_s reflections), the F_2 region is blanketed, and on such occasions we lose the F_2 -region echo and so cannot observe its changes of phase path. Accordingly, no definite conclusion could be drawn from the records as to whether E_s echoes are associated with any increase in total electron content in the E region or not.

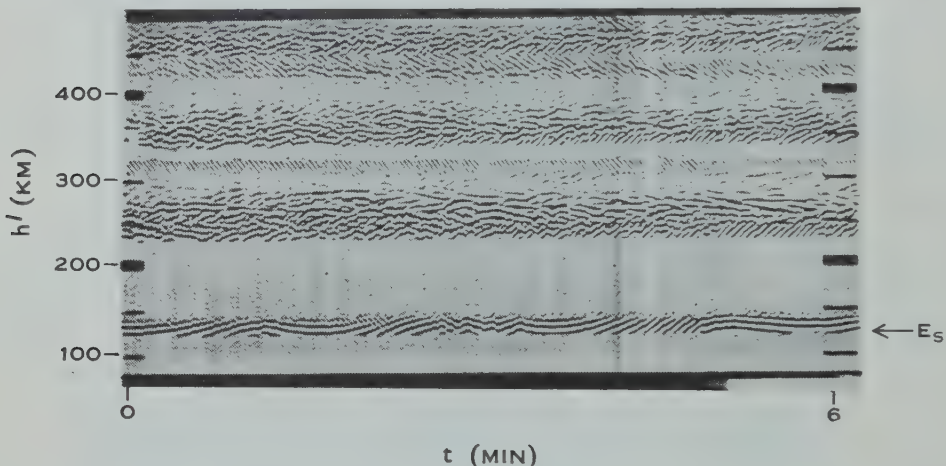


Fig. 8.—Phase-path record showing overlapping E_s clouds at 125 km.

Figure 8 illustrates a rather more common event—at 125 km we have the obvious overlapping of echoes from a series of E_s clouds to form a trace which on group-path records would give no such definite indication of structure.

Occasionally the leading and trailing edges of such cloud echoes extend to ranges beyond that of the main echo, giving rise to converging and diverging traces on group-path records and decreasing and increasing phase paths on P, t records as discussed by Thomas and Burke (1956).

Sometimes the recorded trace presents a completely jumbled appearance, as shown in Figure 3 above, i.e. we have phase incoherence, as discussed in (a) above. This jumbled appearance is probably due to the fact that a large number of clouds are present simultaneously and the traces due to echoes from individual clouds are no longer separately discernible.

(ii) *Simultaneous Occurrence of Several Different Types of E_s Region.*—Quite frequently phase-path records were obtained which show smooth and irregular E_s regions to be present simultaneously. Figure 2 shows a very smooth

E_s region at 95 km, together with a more irregular E_s region at 110 km. A more complex example is shown in Figure 9, where the E_s echo is clearly divisible into three parts, at 95, 110, and 130 km respectively. The phase-coherent central portion shows up again at 220 km on the double-hop path with twice the rate of change of phase path of the single-hop echo. These latter facts make it probable that the E_s region responsible for the echo at 110 km is overhead, at a height close to 110 km, rather than being displaced to one side and being at a slant range of 110 km but at a smaller actual height. If this is true, the smooth E_s region at 110 km must be completely embedded in some quite separate, irregularly distributed, E_s ionization.

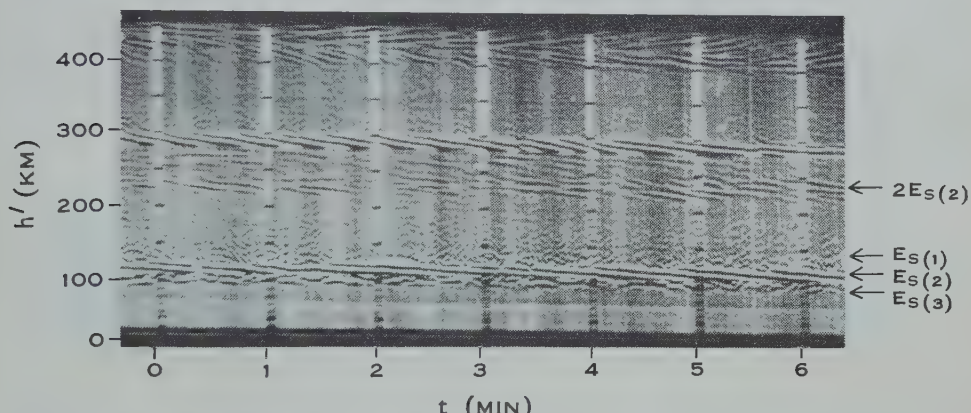


Fig. 9.—Phase-path record showing three different E_s reflecting regions, at 95, 110, and 130 km respectively, and an F_2 region at 280 km.

(iii) *Distinction between Sequential and Constant-height E_s Regions.*—It can be stated generally that the type of sporadic- E echo classified as "sequential E_s " is consistently more phase coherent and stable than the type designated as "constant-height E_s " (McNicol and Gipps 1951). This feature has been used as an aid in distinguishing between these two types of E_s (Thomas 1956).

(j) Effect on F_2 -region Phase-path Records of Underlying Irregular E_s Ionization

One interesting effect is sometimes noticed when echoes from a partially reflecting E_s layer are observed simultaneously with F -region echoes. Normally one would expect incoherent E_s echoes to be accompanied by incoherent F echoes and this is often so. However, in certain cases, such as the one illustrated in Figure 3 above, the E_s echoes are mainly incoherent, while the F_2 echoes (which involve waves passing twice through the E region) are phase coherent. In addition it will be noted that, in this case, the M echo, i.e. the $2F_2-E_s$ echo, is also phase coherent. These observations suggest that, whatever the mechanism by which the E_s region produces reflection of radio waves at normal incidence may be, the region on such occasions has the peculiar property of looking rough

and irregular when viewed from beneath, of looking relatively smooth when viewed from above (as in M reflections), and of being virtually invisible, in so far as variations of phase are concerned, to radio waves passing right through it.

(k) Phase-path Changes during Penetration of a Layer

Although in this paper no direct experimental method of recording phase path as a function of radiated frequency is described, nevertheless some penetration information has been gained by operating on a fixed frequency and by taking advantage of the fact that on certain occasions the ionospheric changes are such as to cause the penetration frequency of one or other of the reflecting layers to pass through the operating frequency of the phase-path equipment. The value of this procedure is somewhat reduced by the fact that it may take quite a few minutes for the complete record to be made and changes in the height of the reflecting layer as a whole may occur during this time, as also may changes in the distribution of ionization at levels well below the reflecting layer, and either of these changes will give rise to changes in the phase path other than those specifically due to the penetration of the layer.

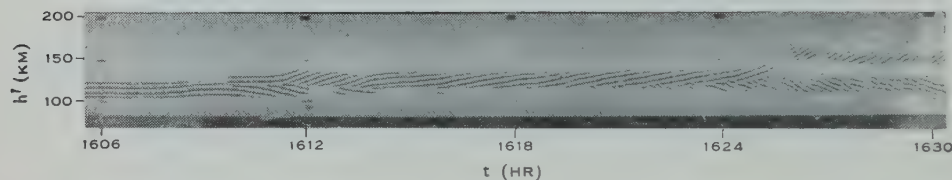


Fig. 10.—Phase-path record showing penetration of E_s region at 1610 hr and penetration of normal E region at 1626 hr.

Figure 10 illustrates two aspects of such penetrations. Near the start of the record, at 1610 hr, there is a sudden reflection "jump" from E_s to normal E , and the phase-path fringes show no consistency from the one region to the other. At 1626 hr, we have, on the other hand, a penetration of the normal E region, and here the phase-path fringes tend to carry over across the penetration to the F region.

Computations of phase path as a function of frequency carried out by Lander (personal communication) for E -region penetrations show a smooth increase of phase path with frequency. Correspondingly it has been noted that the fixed-frequency phase-path record always shows a continuing increase whenever the wave penetrates a region.

IV. CONCLUSION

Phase-path records are easy to make and provide a very useful supplement to the information obtained about the ionosphere in other ways. Their good signal-to-noise properties and their potentialities for the resolution of overlapping echoes are especially valuable.

V. ACKNOWLEDGMENTS

The authors wish to acknowledge financial grants from the Radio Research Board of C.S.I.R.O. and the Research Committee of the University of Queensland.

VI. REFERENCES

- FINDLAY, J. W. (1951).—*J. Atmos. Terr. Phys.* **1** : 353.
GOLDMAN, S. (1948).—“Frequency Analysis, Modulation and Noise.” (McGraw-Hill : New York.)
JONES, R. E. (1953).—*Rev. Sci. Instrum.* **24** : 433.
McNICOL, R. W. E. (1949).—*Proc. Instn. Elect. Engrs.* III **96** : 517.
McNICOL, R. W. E., and GIPPS, G. DE V. (1951).—*J. Geophys. Res.* **50** : 17.
McNICOL, R. W. E., WEBSTER, H. C., and BOWMAN, G. G. (1956).—*Aust. J. Phys.* **9** : 247.
THOMAS, J. A. (1956).—*Aust. J. Phys.* **9** : 228.
THOMAS, J. A., and BURKE, M. J. (1956).—*Aust. J. Phys.* **9** : 440.

EXPERIMENTAL RELATIONS BETWEEN IONOSPHERIC TRUE HEIGHT, GROUP HEIGHT, AND PHASE HEIGHT

By J. A. THOMAS* and R. W. E. McNICOL*

[Manuscript received December 4, 1959]

Summary

Computations of ionospheric phase height at a particular frequency have been made using true height analyses of $h'f$ curves. Temporal changes in these computed values agree well with experimentally measured changes of phase path both in the case of regular diurnal variations and during an eclipse. The true height analyses are thus shown to be experimentally reliable, and at the same time we can allot an "absolute" value to the normal phase-path records.

I. INTRODUCTION

On the basis of ray optics the phase path of a radio wave vertically reflected from the ionosphere at a true height "h" is given by

$$P = 2 \int_0^h \mu dh,$$

where μ is the refractive index (at the frequency concerned) corresponding to the element of height dh . The group path is given by the companion expression

$$P' = 2h' = 2 \int_0^h \mu' dh,$$

where μ' is the group refractive index defined by $\mu' = \mu + f\partial\mu/\partial f$.

Both the group path and the changes in phase path at a fixed frequency may be experimentally determined. Estimates of true height of reflection may be made by various means based on measured (P', f) curves, and we are therefore in a position to compare the measured values of P' and ΔP with those derived from estimates of true height.

II. EXPERIMENTAL MEASUREMENTS

Phase-path measurements have been made at Brisbane at a frequency of 5.8 Mc/s by the method described by McNicol and Thomas (1960). Enlargement of the resulting films enables the phase fringes to be counted starting from some arbitrary origin of time, a decrease of phase path of one wavelength being registered as -1, and an increase as +1. By this means we obtain plots of ΔP values throughout the daylight hours as indicated in Figure 1. Because of interference and the necessity for changing film it is not possible to follow the phase throughout a complete day.

* Physics Department, University of Queensland, Brisbane.

Care is taken to count fringes corresponding to σ -ray reflections only. The estimated accuracy of such a count at the end of a day is ± 10 fringes; this is much greater than any shift due to oscillator instabilities, but still represents a negligible error in a count of some 6000 fringes. There is considerable variation from day to day in such curves; these day-to-day variations are usually associated with similar day-to-day variations in group path.

Simultaneous h' , f records have been taken throughout the day as part of the routine Ionospheric Prediction Service recording and these are available for reduction to (N, h) profiles. Values of h' at 5.8 Mc/s may be taken from either the phase-path films or the $h'f$ curves. Piggott (1959) has recently demonstrated

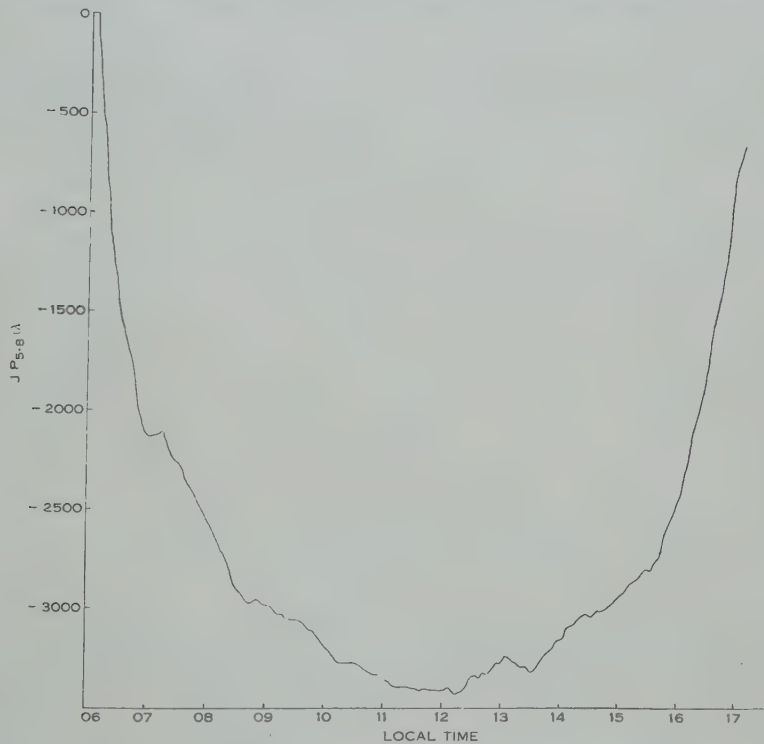


Fig. 1.—Plot of phase-path changes throughout the day (Brisbane, April 9, 1959).
The small irregularities shown here are typical.

the necessity for correcting the values of h' for the large receiver delays commonly found in $h'f$ recorders. For the equipment used the delay is substantially independent of frequency and is given by $D = 9 - 0.4W$ where W is the width (in kilometres) of the recorded trace and D is the correction in kilometres. These corrections have been applied to the data analysed here.

III. TRUE HEIGHT ANALYSIS

Using the method developed by Schmerling (1958) and the tabulated values of sampling frequencies given by either Ventrice and Schmerling (1958) or Wright and Norton (1959), a manual reduction of a number of $h'f$ curves has

been carried out to derive the corresponding (h,f) curves. A typical example of the results of such a reduction is shown in Figure 2. The oscillation of the height values about the general trend is due to the limited sampling method employed, and has been discussed earlier by Piggott (1954). The best one can do in such circumstances is to fit a "mean" curve such that the sum of the areas between the mean curve and the oscillatory curve is balanced. It is obvious that great care must be exercised in using the Schmerling analysis for day-time

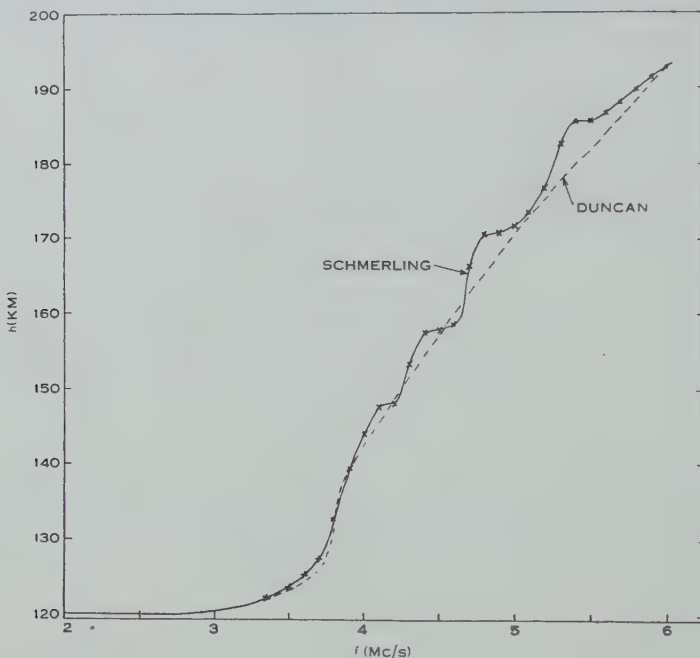


Fig. 2.—A comparison of (h,f) data derived from machine analysis (Duncan), and sampling analysis (Schmerling) of (h/f) data for 1440 hr on April 10, 1959.

records. The height calculations must be carried out at very close frequency intervals if false data are not to be obtained. This difficulty does not exist at night except in the neighbourhood of the F_2 penetration frequency.

For 15 cases the corresponding (h,f) data derived using the machine analysis of Duncan (1958) have also been plotted in Figure 2. It will be noticed that the two sets of data are in substantial agreement up to about 4 Mc/s, but beyond this frequency the Schmerling values of true height are consistently higher than the Duncan values. This is so for all 15 cases, the difference at 6 Mc/s being usually about 3 km.* Such differences may often be neglected, but become important when one computes the phase and group refractive indices as functions of height.

* Since this work was carried out Duncan (personal communication) has inserted a slight correction into his programme; this correction brings the two methods into very close agreement.

IV. CALCULATION OF REFRACTIVE INDICES

Using the methods of Whale and Stanley (1950) and Shinn and Whale (1952), we may compute the values of μ and μ' for a frequency of 5.8 Mc/s for vertical *o*-ray propagation at Brisbane, neglecting collisions. Using the previously calculated (h, f) profiles we obtain μ and μ' as a function of true height at a number of times throughout the day.

V. COMPUTED GROUP PATH

By plotting $\mu'_{5.8}$ as a function of height we obtain curves such as Figure 3. The area beneath this curve is $\int_0^h \mu' dh$ and should thus agree with $h' = \frac{1}{2}P'$ if the previous calculations have been correctly carried out. In practice the area is computed up to the height at which the plasma frequency (f_p) is 5.6 Mc/s ($\mu' = 3.98$). Between this height and the reflection height the electron density

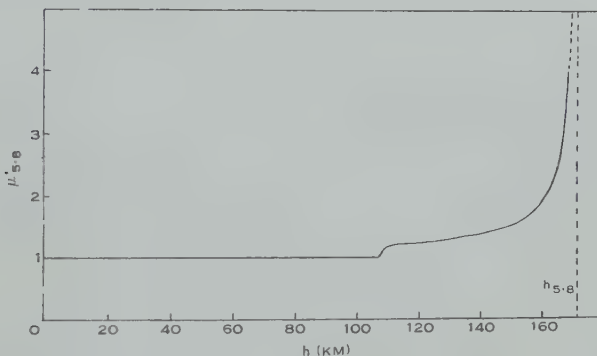


Fig. 3.—Plot of $\mu'_{5.8}$ versus true height for Brisbane at 1024 hr on April 8, 1959.

is assumed to increase linearly, and the transformation is made to the variable $t = \sqrt{(1 - f_p^2)/5.8^2}$. As Shinn and Whale have indicated, we can now obtain a finite answer to the value of

$$\int_{h_{5.6}}^{h_{5.8}} \mu' dh = C(h_{5.8} - h_{5.6}) \int_{t_{5.6}}^{t_{5.8} (=0)} \mu' t dt,$$

since $\mu' t$ tends to a limiting value as $t \rightarrow 0$. For Brisbane conditions this reduces to 12.1 ($h_{5.8} - h_{5.6}$) km, and this value must be added to the previously calculated value of the area up to $h_{5.6}$.

Comparisons between the computed group-path values and those actually observed can now be made. In all cases the two agree within a few kilometres. For those curves analysed using the Duncan method the computed values tend to be systematically low (3.5 km on the average). For those analysed using the Schmerling method, however, the computed values show rather more scatter but on the average agree with the observed values.

VI. COMPUTED PHASE PATH

By plotting $\mu_{5.8}$ as a function of height we obtain curves such as Figure 4. The area beneath this curve is $\int_0^h \mu dh$ and should thus agree with $\frac{1}{2}P$. We have no records of P as such, but only changes in P over a period of time. The computed values of P should vary throughout the day in the same way as does the change in P derived from the fringe count. A comparison of the two sets of data for the eclipse day of April 8, 1959, is given in Figure 5.

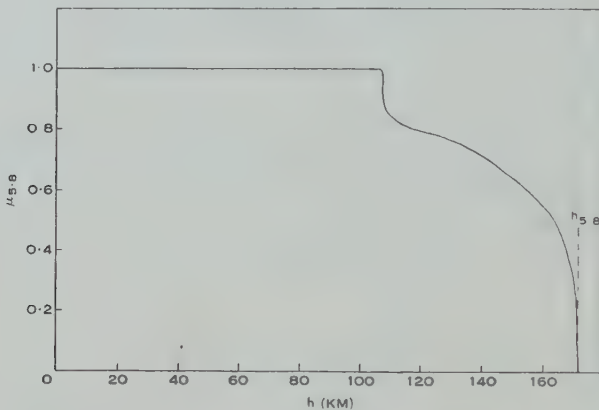


Fig. 4.—Plot of $\mu_{5.8}$ versus true height for Brisbane at 1024 hr on April 8, 1959.

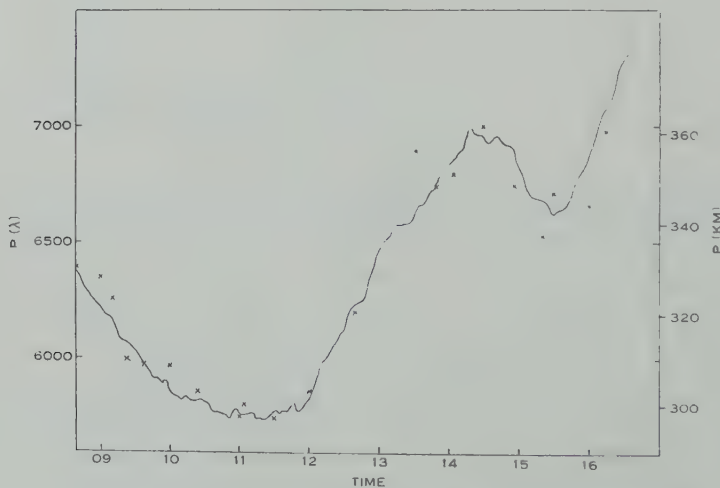


Fig. 5.—Comparison of measured phase-path variations with computed values (\times) of phase path for April 8, 1959.

We thus have, from the good agreement shown here and throughout other days, a direct independent experimental check on the validity of the true height estimations using the Schmerling and Duncan methods. It should be noted that, whereas in the computation of $\int \mu' dh$ the (h, f) curve near the reflection

point (where μ' is high) must be very accurately known, for the computation of $\int \mu dh$ the base height of the E region (where μ is high) is rather more important. It is just this region which is sometimes in doubt because of strong day-time absorption, and recourse has to be made to extrapolation of the $h'f$ curve. This undoubtedly explains some of the larger deviations shown in Figure 5.

By adjusting the vertical position of the ΔP curve to get the best least squares fit to the $\int \mu dh$ points, we can allot an "absolute" value to the phase-path results, i.e. we have a measure of the *total* phase path. The curve of Figure 5

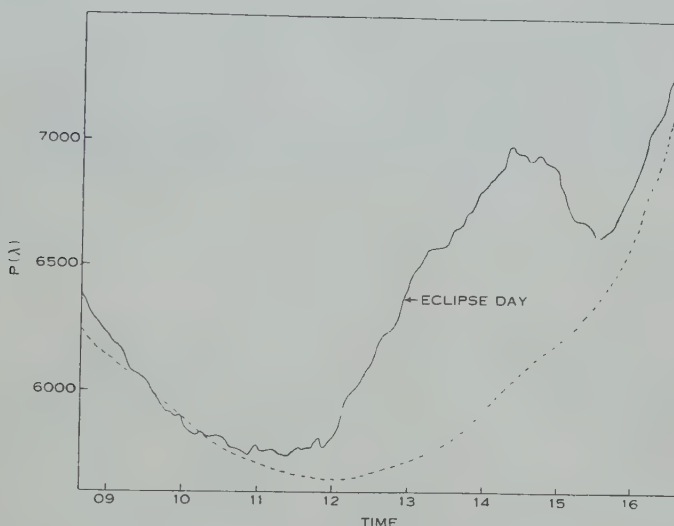


Fig. 6.—Comparison of "absolute" phase path for eclipse and control days.

has been so fitted and we can thus allot an absolute phase of 5810 wavelengths at 1200 hr. The same can, of course, be done for other days with an error of less than 20 wavelengths (~ 1 km)—we have thus regained some of the information lost through inability to record right through the night.

We can now compute, using "absolute" phases, the average absolute phase path throughout a series of days and use this for comparison with unusual effects produced on certain days, e.g. by an eclipse. Such a comparison is shown in Figure 6.

Such comparisons are useful mainly in giving an idea of the integrated effect of any ionization changes taking place. The eclipse day effect will be further discussed elsewhere.

VII. CONCLUSION

We have shown that computed values of ionospheric electron density as a function of height are experimentally reliable, and that they enable us to allot an absolute value to the normal phase path records. True height computations appear to be valid during an eclipse period.

VIII. ACKNOWLEDGMENTS

The authors wish to acknowledge financial grants from the Radio Research Board of C.S.I.R.O. and the University Research Committee, and to express appreciation of the assistance rendered by Mr. P. Monro. The Ionospheric Prediction Service cooperated in the loan of ionosonde records.

IX. REFERENCES

- DUNCAN, R. A. (1958).—*J. Geophys. Res.* **63**: 491.
McNICOL, R. W. E., and THOMAS, J. A. (1960).—*Aust. J. Phys.* **13**: 120.
PIGGOTT, W. R. (1954).—*J. Atmos. Terr. Phys.* **5**: 201.
PIGGOTT, W. R. (1959).—*J. Atmos. Terr. Phys.* **14**: 175.
SCHMERLING, E. R. (1958).—*J. Atmos. Terr. Phys.* **12**: 8.
SHINN, D. H., and WHALE, H. A. (1952).—*J. Atmos. Terr. Phys.* **2**: 85.
VENTRICE, C. A., and SCHMERLING, E. R. (1958).—Sci. Rep. No. 106. Ionospheric Research Laboratory, Pennsylvania State University.
WHALE, H. A., and STANLEY, J. P. (1950).—*J. Atmos. Terr. Phys.* **1**: 82.
WRIGHT, J. W., and NORTON, R. B. (1959).—Nat. Bur. Standards Rep. No. 6031.

THE LIFETIME AND CELL SIZE OF THE GRANULATION IN SUNSPOT UMBRAE

By R. E. LOUGHHEAD* and R. J. BRAY*

[*Manuscript received December 14, 1959*]

Summary

High quality photographs extending over a period of 2 hr 11 min have been obtained of the granulation in the umbra of a large sunspot. In agreement with earlier work, the mean cell size of the umbral granulation is found to be significantly less, and the lifetime considerably greater, than that of the photospheric granulation. Ten per cent. of the umbral granules last for over 2 hr.

The majority of the umbral granules, like the photospheric granules, show no detectable change in brightness, size, or shape during the periods over which they are observed to persist as identifiable structures. Some information is obtained about the modes of formation and dissolution of individual granules.

The similarity between the photospheric and umbral granulation is pointed out, and the possible role played by convective processes in sunspots is briefly discussed.

I. INTRODUCTION

Recent observations of the detail in sunspot umbrae (Bray and Loughhead 1959) have shown that the umbral granulation, while resembling the photospheric granulation in appearance, differs in lifetime and cell size. Measurement of a 32 min 42 sec sequence of photographs showed that some umbral granules last for at least this period; the cell size, although derived from limited data, was found to be significantly less than that of the photospheric granulation. The present paper gives the results of the measurement of the lifetime and cell size of the granulation in the umbra of a large spot showing clear granular structure, based on a longer sequence showing a greater number of granules.

The mean cell size is found to be 2.3 sec of arc as compared with 2.9 sec for the photospheric granulation. Sixty-seven per cent. of the umbral granules last for more than 15 min, 27 per cent. for more than 45 min, and 10 per cent. for over 2 hr. Like the photospheric granules (Bray and Loughhead 1958b), most umbral granules showed no detectable change of brightness, size, or shape during the periods over which they were observed to persist as identifiable structures.

II. OBSERVATIONS

The observations of the granulation in the umbra of the spot were made with a 5-in. photoheliograph using techniques similar to those described previously (Bray and Loughhead 1959). Two consecutive sequences of photographs were obtained, each covering a period of nearly an hour. The umbral granules appear quite clearly on both sequences, taken with exposures three and five times greater than those required for the photosphere (cf. Plate 1). Together, the two sequences allowed the granules to be studied over a total period of 2 hr

* Division of Physics, C.S.I.R.O., University Grounds, Chippendale, N.S.W.

11 min. Some of the brighter granules are also visible on a 10 min sequence of twofold exposures taken shortly before.

The film, which was taken under good seeing conditions, contains nearly 40 umbral photographs whose quality approaches the theoretical performance of the telescope. Plate 1 shows the detail present in the umbra of the spot. Plate 1 (*a*) is a normal photograph of the spot and the surrounding photospheric granulation. Plate 1 (*b*) shows, on twice the scale, a photograph taken through a 0.22 mm diaphragm at the prime focus with three times the exposure of Plate 1 (*a*). Granulation appears over a large part of the umbra though none is visible in the left-hand portion, which is considerably darker than the rest.

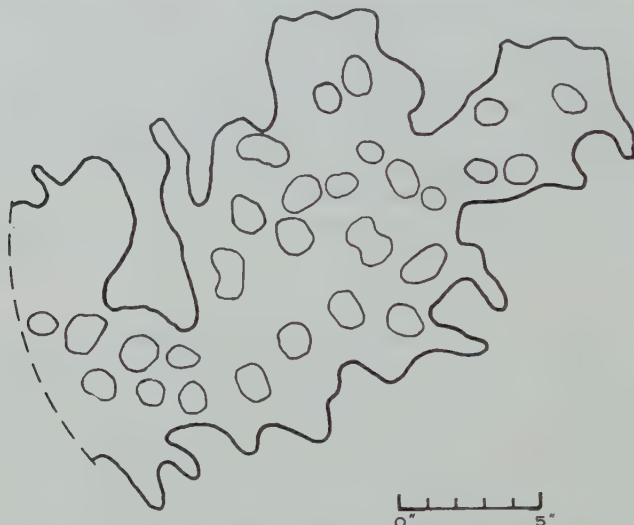


Fig. 1.—Umbral granulation pattern at 1^h 2^m 36^s. The heavy line represents the apparent outline of the umbra. The lower histogram in Figure 2 was derived with the aid of this map.

Some of the granules are so close together that they can barely be distinguished. Note the bright forked structure in the left-hand portion of the umbra.* Plate 1 (*c*) shows a photograph with five times the exposure of Plate 1 (*a*), also taken through the diaphragm. The umbral granules now appear brighter, but the exposure is still insufficient to reveal any detail in the left-hand portion. (There are often large differences in intensity between different regions of an umbra, several intensity minima usually being present (Bray and Loughhead 1959)). Note the detachment of the left-hand tip of the fork to form a granule during the interval between Plates 1 (*b*) and 1 (*c*) (80 min).

III. CELL SIZE

Direct measurements of the diameters of individual umbral granules provide at best only a rough guide to the true dimensions owing to their dependence on photographic contrast and on the combined instrumental profile of telescope and

* Such forks or loops are characteristic features of sunspot umbrae : with the correct exposure they, too, often show a granular appearance.

atmosphere. However, measurements of the mean cell size of the pattern, defined as the average distance between the centres of adjacent granules, are independent of these effects, provided individual granules are actually resolved. This quantity therefore provides a reliable and convenient parameter for characterizing the scale of the pattern. A similar parameter is often used in the theory of convective motion.

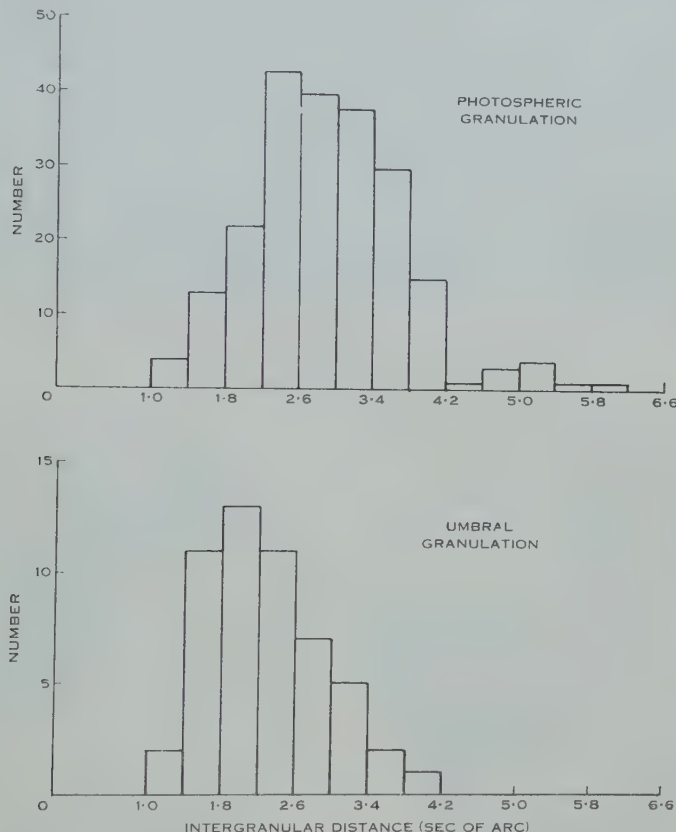


Fig. 2.—Cell size of the umbral and photospheric granulation patterns: the histograms give the distributions of the distances between the centres of adjacent granules (corrected for foreshortening), measured for groups of 28 umbral and 92 photospheric granules. The mean cell sizes are 2.3 and 2.9 sec of arc respectively.

The cell size measurements were derived from a very good photograph taken with an exposure factor of five. A map of the 28 umbral granules visible on this photograph is shown in Figure 1. Some of the granules near the edge of the umbra cannot be distinguished on Plate 1 owing to the difficulty of recording objects of different brightness with high contrast on a single reproduction.

The distribution of the 52 intergranular distances measured is given in Figure 2, which also shows the cell size distribution of the photospheric granulation, derived from a good-quality photograph (Bray and Loughhead 1958b: cf. Plate 1) taken with the same instrument. It is evident that the cell size

of the umbral granulation is significantly less than that of the photospheric granulation, the *mean* cell sizes being 2.3 and 2.9 sec of arc respectively.* Observations of higher resolving power might be expected to yield somewhat more symmetrical distributions, with some separations of less than 1 sec of arc.

IV. LIFETIMES

The lifetimes of the umbral granules were determined by a method similar to that used in determining the lifetimes of the photospheric granules (Bray and Loughhead 1958b). The results of the measurements, which refer to 48 granules in all, are as follows: 67 per cent. of the granules had lifetimes exceeding 15 min, 38 per cent. exceeded 30 min, 27 per cent. exceeded 45 min, and 10 per cent. exceeded 2 hr. Three particularly bright granules are visible on the short sequence of twofold overexposures as well as on the two long sequences; these granules lasted for at least $2\frac{1}{2}$ hr.† Umbral granules are therefore considerably longer-lived than photospheric granules, whose lifetimes, according to the best available estimates, are of the order of 10 min (Macris 1953; Bray and Loughhead 1958b).

V. CHANGES IN UMBRAL GRANULES

The umbral granules exhibit a diversity in brightness, size, and shape similar to that shown by the photospheric granules. By examining their appearances on each photograph in the sequences, an attempt was made to detect changes in the individual granules during the periods over which they were observed to persist as identifiable objects. The results are given in Table 1.

TABLE 1
CHANGES IN UMBRAL GRANULES

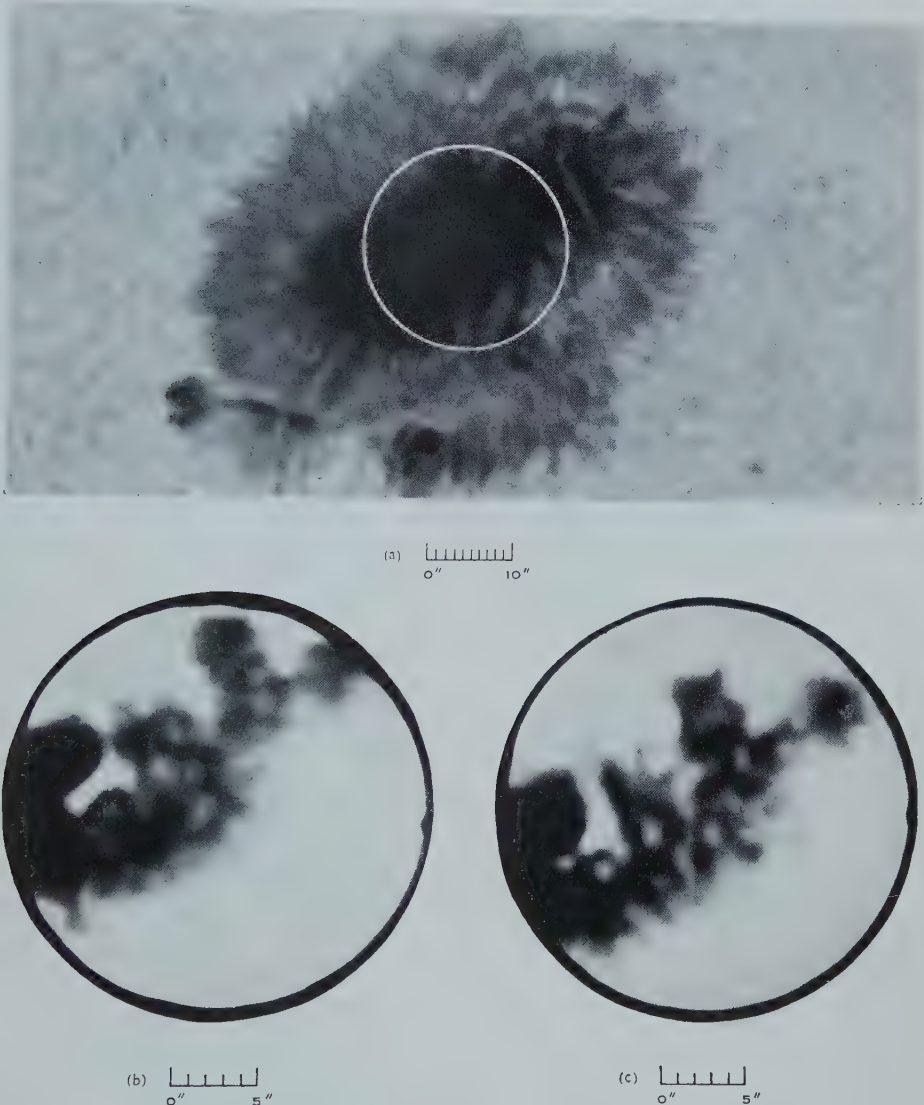
| Type of Change | No. of Granules |
|--------------------------------|-----------------|
| No change | 34 |
| Brightness { increase | 4 |
| | 4 |
| Size { increase | 1 |
| | 4 |
| Change of shape | 5 |

Comparison of Table 1 with the corresponding results for the photospheric granulation (Bray and Loughhead 1958b: cf. Table 2) suggests that rather more umbral than photospheric granules undergo no detectable change (71 per cent. as opposed to 57 per cent.). However, this may be an observational effect, since

* The significance of this result is established by the fact that the observed difference between the mean cell sizes, 0.6 sec, is six times greater than the standard error of the difference of the means, which is $\sqrt{(0.09)^2 + (0.06)^2} = 0.1$ sec, 0.09 and 0.06 sec being the standard errors of the means of the two distributions.

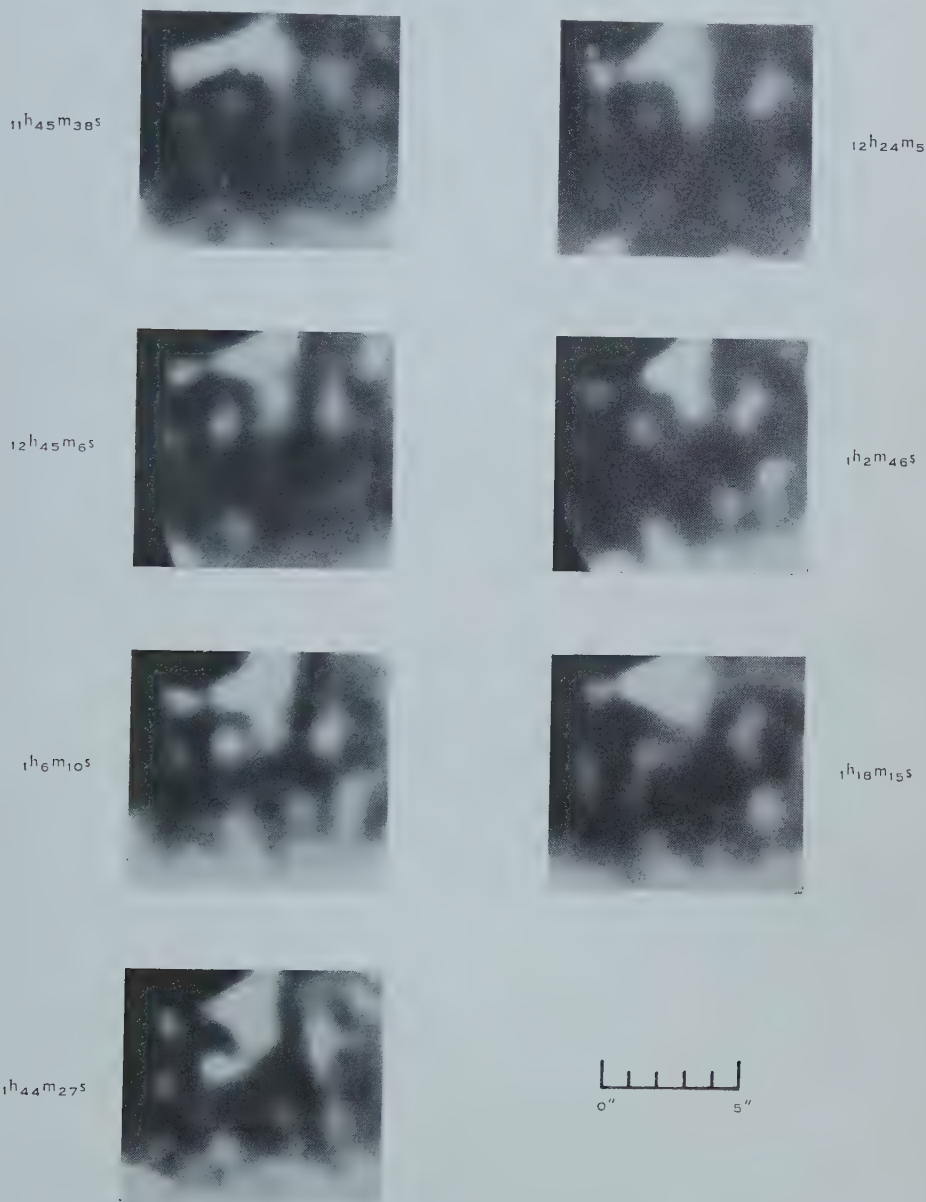
† The lifetimes of the longer-lived umbral granules are comparable with those of the penumbral filaments (Bray and Loughhead 1958a).

LIFETIME AND CELL SIZE OF SUNSPOT UMBRAL GRANULATION



The approximate position of the diaphragm relative to the spot is shown by the white circle. The scale of (b) and (c) is twice that of (a).

LIFETIME AND CELL SIZE OF SUNSPOT UMBRAL GRANULATION



A sequence of photographs showing the stability of the umbral granulation pattern over a period of $1^h\ 59^m$; the first two photographs are threefold overexposures, the rest are fivefold overexposures. Despite apparent changes due to seeing (e.g. the tail-like projections seen on several granules at $1^h\ 18^m\ 15^s$), some umbral granules can readily be followed over the entire sequence. Note the granule which becomes detached from the upper prong of the fork structure, and also the bright granule which ultimately attaches itself to the lower prong.

the smaller scale of the umbral pattern renders changes more difficult to detect. For those granules showing change, variations in brightness and size are uncorrelated and have no tendency to occur during any particular part of the observed lifetime.

Plate 2 illustrates the general stability of the umbral granulation pattern over a period of nearly 2 hr. Although there are apparent differences from one photograph to another due to seeing, some granules can easily be followed over the entire sequence. The "tails" attached to some of the granules at 1 hr 18 min 15 sec have no real existence but are due to poor seeing on this photograph.

Changes in the umbral granules are difficult to detect during their periods of formation and decay, when the granules cannot easily be identified as such. However, a few cases of well-defined births and deaths were recorded. Some granules are preceded by a diffuse patch of bright material, which is difficult to distinguish from a granule smeared by seeing. Others originate by detachment from the inner ends of penumbral filaments or from the tip of a "fork" structure (cf. Plate 2). Dissolution sometimes occurs by a granule fading into diffuse bright material, which may then become dark. Sometimes a granule loses its identity by coalescing with a neighbouring granule, penumbral filament, or fork structure (cf. Plate 2).

VI. DISCUSSION

The view that the photospheric granules are to be identified with convection cells is supported by two main lines of observational evidence: the cellular nature of the granulation pattern (Loughhead and Bray 1959; Schwarzschild and Schwarzschild 1959), and the observed correlation between brightness and line-of-sight velocity in the photosphere (Plaskett 1954; Stuart and Rush 1954). Although no measurements have yet been made of the velocities of umbral granules, the general similarity of the umbral granulation to the photospheric granulation suggests that it also may prove to have a convective origin. If so, the influence of the spot magnetic field on convection currents in its umbra may well be responsible for the smaller cell size actually observed (cf. Chandrasekhar 1952a), though it is not clear how the magnetic field would affect the lifetime. In addition, theory indicates that the retardation of the circulatory convection currents by the field would reduce—but not suppress—the transport of convective energy from the bottom of the hydrogen convection zone to the visible layers of the spot.

Biermann (1941) suggested that the upward transport of energy by convection in a spot would be completely suppressed by the field, while Hoyle (1949) pointed out that, assuming the material was constrained to follow the lines of force as they fan out near the surface, the convected energy would be distributed over a greater area than in the absence of a field. Chandrasekhar (1952b), on the other hand, has concluded that under solar conditions the onset of thermal instability in the presence of a magnetic field is characterized by oscillations of increasing amplitude rather than by cellular convection. Now that the existence of umbral

granulation is firmly established and some information about its lifetime and cell size is known, further work on the behaviour of convection currents in a magnetic field under solar conditions is clearly desirable.

VII. ACKNOWLEDGMENTS

The authors wish to thank Mr. D. G. Norton for assistance in securing the observations, and Mr. H. Gillett for processing the film and making the enlargements.

VIII. REFERENCES

- BIERMANN, L. (1941).—Cf. Cowling, T. G. (1953).—“The Sun.” (Ed. G. Kuiper.) p. 570. (Univ. Chicago Press.)
- BRAY, R. J., and LOUGHHEAD, R. E. (1958a).—*Aust. J. Phys.* **11**: 185.
- BRAY, R. J., and LOUGHHEAD, R. E. (1958b).—*Aust. J. Phys.* **11**: 507.
- BRAY, R. J., and LOUGHHEAD, R. E. (1959).—*Aust. J. Phys.* **12**: 320.
- CHANDRASEKHAR, S. (1952a).—*Phil. Mag.* **43**: 518–9.
- CHANDRASEKHAR, S. (1952b).—*Phil. Mag.* **43**: 529.
- HOYLE, F. (1949).—“Some Recent Researches in Solar Physics.” p. 11. (Cambridge Univ. Press.)
- LOUGHHEAD, R. E., and BRAY, R. J. (1959).—*Nature* **183**: 240.
- MACRIS, C. (1953).—*Ann. Astrophys.* **16**: 19.
- PLASKETT, H. H. (1954).—*Mon. Not. R. Astr. Soc.* **114**: 251.
- SCHWARZSCHILD, M., and SCHWARZSCHILD, B. (1959).—*Sci. Amer.* **200**: 52.
- STUART, F. E., and RUSH, J. H. (1954).—*Astrophys. J.* **120**: 245.

THE CHARACTERISTIC ELECTRON ENERGY LOSS SPECTRA OF ALUMINIUM-MAGNESIUM AND ALUMINIUM-COPPER ALLOYS

By C. J. POWELL*

[Manuscript received January 13, 1960]

Summary

The characteristic electron energy loss spectra of 1500 eV electrons scattered by aluminium-magnesium and aluminium-copper alloys have been measured. A plasma and a lowered plasma energy loss were observed in the alloys, and it was found that surface oxidation caused the disappearance of the lowered plasma loss and the appearance of a new modified lowered plasma loss. Though the compositions of the evaporated alloy specimens were unknown, the three energy losses were observed to vary continuously between the values observed for the three elements. This continuous change can be interpreted in terms of the changing free electron density in alloys of varying composition. It is concluded that measurements of the characteristic loss spectra of alloys can differentiate between losses due to individual and collective electron excitation.

I. INTRODUCTION

In a previous paper, possible reasons for the many discrepancies in the measurements of characteristic electron energy losses in solids by different workers have been discussed (Powell 1960*b*). New measurements in this laboratory have shown the source of some of these discrepancies and have enabled positive identification of the origin of many energy losses to be made. Before that work was carried out, however, it had been considered that an experiment which could be useful in determining the energy loss mechanism would be the measurement of the energy loss spectra of certain metal alloys.

It had been proposed that the dominant energy loss in a metal was due to the collective excitation of the conduction electrons (Pines 1956; Nozières and Pines 1958, 1959). For a free-electron gas, the energy loss is $\hbar\omega_p = \hbar(4\pi ne^2/m)^{1/2}$, where ω_p is the free-electron plasma frequency and n is the density of free electrons. Where the conduction electrons in a metal are weakly bound and the outermost core electrons strongly bound, the observed energy loss would be expected to be close to $\hbar\omega_p$ and the half-width of the loss small compared to $\hbar\omega_p$. In a metal where the binding energies of the valence and outermost core electrons are similar, the observed energy loss would be displaced appreciably from $\hbar\omega_p$ and the half-width of the loss peak would be of the order of $\hbar\omega_p$.

It had also been suggested that many of the energy losses were due to interband electronic transitions. Rudberg and Slater (1936) compared the loss spectrum of copper observed by Rudberg (1936) with one calculated from previous studies of the band structure, with fair agreement. More recently, Cauchois

* Department of Physics, University of Western Australia; present address: Imperial College of Science and Technology, London.

(1952), Watanabe (1954, 1956), and Leder, Mendlowitz, and Marton (1956) compared the energy losses observed in a number of elements with the displacements of subsidiary absorption maxima from the *K* and *L* edges in the X-ray absorption spectra. These authors found a degree of correlation between the loss values and the fine-structure displacements, and Leder, Mendlowitz, and Marton found some dependence of the energy losses on the inverse square of the lattice constant in elements of similar structure. Viatskin (1958) has also found fair agreement between some observed energy losses and values calculated using the interband transition hypothesis.

Measurements of the loss spectra of binary alloys of varying composition might therefore differentiate between these two mechanisms for the origin of a particular energy loss. If the dominant energy losses in two elements were due to plasma excitation, one might expect that a gradual shift in the energy loss with changing electron density would be observed in the alloy spectra. Alternatively, if the losses were due to interband transitions, it might be expected that the losses due to one element would gradually decrease in intensity while the losses characteristic of the second element gradually increased in intensity in alloys of increasing content of the second element, with possibly a small variation in each loss position caused by band structure changes. Alloys of aluminium, magnesium, and copper were chosen for investigation in the present work, as the dominant loss in each element had been identified as arising from plasma excitation by Nozières and Pines (1958, 1959) and had been correlated with the X-ray absorption fine structure by Leder, Mendlowitz, and Marton (1956). Further, the energy losses in aluminium and magnesium had been previously found to be sharp and in good agreement with the free-electron values of $\hbar\omega_p$, while the prominent loss in copper was broad and considerably different from $\hbar\omega_p$. The dominant losses in each element were well separated, occurring at approximately 10, 15, and 20 eV in magnesium, aluminium, and copper respectively, so that any gradual changes in the basic loss would be easily detectable.

Before the alloy experiments were performed, measurements of the loss spectra of each element were made. The results of such measurements have been discussed elsewhere (Powell and Swan 1959*a*, 1959*b*; Powell 1960*b*) and were sufficient in themselves to clearly identify the origin of the losses. Nevertheless, the alloy results to be presented are interesting and also confirm the previous interpretations. Some of the results from aluminium-magnesium alloys have already been described elsewhere (Powell 1960*a*).

The measurements of the loss spectra of aluminium and magnesium show that the loss spectra of each element consist entirely of combinations of two fundamental energy losses, 10.3 and 15.3 eV in aluminium, and 7.1 and 10.6 eV in magnesium. The larger loss in each metal was identified as the plasma loss and the smaller low-lying loss with the lowered plasma loss predicted to occur at $\hbar\omega_p/\sqrt{2}$ by Ritchie (1957). The copper spectrum was found to consist of a 7.2 eV lowered plasma loss, a 19.9 eV plasma loss, a 27.1 eV combination loss, and a loss of 4.4 eV considered to be due possibly to an intraband transition. Further work (Powell and Swan 1960; Powell 1960*b*) has shown that surface

oxidation of the specimens caused a rapid decrease in intensity of the lowered plasma loss and the appearance of a modified low-lying loss of 7.1 eV in aluminium, 4.9 eV in magnesium, and 3.7 eV in copper.

II. EXPERIMENTAL PROCEDURE

The characteristic loss spectra of electrons scattered through 90° by the targets were obtained with the 127° electrostatic electron spectrometer and apparatus previously described (Powell, Robins, and Swan 1958; Powell 1960a). After the target chamber had been gettered by several evaporations of either aluminium or magnesium, the alloy specimens were prepared by heating a helical tungsten filament on which strips of two elements had been placed. This procedure resulted in the deposition of alloys of unknown composition on the target surface and was adopted after attempts to prepare alloys by flash evaporation had proved unsuccessful. Though alloys of unknown composition were prepared by this technique, investigations of the loss spectra of each element had shown the necessity for unoxidized specimen surfaces. A primary electron energy of 1500 eV was used for all measurements.

III. RESULTS

After the simultaneous evaporation of either aluminium and magnesium or of aluminium and copper, a characteristic loss spectrum could be obtained which showed a prominent (plasma-type) loss and a low-lying loss. Typical loss spectra for the elements and the two types of alloys are shown in Figure 1. It was found that in no case could the observed spectra be regarded as arising from the superposition of the spectra of the corresponding pair of elements. It was therefore concluded that alloys had in fact been formed and that there was effectively no separate aggregation of the elements. From the consistency of the results it would also seem that the alloys must have been reasonably homogeneous.

The prominent loss in aluminium-magnesium alloys was observed to occur between 10.6 and 15.3 eV, the values of the plasma loss in magnesium and aluminium. Similarly, the prominent loss in aluminium-copper alloys occurred between 15.3 and 19.9 eV, the observed plasma losses in aluminium and copper. It was found that the low-lying loss changed its position concurrently with the prominent loss; whereas the low-lying loss increased as the plasma-type loss increased in aluminium-magnesium alloys, it decreased in aluminium-copper alloys as the plasma-type loss increased. The continuous changes in the dominant loss and the low-lying loss between the positions observed in the elements confirm the previous identifications as plasma loss and lowered plasma loss respectively. The variations in the lowered plasma loss are plotted in Figure 2 (b) as a function of the observed plasma energy loss.

As the alloy specimens oxidized, the lowered plasma loss decreased in intensity and was replaced by a modified low-lying loss, as in the elements. The observed modified low-lying loss is plotted against the corresponding plasma loss in Figure 2 (a); it is also seen to increase with the plasma loss in the aluminium-magnesium alloys and to decrease in the aluminium-copper alloys.

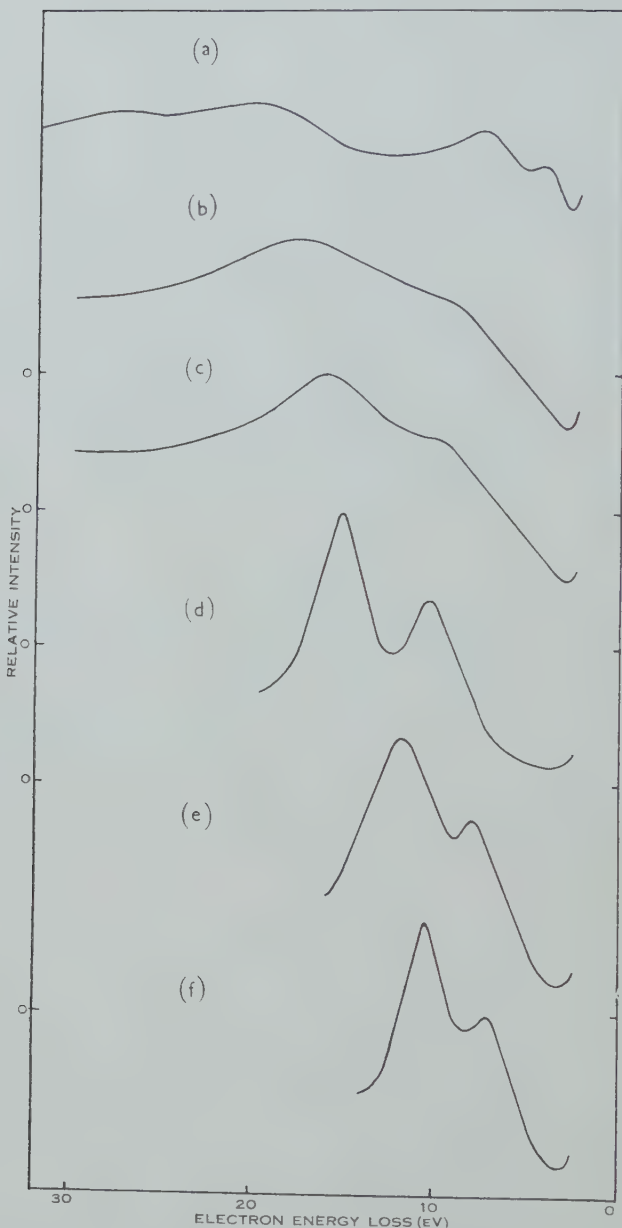


Fig. 1.—Representative portions of characteristic loss spectra of aluminium-magnesium and aluminium-copper alloys together with the loss spectra of the three elements, recorded with a primary electron energy of 1500 eV. Curve (a) is the spectrum of copper, curves (b) and (c) are spectra of aluminium-copper alloys, curve (d) is the spectrum of aluminium, curve (e) is a spectrum of an aluminium-magnesium alloy, and curve (f) is the spectrum of magnesium. The spectra have been drawn so that the plasma peak has the same intensity in all cases.

It was found that the width of the plasma loss peak at half maximum intensity varied considerably in the alloys and the measured half-width is plotted against plasma energy loss in Figure 3 (b). As the half-width of the peak of elastically scattered electrons was 1.9 eV, the true breadth of the plasma peak increased by a maximum factor of approximately 2.5 in the aluminium-

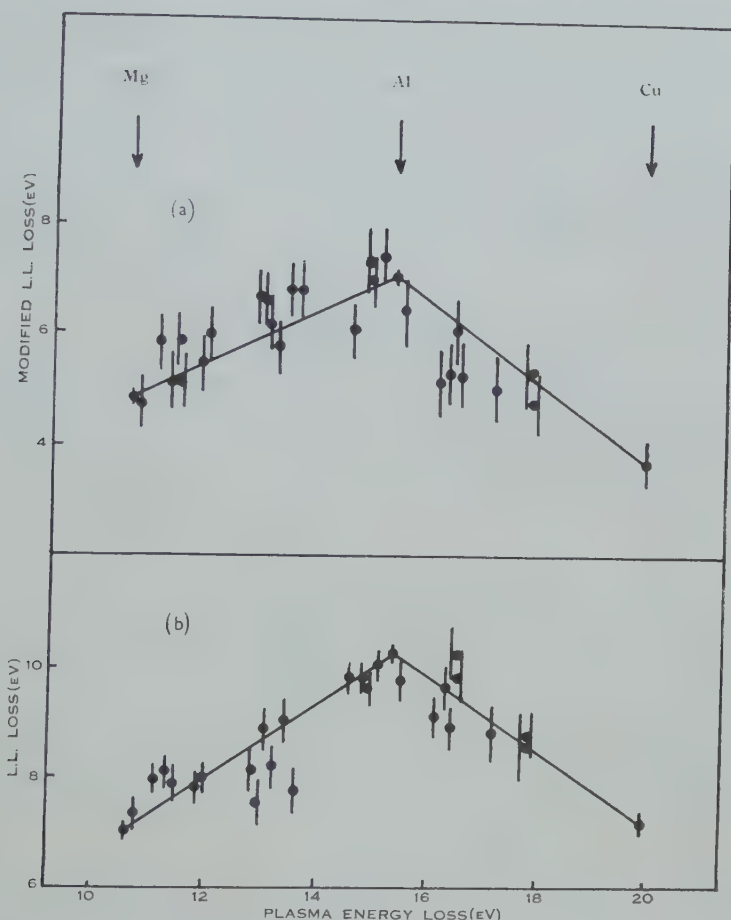


Fig. 2.—The observed modified low-lying loss (a) and the low-lying loss (b) plotted as a function of the corresponding plasma energy loss for aluminium-magnesium and aluminium-copper alloys. Straight lines have been drawn between the points corresponding to the energy losses observed in the elements and are not intended to imply a fit of the alloy data. The probable error in the abscissa is ± 0.2 eV.

magnesium alloys and by a maximum factor of about 9 in the aluminium-copper alloys. In contrast, there is only a gradual increase in the half-width of the lowered plasma loss, as shown in Figure 3 (a). It should be noted that the large errors in the half-widths of the aluminium-copper alloy loss peaks, due to the difficulty in locating the continuous background of inelastically scattered electrons, preclude a more accurate measurement of the half-width variations.

IV. DISCUSSION

It has been found that the loss spectra of aluminium-magnesium and aluminium-copper alloys do not simply arise as combinations of the spectra of the constituent elements. This observation is similar to that of Gauthé (1959), who has recently investigated the loss spectra of several intermetallic compounds.

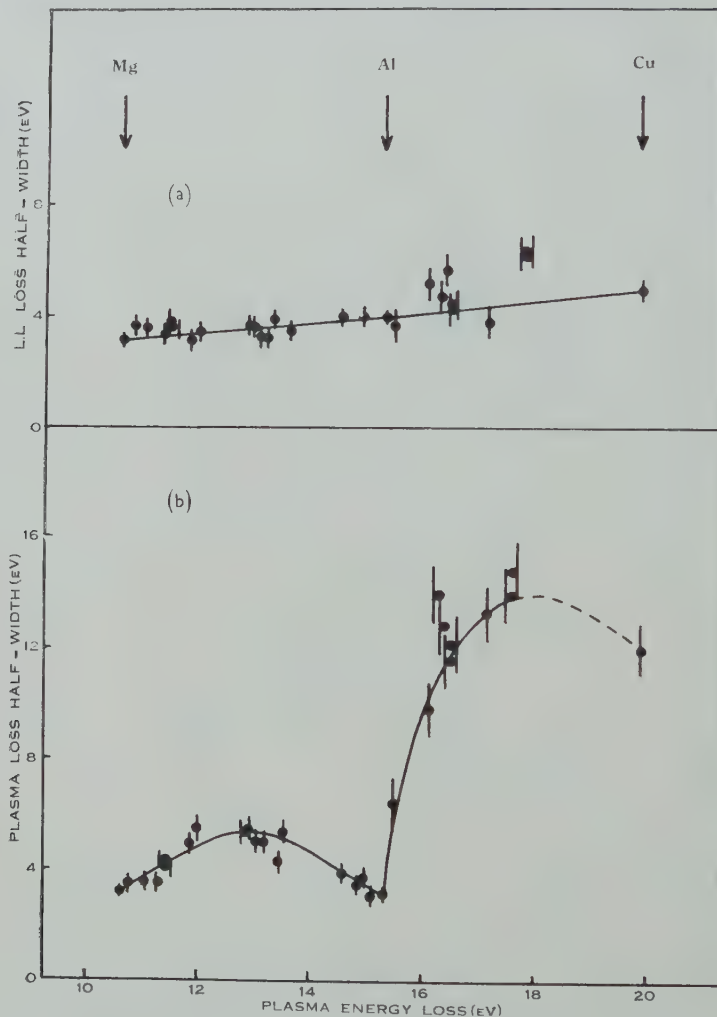


Fig. 3.—The width at half-maximum intensity of the low-lying loss (*a*) and the plasma loss (*b*) as a function of the plasma energy loss. Straight lines have been drawn through the points corresponding to the values observed for the elements in (*a*) and are not intended to represent a fit of the alloy data.

Further, the alloy spectra show a plasma and a lowered plasma loss which both vary continuously between the values observed in the elements. These gradual changes in the energy losses, presumably with composition, confirm the previous collective interpretation of the origin of the losses.

It was suggested in a previous paper (Powell 1960b) that the lowered plasma loss could indicate the effective free-electron density in the specimens. This view appears to be confirmed by the observed decrease in the lowered plasma loss with increasing plasma loss in the aluminium-copper alloys. As stated in the introduction, the position of the plasma loss may be determined by considerations other than the free-electron density. Where the plasma loss is displaced from the value estimated using the free-electron density, a large increase in breadth of the loss peak is to be expected. The plasma loss peak in aluminium-copper alloys is thus observed to increase from that found in aluminium, even though the lowered plasma loss and the calculated free-electron density are decreasing. The large increase in breadth of the plasma loss peak is therefore consistent with this interpretation. It is also possible that part of the observed increase in breadth is due to the fact that the conduction electrons are not moving in a uniform lattice in the alloys; variations in the interaction between these electrons and the two types of ions could cause a broadening of the loss peak.

V. CONCLUSION

Measurements of the characteristic loss spectra of aluminium-magnesium and aluminium-copper alloys have shown continuous changes in the positions of the plasma and lowered plasma energy losses found in the elements. Though the alloy compositions were unknown, these variations in the energy losses confirm the previous identifications. It would be of some interest in any future investigation to endeavour to find the relation between loss position and alloy composition.

The present results also show that an investigation of the characteristic loss spectra of alloys can indicate the origin of the energy losses. Though the energy losses in aluminium, magnesium, and copper had been previously identified, the alloy measurements differentiated between the individual particle and collective nature of the origin of the losses. If the loss spectrum of a particular element was so complicated that the origin of the losses could not be otherwise determined, it could be useful to alloy that element with another element whose spectrum was known in order to distinguish between the losses of different origin.

VI. ACKNOWLEDGMENTS

The author would like to thank Dr. J. B. Swan for his continuous interest and encouragement during this work. He also appreciates the suggestions for improving the manuscript given by Dr. Swan and Professor C. J. B. Clews. The author finally wishes to acknowledge the tenure of a C.S.I.R.O. Senior Post-graduate Studentship and the support of the research by the Research Grants Committee of the University of Western Australia.

VII. REFERENCES

- CAUCHOIS, Y. (1952).—*Acta Cryst.* **5**: 351.
GAUTHÉ, B. (1959).—*Phys. Rev.* **114**: 1265.
LEDER, L. B., MENDLOWITZ, H., and MARTON, L. (1956).—*Phys. Rev.* **101**: 1460.
NOZIÈRES, P., and PINES, D. (1958).—*Phys. Rev.* **109**: 1062.
NOZIÈRES, P., and PINES, D. (1959).—*Phys. Rev.* **113**: 1254.
PINES, D. (1956).—*Rev. Mod. Phys.* **28**: 184.

- POWELL, C. J. (1960a).—*J. Plasma Physics, Accelerators, Thermonuclear Research* (In press.)
POWELL, C. J. (1960b).—*Proc. Phys. Soc.* (In press.)
POWELL, C. J., ROBINS, J. L., and SWAN, J. B. (1958).—*Phys. Rev.* **110**: 657.
POWELL, C. J., and SWAN, J. B. (1959a).—*Phys. Rev.* **115**: 869.
POWELL, C. J., and SWAN, J. B. (1959b).—*Phys. Rev.* **116**: 81.
POWELL, C. J., and SWAN, J. B. (1960).—*Phys. Rev.* (In press.)
RITCHIE, R. H. (1957).—*Phys. Rev.* **106**: 874.
RUDBERG, E. (1936).—*Phys. Rev.* **50**: 138.
RUDBERG, E., and SLATER, J. C. (1936).—*Phys. Rev.* **50**: 150.
VIATSKIN, A. Ia. (1958).—*Soviet Physics, Technical Physics* **3**: 2252.
WATANABE, H. (1954).—*J. Phys. Soc. Japan* **9**: 920.
WATANABE, H. (1956).—*J. Phys. Soc. Japan* **11**: 112.

IONOSPHERIC REFRACTION IN RADIO ASTRONOMY

I. THEORY

By M. M. KOMESAROFF*

[*Manuscript received January 13, 1960*]

Summary

Expressions are derived for the apparent displacements of cosmic radio sources at transit resulting from ionospheric refraction. The derivation takes account of horizontal electron density gradients whose effects often outweigh the refraction expected from a spherically symmetrical ionosphere.

Using these results together with position measurements taken at 19.7 Mc/s, the "total thickness" of the ionosphere has been estimated. This quantity relates the total electron content of a vertical column to the maximum electron density. During the observing period it had a value of 355 km, in good agreement with moon-echo results. The observations also indicate that a considerable improvement in observed source positions may be achieved by applying the theory.

I. INTRODUCTION

Ionospheric refraction may seriously limit the accuracy of wide-aperture radio-astronomy aerials operating at low frequencies. A number of authors, notably Bailey (1948), Belyaev (1955), Link (1957), and Chvojkova (1958a and 1958b), have estimated this refraction assuming that the ionosphere is a spherical shell concentric with the Earth. Smith (1952), on the other hand, has shown that horizontal density gradients lead to appreciable displacements of sources at the zenith, indicating that an adequate theory must take account of departures from spherical symmetry.

The present calculation shows that, for a source at transit, the change of declination depends on the total electron content of a column of unit area through the ionosphere, together with the north-south gradient of this quantity. The change of Right Ascension depends to a first order only on the east-west gradient.

The investigation had a twofold aim. It was originally prompted by the need to eliminate refraction effects from galactic records taken with a Mills Cross operating as a transit instrument at 19.7 Mc/s. For this it was necessary to relate observed displacements of discrete sources to published ionospheric sounding data. This was accomplished, and also information was gained about the structure of the ionosphere above the *F*-region maximum.

This paper deals mainly with the theoretical aspect of the problem and includes an estimate of errors in the necessarily approximate treatment. A brief discussion of some experimental results shows that the derived value of ionospheric "total electron content" is in good agreement with estimates derived by

* Division of Radiophysics, C.S.I.R.O., University Grounds, Chippendale, N.S.W.

other methods, and also indicates the improvement to the astronomical data which may be attained using the derived corrections.

A preliminary report on this work has been given previously (Komesaroff and Shain 1959).

II. DEFINITIONS OF THE MAIN SYMBOLS USED

The more important symbols used are defined as follows:

- N , number of electrons per cubic centimetre,
- f , frequency of observation,
- f_c , critical frequency of the F region,
- $X_m, f_c^2/f^2$,
- r , distance to the Earth's centre,
- r_m , radius of the surface of maximum electron density,
- r_b , radius of the lower ionospheric bounding surface,
- φ , terrestrial latitude (radians),
- Φ , latitude of observer,
- L , longitude to the east of the observer (radians),
- k , angle between ray tangent and radius vector,
- Z , observed zenith angle,
- δ , declination,
- α , Right Ascension,
- y_m, y'_m , " semithicknesses " of regions above and below maximum density (parabolic model),
- d , total effective thickness; $d = \frac{2}{3}(y_m + y'_m)$.

III. RAY PATHS IN THE IONOSPHERE

In discussing ionospheric parameters a spherical coordinate system, r, φ, L , is used with origin at the centre of the Earth, φ being latitude and L longitude measured to eastward from the observer. Records of critical frequency taken at different places show that the refractive index varies not only with r but also with φ and L . Thus the optical length of a ray path between points a and b is

$$\begin{aligned} P &= \int_a^b \mu(r, \varphi, L) ds \\ &= \int_a^b [1 + r^2 \dot{\varphi}^2 + r^2 \dot{L}^2 \cos^2 \varphi]^{\frac{1}{2}} \mu(r, \varphi, L) dr, \end{aligned}$$

where $\dot{\varphi} = d\varphi/dr$ and $\dot{L} = dL/dr$.

From Fermat's principle, the differential of P with respect to changing ray paths is zero, and this leads to the following ray equations:

$$\frac{d}{dr} \left(\mu r^2 \frac{d\varphi}{ds} \right) = \frac{ds}{dr} \left[\frac{\partial \mu}{\partial \varphi} - \mu r^2 \frac{dL}{ds} \sin \varphi \cos \varphi \right], \quad \dots \dots \dots \quad (1)$$

$$\frac{d}{dr} \left(\mu r^2 \cos^2 \varphi \frac{dL}{ds} \right) = \frac{ds}{dr} \frac{\partial \mu}{\partial L}. \quad \dots \dots \dots \quad (2)$$

From these equations the refraction produced by any model ionosphere may be calculated.

Following Ratcliffe (1951) we will assume a density distribution of electrons below the maximum value N_m ,

$$N = N_m(1 - y^2/y_m^2), \quad \dots \dots \dots \quad (3)$$

where y is the distance from the maximum density layer and the scale factor y_m is of the order of 100 km. A corresponding expression is adopted for the distribution above the maximum, y_m being replaced by y'_m , where, according to the moon-echo work of Evans (1957), y'_m is several times larger than y_m , and

$$y_m + y'_m \approx 0.1 r_m,$$

r_m being the radius of the maximum density layer.

For a radio wave of frequency f , well above the electron gyro frequency (usually the case in radio-astronomical work), the refractive index is given by

$$\mu^2 = 1 - f_p^2/f^2 = 1 - X, \quad \dots \dots \dots \quad (4)$$

where f_p^2 , the square of the "plasma frequency", is proportional to N . Thus from (3)

$$\mu^2 = 1 - X_m(1 - y^2/y_m^2). \quad \dots \dots \dots \quad (5)$$

In terms of the F -layer critical frequency f_c , X_m is defined by

$$X_m = f_c^2/f^2.$$

Now, assuming that the scale factors y_m , y'_m are substantially constant over large distances, then corresponding to horizontal density gradients we have refractive index gradients given by

$$\frac{\partial \mu}{\partial \varphi} = \frac{-1}{2\mu} \frac{\partial X_m}{\partial \varphi} \left(1 - \frac{y^2}{y_m^2}\right), \quad \dots \dots \dots \quad (6)$$

$$\frac{\partial \mu}{\partial L} = \frac{-1}{2\mu} \frac{\partial X_m}{\partial L} \left(1 - \frac{y^2}{y_m^2}\right). \quad \dots \dots \dots \quad (7)$$

In the subsequent argument it will be assumed that these partial derivatives of X_m are constant over small angular ranges.

IV. THE APPARENT CHANGE OF DECLINATION

The discussion will be limited to the case of a source at transit. Let us first assume that there are no east-west refractive index gradients, so that the observed ray lies entirely in the meridian plane. Later it will be shown that the effect of these gradients on observed declinations is negligible.

(a) The Two Refraction Components

In Figure 1, ABC is part of a ray path. The ray tangent at B , in latitude φ , makes an angle k with the radius vector to the centre of the Earth O . It follows from the figure that the apparent declination of the source as seen from B is D , where

$$D = \varphi + k. \quad \dots \dots \dots \quad (8)$$

It also follows that

$$\sin k = r d\phi / ds, \dots \quad (10)$$

and

$$(\tan k)/r = d\phi/dr. \quad \dots \dots \dots \quad (11)$$

In Figure 2, $QRST$ is a ray from a distant source to a terrestrial observer at T . The upper and lower ionospheric bounding radii are $(r_m + y_m)$ and $(r_m - y_m)$ respectively. The true declination δ of the source is indicated by the direction



Fig. 1.—Section of a ray path in the meridian plane. OP is the equatorial plane and angle D is the apparent declination of the source seen from point B in latitude ϕ .

of the ray at the point Q at which it intersects the upper boundary. Denoting the values of angles at this level by the suffix a , it follows from (8) and (11) that

$$\delta = \Phi + \int_{r_a}^{r_m + y'_m} \frac{\tan k}{r} dr + k_a, \dots \quad (12)$$

where Φ is the observer's latitude and r , the radius of the Earth.

The straight line TU indicates the apparent declination δ_0 as seen from T . Denoting the angle between TU and the radius vector at any level by k , it may

be seen that the value of δ_0 is given by a relation formally identical with (12), namely,

$$\delta_0 = \Phi + \int_{r_e}^{r_m + y'_m} \frac{\tan k_0}{r} dr + k_{0a}. \quad \dots \dots \dots \quad (13)$$

Thus the difference $\Delta(\delta)$ between the apparent and true declination is given by

$$\Delta(\delta) = \delta_0 - \delta = k_{0a} - k_a + \int_{r_m - y_m}^{r_m + y'_m} \frac{(\tan k_0 - \tan k)}{r} dr, \quad \dots \dots \dots \quad (14)$$

(since $k = k_0$ when r lies between r_e and $r_m - y_m$). The equation for k_0 is

$$r \sin k_0 = r_e \sin Z = r_m \sin k_{0m}. \quad \dots \dots \dots \quad (15)$$

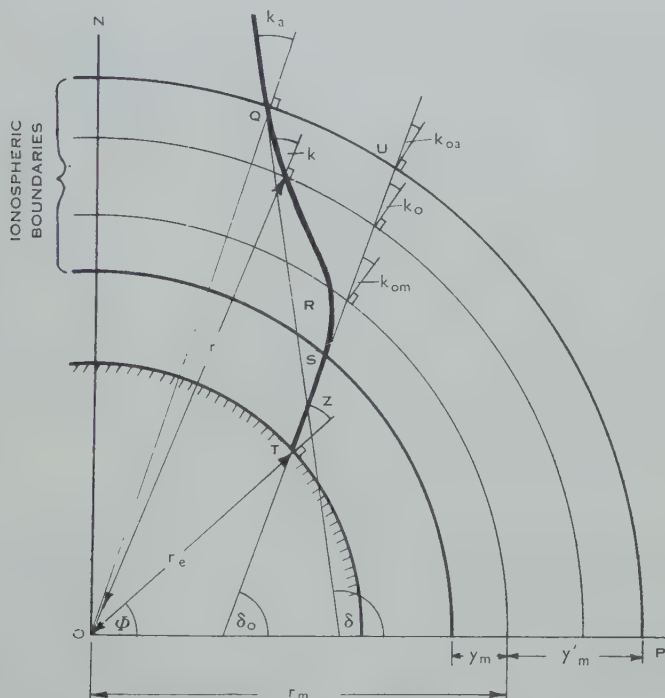


Fig. 2.—Path of a ray through the ionosphere to an observer at T . OP is the equatorial plane. (Not to scale.)

Here Z is the apparent zenith angle of the source and the suffix m denotes the value of a parameter at the level of maximum electron density. To calculate k we must refer to the ray equation (1). Since according to our assumption there are no east-west gradients, this reduces to

$$\frac{d}{dr} \left(\mu r^2 \frac{d\varphi}{ds} \right) = \frac{ds}{dr} \frac{\partial \mu}{\partial \varphi}.$$

Integrating and combining this equation with (9), (10), and (15) yields

$$\mu r \sin k = r_m \sin k_{0m} + \int_{r_m - y_m}^r \sec k \frac{\partial \mu}{\partial \varphi} dr. \quad \dots \dots \dots \quad (16)$$

Now taking into account that $\mu=1$ at the upper boundary, it follows from (14), (15), and (16) that

$$\Delta(\delta)=\Delta(\delta)_w+\Delta(\delta)_s,$$

where

$$\Delta(\delta)_w=k_{0a}-\sin^{-1}\left[\sin k_{0a}+\left(\frac{1}{r_m+y'_m}\right)\int_{r_m-y_m}^{r_m+y'_m} \sec k \frac{\partial \mu}{\partial \varphi} dr\right], \dots \quad (17)$$

$$\Delta(\delta)_s=\int_{r_m-y_m}^{r_m+y'_m} \frac{(\tan k_0-\tan k)}{r} dr, \dots \quad (18)$$

and

$$\sin k_{0a}=r_m \sin k_{0m}/(r_m+y'_m). \dots \quad (19)$$

In substituting the value of k from (16) into (17) and (18), a simplifying approximation may be made. Provided k nowhere exceeds about 45° , and the values of $\partial \mu / \partial \varphi$ are such that the second term on the right-hand side of (16) is "small", that is, provided

$$\frac{1}{\mu r} \int \sec k \frac{\partial \mu}{\partial \varphi} \lesssim \frac{\cos k_{0m}}{30} dr, \dots \quad (20)$$

we may neglect this term in (16), giving

$$\sin k=r_m \sin k_{0m}/\mu r. \dots \quad (21)$$

The restriction imposed by inequality (20) will be discussed subsequently. It may be shown that the approximation which we have made results in an error equivalent to an underestimate of $\Delta(\delta)_w$ of the order

$$\{(y_m+y'_m)/r_m\} \Delta(\delta)_w.$$

Thus the total north-south displacement of a source at transit is expressible as the sum of two terms given by (17) and (18). The term $\Delta(\delta)_w$, which will be designated the "wedge component", depends on angular gradients of refractive index and vanishes in the limiting case of spherical symmetry. The term $\Delta(\delta)_s$, depends to a first order only on the radial distribution and represents the refraction calculated for a spherically symmetrical medium. Accordingly it is called the "spherical component". Each of these terms is evaluated below. It is later shown that the wedge component is commonly predominant, indicating that previous treatments of the problem based on a spherically symmetrical model lead to erroneous results.

(b) The Wedge Component

Equation (17) may be simplified by a minor approximation. From (19),

$$k_{0a} \approx k_{0m},$$

and, since the integral term has been assumed "small", (17) may be restated thus

$$\Delta(\delta)_w=\frac{-\sec k_{0m}}{(r_m+y'_m)} \int_{r_m-y_m}^{r_m+y'_m} \sec k \frac{\partial \mu}{\partial \varphi} dr. \dots \quad (22)$$

An expression for $\sec k$ may be derived from (4), (5), and (21). If M is defined by the relation

$$M = [1 - X \sec^2 k_{0m}]^{-\frac{1}{2}} = [1 - X_m \sec^2 k_{0m} (1 - y^2/y_m^2)]^{-\frac{1}{2}} \dots (23)$$

then it may be shown that

$$\sec k = \mu M \sec k_{0m} [1 + (1 - r_m^2/r^2) M^2 \tan^2 k_{0m}]^{-\frac{1}{2}}. \dots (24)$$

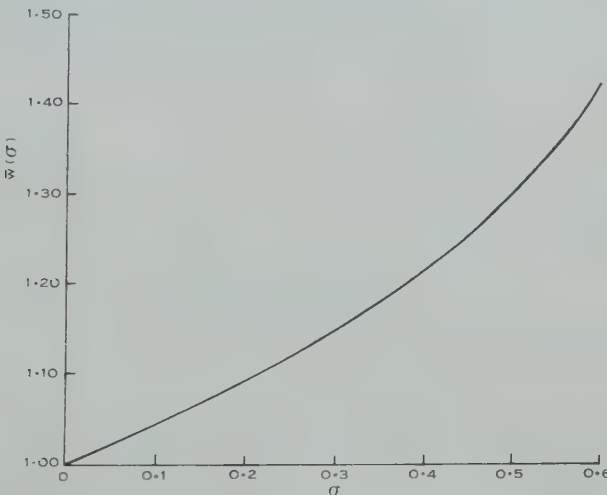


Fig. 3.—Graph of the function
 $\bar{w}(\sigma) = \frac{3}{4\sigma} \left\{ \left[(1+\sigma)/2\sigma^{\frac{1}{2}} \right] \ln \left[\left(1+\sigma^{\frac{1}{2}} \right) / \left(1-\sigma^{\frac{1}{2}} \right) \right] - 1 \right\},$
where $\sigma = (f_c^2/f^2) \sec^2 k_{0m}$.

Now, provided $k_{0m} \lesssim 45^\circ$ and $\sigma \lesssim \frac{1}{2}$, where σ is defined by

$$\sigma = X_m \sec^2 k_{0m},$$

the value of the surd in (24) is very nearly unity throughout the range of integration. Thus from (22) and (24) we derive the approximation

$$\Delta(\delta)_w = \frac{-\sec^2 k_{0m}}{r_m + y'_m} \int_{r_m - y_m}^{r_m + y'_m} M \mu \frac{\partial \mu}{\partial \varphi} dr.$$

Substituting from (5), (6), and (23) and integrating,

$$\Delta(\delta)_w = \frac{(y_m + y'_m) \cdot \bar{w}(\sigma) \sec^2 k_{0m}}{3(r_m + y'_m)f^2} \cdot \frac{\partial(f_c^2)}{\partial \varphi}, \dots (25)$$

where

$$\bar{w}(\sigma) = \frac{3}{4\sigma} \left\{ \frac{(1+\sigma)}{2\sigma^{\frac{1}{2}}} \ln \left(\frac{1+\sigma^{\frac{1}{2}}}{1-\sigma^{\frac{1}{2}}} \right) - 1 \right\}. \dots (26)$$

The parameter $\bar{w}(\sigma)$ is shown as a function of σ in Figure 3. For values of σ lying between 0 and $\frac{1}{2}$, $\bar{w}(\sigma)$ lies between 1 and 1.3.

The error of approximation in going from (17) to (25) is equivalent to an overestimate of about $\{y_m + y'_m\}/r_m \Delta(\delta)_w$. Since the error mentioned in Section III (a) was of similar magnitude but opposite sign, the total approximation error is generally less than $\{(y_m + y'_m)/r_m\} \Delta(\delta)_w$, or one part in ten.

The foregoing results have been derived on the assumption that the vertical distribution of electron density has a parabolic form. However, it may be shown that (25) can be generalized to cover any form of vertical profile, provided that this is a smoothly varying function and has a reasonably sharp upper boundary. For the general form we introduce the "effective thickness" d of the ionosphere given by

$$dN_m = \int N dr, \quad \dots \dots \dots \quad (27)$$

so that for a parabolic layer

$$d = \frac{2}{3}(y_m + y'_m).$$

Equation (25) then becomes

$$\Delta(\delta)_w = \frac{d\bar{w}(\sigma) \sec^2 k_{0m}}{2(r_b + 3d/2)f^2} \frac{\partial(f_e^2)}{\partial\varphi}, \quad \dots \dots \dots \quad (28)$$

where r_b is the inner bounding radius of the ionosphere.

(c) The Spherical Component

To evaluate the integral in equation (18) we require an expression for $\tan k$. From (21) and (24),

$$\tan k = (r_m/r)M \tan k_{0m} [1 + (1 - r_m^2/r^2)M^2 \tan^2 k_{0m}]^{-\frac{1}{2}}.$$

If now M is replaced by \bar{M} , its mean value for the range of integration, and the resulting value of $\tan k$ substituted in (18), it may be shown that this gives a close approximation to $\Delta(\delta)_s$,

$$\begin{aligned} \Delta(\delta)_s &= \int_{r_m - y_m}^{r_m + y'_m} \frac{r_m \tan k_{0m}}{r^2} \\ &\quad \times \left\{ \left[1 + \left(1 - \frac{r_m^2}{r^2} \right) \tan^2 k_{0m} \right]^{-\frac{1}{2}} - \bar{M} \left[1 + \left(1 - \frac{r_m^2}{r^2} \right) \bar{M}^2 \tan^2 k_{0m} \right]^{-\frac{1}{2}} \right\} dr \\ &= \sin^{-1} \left[\frac{r_m \sin K}{r_m + y'_m} \right] - \sin^{-1} \left[\frac{r_m \sin K}{r_m - y_m} \right] - \sin^{-1} \left[\frac{r_m \sin k_{0m}}{r_m + y'_m} \right] + \sin^{-1} \left[\frac{r_m \sin k_{0m}}{r_m - y_m} \right]. \end{aligned} \quad \dots \dots \dots \quad (29)$$

Here K is given by

$$\tan K = \bar{M} \tan k_{0m},$$

and

$$\begin{aligned} \bar{M} &= \frac{1}{y_m} \int_{-y_m}^0 M dy = \frac{1}{y'_m} \int_0^{y'_m} M dy = \frac{1}{y_m + y'_m} \int_{-y_m}^{y'_m} M dy \\ &= \frac{1}{2\sigma^{\frac{1}{2}}} \ln \left(\frac{1 + \sigma^{\frac{1}{2}}}{1 - \sigma^{\frac{1}{2}}} \right). \end{aligned} \quad \dots \dots \dots \quad (30)$$

The parameter \bar{M} is shown as a function of σ in Figure 4.

The error in approximation (29) is

$$\int_{r_m-y_m}^{r_m+y'_m} \frac{r_m \tan k_{0m}}{r^2} \times \left\{ \bar{M} \left[1 + \left(1 - \frac{r_m^2}{r^2} \right) \bar{M}^2 \tan^2 k_{0m} \right]^{-\frac{1}{2}} - M \left[1 + \left(1 - \frac{r_m^2}{r^2} \right) M^2 \tan^2 k_{0m} \right]^{-\frac{1}{2}} \right\} dr.$$

By expressing the integrand as a first-order Taylor expansion in $(\bar{M} - M)$, it may be shown that the ratio of this error term to $\Delta(\delta)_s$, given by (29), is considerably less than $(y_m + y'_m)/r_m$.

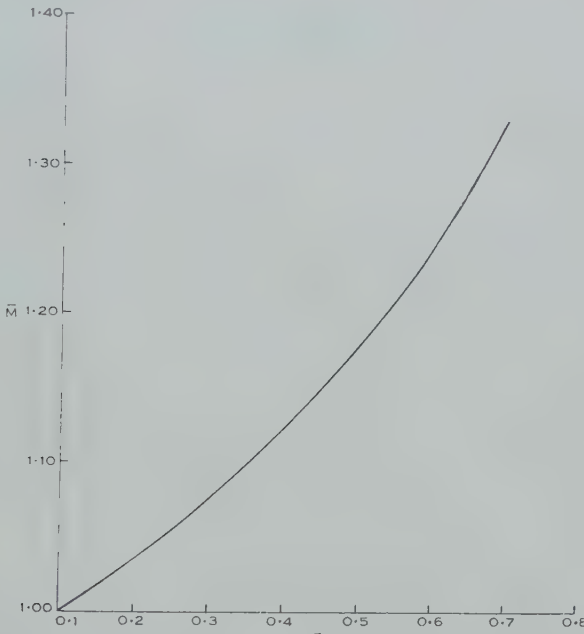


Fig. 4.—Graph of the function $\bar{M} = (1/2\sigma^{\frac{1}{2}}) \ln [(1+\sigma^{\frac{1}{2}})/(1-\sigma^{\frac{1}{2}})]$.

In Figure 5, $\Delta(\delta)_s$ is shown as a function of k_{0m} according to equation (29). This figure also includes a graph relating k_{0m} to the apparent zenith angle Z (from (15)). Figure 5 is based on a model ionosphere for which

$$y_m = 0.018r_m = 120 \text{ km}, \\ y'_m = 0.062r_m = 410 \text{ km}.$$

For values of y_m and y'_m differing slightly from the above, $\Delta(\delta)_s$ may be calculated by assuming a linear relation with the total thickness.

In some applications a less accurate expression than (29) is adequate. Thus at high frequencies and for moderate values of k_{0m} , the following relation may be derived from (29)

$$\Delta(\delta)_s = -\frac{d}{2r_m} \frac{f_c^2}{f^2} \sec^2 k_{0m} \tan k_{0m}. \dots \dots \dots \quad (31)$$

This equation, due originally to Chvojkova (1958a, 1958b), is very convenient for rapid numerical calculation.

Numerical values of $\Delta(\delta)_s$ may be computed by graphical integration of the general refraction integral

$$\int \frac{\tan i}{\mu} d\mu$$

taken in conjunction with equation (21). In Table 1 a number of values calculated in this way are presented, together with corresponding values from equation (29). For comparison, results given by Chvojkova's equation (31) and an equation due to Bailey (1948), are also quoted (the last example quoted is one

TABLE 1
THE SPHERICAL COMPONENT

| k_{0m} | $\frac{f_c^2}{f^2}$ | y'_m (km) | y_m (km) | $r_m - r_e$ (km) | $-\Delta(\delta)_s$ | | | |
|-----------|---------------------|----------------|---------------|---------------------|---------------------|-----------|-----------|------------------|
| | | | | | Bailey | Chvojkova | Eqn. (29) | Graph. Integ. |
| 25° 35.9' | 0.25 | 330 | 100 | 300 | 11.1' | 11.0' | 13' | 13.1' |
| 30° | 0.1875 | 561 | 198 | 300 | 19.1' | 19' | 21' | 21.4' |
| 45° | 0.25 | 495 | 99 | 300 | 51.9' | 51.6' | 1° 5.7' | 1° 7.6' |
| 45° | 0.25 | 660 | 165 | 300 | 1° 12' | 1° 11.6' | 1° 29' | 1° 30' |
| 70° 42.2' | 0.0576 | 375 | 75 | 375 | 1° 8' | 1° 4' | 1° 25.1' | 1° 26.6' |

which Bailey considers). It can be seen that equation (29) yields an accuracy five to ten times better than the other equations. However, world maps of critical frequency show that in moderate latitudes $\partial(f_c^2)/\partial\phi$ often far exceeds f_c^2 , so that from (28) and (31)

$$\Delta(\delta_w) \gg \Delta(\delta)_s.$$

Under these conditions, $\Delta(\delta)$ may be calculated using the less accurate form of $\Delta(\delta)_s$ without significant loss of overall accuracy.

(d) The Total Change of Declination

Combining equations (28) and (31), the angle $\Delta(\delta)$ by which the observed declination of a source at transit exceeds its true declination is given by

$$\Delta(\delta) = \frac{d \sec^2 k_{0m}}{2(r_b + 3d/2)f^2} \left[\bar{w}(\sigma) \frac{\partial(f_c^2)}{\partial\phi} - \frac{(r_b + 3d/2)}{r_m} f_c^2 \tan k_{0m} \right], \quad \dots \quad (32)$$

which may be written

$$\Delta(\delta) = \frac{d \sec^2 k_{0m}}{2(r_b + 3d/2)f^2} R(\delta) \quad \dots \quad (33)$$

(for k_{0m} , d , and $\bar{w}(\sigma)$ see equations (15) and (27) and Figure 3).

Equation (32) has an accuracy of about one part in ten for sources up to about 45° from the zenith assuming that f is not less than $2\frac{1}{2}f_c \sec k_{0m}$. This is not a serious restriction since radiation of frequencies less than $f_c \sec k_{0m}$ cannot be observed.

The derivation of (32) also assumes that the first term on the right-hand side considerably outweighs the second. When this condition is not satisfied, a more accurate approximation to the second term, given by (29), should be used. When the condition is satisfied, however, it is noteworthy that the source displace-

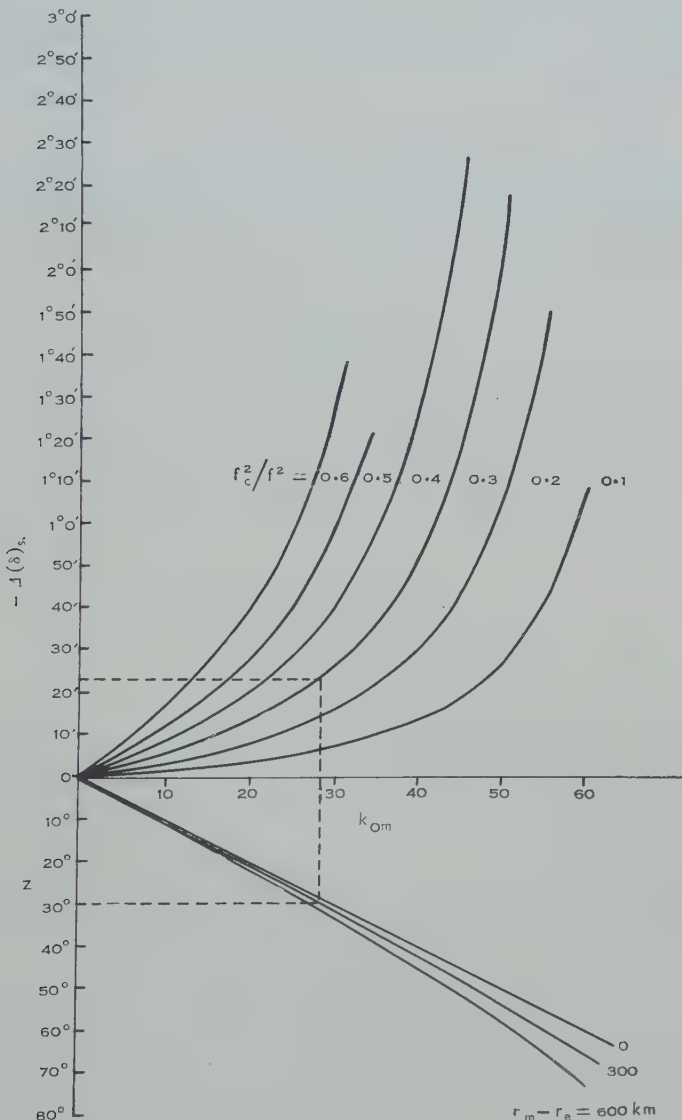


Fig. 5.—Curves showing the relationship between $\Delta(\delta)_s$ and observed zenith angle Z for various values of the parameters f_c^2/f^2 and $r_m - r_e$, according to equations (29) and (15). The dotted line illustrates the way in which the figure is used to determine $\Delta(\delta)_s$. In the example shown in which the figure is used to determine $\Delta(\delta)_s$. In the example shown

$$Z = 30^\circ, r_m - r_e = 300 \text{ km}, f_c^2/f^2 = 0.3, \text{ and } \Delta(\delta)_s = -23'.$$

ment is in the direction in which f_c increases. By contrast, in a spherically symmetrical medium the displacement is always towards the zenith.

Finally, certain restrictions have been imposed on the magnitude of the horizontal gradients. From inequality (20) and equation (22), it follows that the first term in (32) (the wedge component) should not exceed about 1/30 radian or 2°. In the next section the magnitude of the change in Right Ascension is expressed in terms of east-west gradients. Provided this change also does not exceed a few degrees, the foregoing derivation, which has neglected east-west gradients, is still valid.

V. THE APPARENT CHANGE OF RIGHT ASCENSION

In general the refractive index gradient has an east-west component. We will designate the resulting change in Right Ascension by $\Delta(\alpha)$. From equation (2), by an argument similar to that outlined in Section IV (b),

$$\Delta(\alpha) = \frac{d \cdot \bar{w}(\sigma) \sec \delta \cdot \sec \varphi_a \sec k_{0m}}{2(r_b + 3d/2)f^2} \cdot \frac{\partial(f_c^2)}{\partial L}. \quad \dots \dots \quad (34)$$

The angle φ_a is the latitude of the point at which the ray intersects the upper ionospheric boundary. To sufficient accuracy $\sec \varphi_a$ is given by

$$\sec \varphi_a = \sec \Phi \left[1 - \tan k_{0m} \tan \varphi_T \left(\frac{r_b - r_e + 3d/2}{r_m} \right) \right]^{-1}.$$

Provided

$$\frac{\cos \delta}{\cos \Phi} \cos k_{0m} \approx 1,$$

(34) has an accuracy of about 5 per cent.

VI. APPLICATIONS OF THE THEORY

The results just derived have been applied to a number of discrete source observations taken with the Sydney 19.7 Mc/s Mills Cross with a beamwidth of 1.4° (Shain 1958).

The observing site (lat. 34° S., long. 151° E.) is well placed for calculating f_c^2 and its north-south gradient, since there are a number of ionospheric sounding stations 800–900 km apart and close to the 150th meridian. The situation is less favourable, however, for calculating the east-west gradient. The nearest stations in this direction are at Christchurch (New Zealand) and Watheroo (Western Australia), each more than 2000 km away. Furthermore, it was found on comparing sounding records taken in longitude 150° E. with Watheroo records for the same local times, that the time derivative of f_c^2 (as used by Smith (1952)), was not a sufficiently accurate measure of the east-west gradient. The method of computation finally arrived at required data from at least three stations. Since there were very few days on which these were all available at the appropriate times, much of the information had to be based on monthly medians. Consequently, the east-west component estimates are considerably less accurate than those of the north-south component.

Figure 6 shows declination measurements of the source 03S3A, taken between September and November 1957. The local times of transit were between 2330 and 0330. It is clear that there is good correlation between observed declination δ_0 and the quantity $R(\delta)$, given by equations (32) and (33). (Since the source is close to the zenith the second term on the right-hand side of (32) may be neglected.) From the "least squares" regression line also shown on this figure, the "true declination" is $-37^\circ 23'$. The declination measured at 85 Mc/s is $-37^\circ 23' \pm 3'$ (Sheridan 1958), so that the two results agree within the limits of observational accuracy.

From the slope of the regression line, taking r_b as 6500 km, we calculate that $d=355$ km. This is only about 10 per cent. lower than a value derived by combining Evans's (1957) moon-echo results taken in the pre-dawn period at

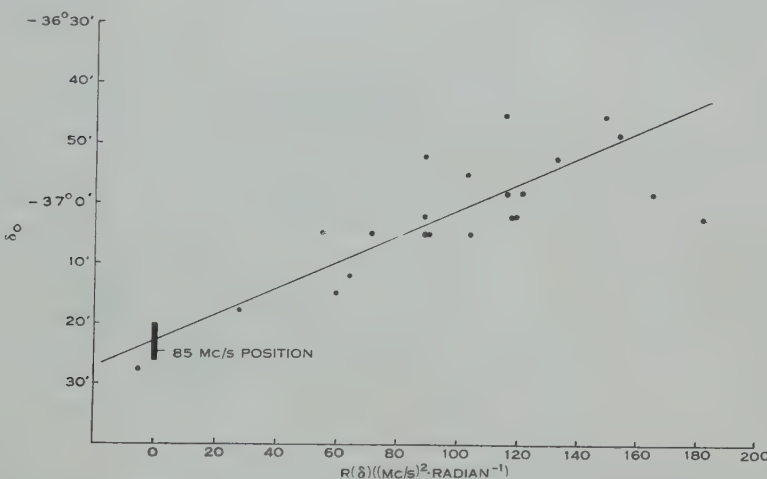


Fig. 6.—Observed declination (epoch 1950) of the source 03S3A related to ionospheric parameters according to equation (32). $R(\delta)=\bar{w}(\sigma)\partial f_e^2/\partial\phi$.

Manchester with simultaneous critical frequency measurements made at Slough. In an earlier report on this work Komesaroff and Shain (1959) quoted a value of 550 km. The lower value is based on a more careful analysis of the experimental results.

The derived value of d was used to compute Right Ascension corrections for the same observations, and Figure 7 (a) shows the observed and corrected positions of 03S3A. The improvement in declination is very marked; that in Right Ascension is by no means as good, although the mean error in Right Ascension has been reduced from $0^m.4$ to less than $0^m.1$.

Figure 7 (b) is a similar diagram for the source 09S1A based on observations taken between the beginning of October and mid December 1957. During this period the source was observed within two and a half hours of sunrise when ionospheric conditions were changing rapidly, making the period difficult for refraction corrections. Nevertheless, although the corrected declinations show

considerable "scatter", their mean is within 5' of the 85 Mc/s position (Mills, Slee, and Hill 1958). On the other hand, there is still a systematic displacement in Right Ascension from the high frequency position. In the absence of more detailed ionospheric data, it is not possible to assess the significance of this shift.

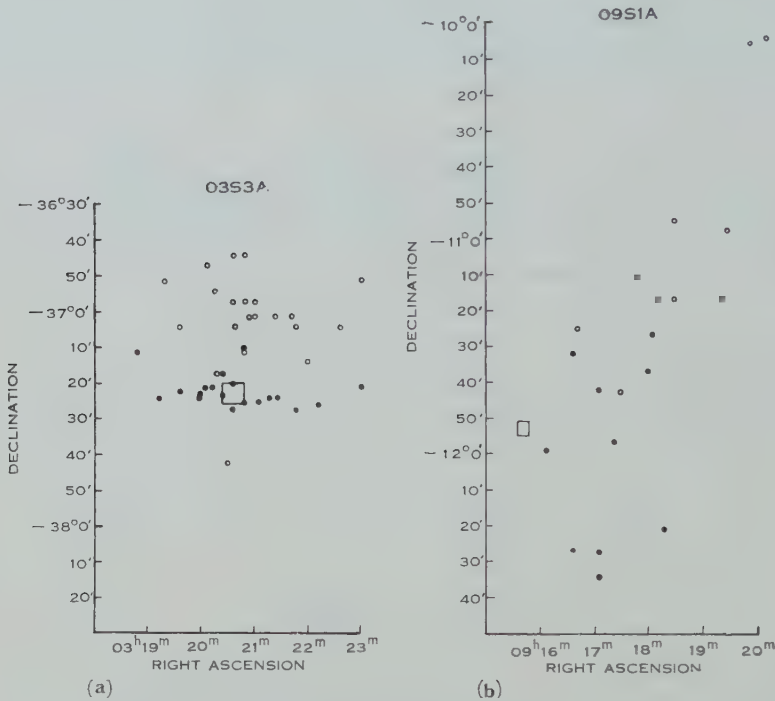


Fig. 7.—19.7 Mc/s positions (epoch 1950) of two sources : (a) 03S3A, (b) 09S1A. Observed positions are shown by open circles and positions obtained after applying corrections for ionospheric refraction are shown by full circles. The rectangles indicate 85 Mc/s positions.

VII. CONCLUSIONS

The main results of the present paper are expressed by equations (32) and (34), relating the displacement components of a radio source at transit to ionospheric parameters. In order to compute these displacements under commonly prevailing ionospheric conditions, account must be taken, not only of the total electron content of a vertical column through the ionosphere but also of the horizontal gradients of this quantity.

Application of the results to preliminary observations, taken mainly in the early morning, indicates that over several months the effective ionospheric thickness d was apparently constant at a value of about 355 km, in substantial agreement with the results of Evans (1957) for another time and place.

Combining this value of d with sounding data on the basis of equations (32) and (34), a considerable improvement in measured source positions has been effected. Even under the somewhat unfavourable conditions around sunrise time, it has been possible to achieve a ten to one reduction in mean declination

error. To make the declination correction it was necessary to derive detailed information relating to north-south gradients from the published data of several sounding stations along the eastern Australian coast. No such detailed information about east-west gradients is available, however, and the improvement in Right Ascension which could be achieved was correspondingly less marked.

Since these observations were made, many more position measurements have been taken, and these, together with a more detailed account of the experimental procedure, will be given in a subsequent paper.

VIII. ACKNOWLEDGMENTS

The author is indebted to Mr. C. A. Shain, who suggested this investigation and provided much guidance in carrying it out. He also wishes to thank Dr. J. H. Piddington and Dr. R. F. Mullaly for their helpful criticism of the presentation.

IX. REFERENCES

- BAILEY, D. K. (1948).—*Terr. Magn. Atmos. Elect.* **53**: 41.
BELYAEV, N. A. (1955).—*Astr. J., Moscow* **32**: 357.
CHVOJKOVA, E. (1958a).—*Bull. Astr. Insts. Csl.* **9**: 1.
CHVOJKOVA, E. (1958b).—*Bull. Astr. Insts. Csl.* **9**: 133.
EVANS, J. V. (1957).—*J. Atmos. Terr. Phys.* **11**: 259.
KOMESAROFF, M. M., and SHAIN, C. A. (1959).—*Nature* **183**: 1584.
LINK, F. (1957).—*Bull. Astr. Insts. Csl.* **8**: 112.
MILLS, B. Y., SLEE, O. B., and HILL, E. R. (1958).—*Aust. J. Phys.* **11**: 360.
RATCLIFFE, J. A. (1951).—*J. Geophys. Res.* **56**: 487.
SHAIN, C. A. (1958).—*Proc. Inst. Radio Engrs., N.Y.* **46**: 85.
SHERIDAN, K. V. (1958).—*Aust. J. Phys.* **11**: 400.
SMITH, F. G. (1952).—*J. Atmos. Terr. Phys.* **2**: 350.

HYPERFINE STRUCTURE IN THE MICROWAVE SPECTRUM OF WATER

II. EFFECTS OF MAGNETIC INTERACTIONS

By D. W. POSENER*

[*Manuscript received March 10, 1960*]

Summary

Further analysis of the hyperfine structure appearing in the observed microwave spectra of HDO and D₂O, taking into account nuclear quadrupole and magnetic dipole interactions, leads to a complete determination of the electric field gradient tensor at the hydrogen nuclei in the water molecule, giving a value along the bond direction of $(+1.59 \pm 0.04) \times 10^{16}$ e.s.u.

Parameters describing magnetic effects in the observed spectra have also been obtained.

I. INTRODUCTION

The partially resolved microwave spectra of the 2₂₀←2₂₁ transition of HDO at 10,278 Mc/s and of the 3₁₃←2₂₀ line of D₂O at 10,919 Mc/s have been previously described (Posener 1957, hereafter referred to as I) and the results for D₂O analysed on the assumption that only nuclear quadrupole coupling effects contributed significantly to the observed hyperfine structure. It was there concluded that the quadrupole coupling constant of the deuteron in the direction of the OD bond was $\langle eqQ \rangle_{OD} = +353 \pm 4$ kc/s, and that it was not possible to account for the HDO spectrum if only the nuclear quadrupolar interaction were taken into account.

Improved agreement between calculated and observed spectra has now been obtained by including effects due to magnetic interactions occurring within the molecules; it will be shown that neglect of these effects in the previous analysis of D₂O introduced a systematic error of some 10 per cent. in the estimation of $\langle eqQ \rangle_{OD}$.

II. THEORY

(a) Calculation of Transition Frequencies

Hypersfine structure in the rotational spectra of HDO and D₂O arises from interaction of the magnetic dipole and nuclear quadrupole moments of the hydrogen and deuterium nuclei with the various electric and magnetic fields occurring in the rotating molecules. The generalized theory of such interactions has been published (Posener 1958, hereafter referred to as II), and our notation will follow this work unless otherwise stated.

* Division of Electrotechnology, C.S.I.R.O., University Grounds, Chippendale, N.S.W.

TABLE I
ENERGY MATRIX FOR HDO, $J=2$

| F_1, F | 1,1/2 | 1,3/2 | 2,3/2 | 2,5/2 | 3,5/2 | 3,7/2 |
|----------|--|---|--|--|--|--|
| 1,1/2 | $\frac{1}{6}(\alpha(Q) + \alpha(S))$ $+\frac{1}{2}(c(D) + \frac{1}{2}c(H))$ | | | | | |
| 1,3/2 | | $\frac{1}{6}\left(\alpha(Q) - \frac{1}{2}\alpha(S)\right)$ $+\frac{1}{2}\left(c(D) - \frac{1}{4}c(H)\right)$ | $\frac{1}{8}c(H)$ | | | |
| 2,3/2 | | | $-\frac{1}{6}\left(\alpha(Q) - \frac{1}{2}\alpha(S)\right)$ $+\frac{1}{6}\left(c(D) + \frac{5}{4}c(H)\right)$ | | | |
| 2,5/2 | | | | $-\frac{1}{6}\left(\alpha(Q) + \frac{1}{3}\alpha(S)\right)$ $+\frac{1}{6}\left(c(D) - \frac{5}{6}c(H)\right)$ | $-\frac{14}{36}\left(\frac{5}{7}\alpha(S) - c(H)\right)$ | |
| 3,5/2 | | | | | $\frac{1}{21}\left(\alpha(Q) - \frac{4}{3}\alpha(S)\right)$ $-\frac{1}{3}\left(c(D) - \frac{2}{3}c(H)\right)$ | |
| 3,7/2 | | | | | | $\frac{1}{21}(\alpha(Q) + \alpha(S))$ $-\frac{1}{3}\left(c(D) + \frac{1}{2}c(H)\right)$ |

TABLE 2
ENERGY MATRIX FOR D₂O, J=2

| <i>I,F'</i> | 2,0 | 2,1 | 0,2 | 2,2 | 2,3 | 2,4 |
|-------------|--|-----|---|--|--|---|
| 2,0 | $\frac{1}{3}(\alpha(Q) + \alpha(S)) + c(D)$ | | | | | |
| 2,1 | $\frac{1}{6}(\alpha(Q) + \alpha(S)) + \frac{5}{6}c(D)$ | | | | | |
| 0,2 | | 0 | $\frac{1}{63\frac{1}{2}}(2\alpha(Q) - \alpha(S))$ | | | |
| 2,2 | | | $\frac{1}{63\frac{1}{2}}(2\alpha(Q) - \alpha(S))$ | $-\frac{1}{14}(\alpha(Q) + \alpha(S)) + \frac{1}{2}c(D)$ | | |
| 2,3 | | | | | $-\frac{4}{21}(\alpha(Q) + \alpha(S))$ | |
| 2,4 | | | | | | $\frac{2}{21}(\alpha(Q) + \alpha(S)) - \frac{2}{3}c(D)$ |

TABLE 3
ENERGY MATRIX FOR D₂O, J=3

| I,F | 2,1 | 2,2 | 0,3 | 2,3 | 2,4 | 2,5 |
|-----|---|---|-----|---|--|---|
| 2,1 | $\frac{2}{15}(\alpha(Q) + \alpha(S)) + \frac{2}{3}c(D)$ | | | | | |
| 2,2 | | $\frac{1}{30}(\alpha(Q) + \alpha(S)) + \frac{1}{2}c(D)$ | | | | |
| 0,3 | | | 0 | $\frac{1}{270}\langle 2\alpha(Q) - \alpha(S) \rangle$ | | |
| 2,3 | | | | $\frac{1}{270}\langle 2\alpha(Q) - \alpha(S) \rangle$ | $-\frac{11}{180}\langle \alpha(Q) + \alpha(S) \rangle + \frac{1}{4}c(D)$ | |
| 2,4 | | | | | $-\frac{1}{12}\langle \alpha(Q) + \alpha(S) \rangle - \frac{1}{12}c(D)$ | |
| 2,5 | | | | | | $\frac{1}{18}\langle \alpha(Q) + \alpha(S) \rangle - \frac{1}{2}c(D)$ |

Choosing for HDO the $I_1JF_1I_2FK$ representation, in which \mathbf{I}_1 is the spin of the deuterium nucleus ($I_1=1$) and \mathbf{I}_2 the spin of the nucleus of hydrogen ($I_2=\frac{1}{2}$), the matrix elements of the hyperfine structure part of the Hamiltonian may be obtained directly from II, equation (58), noting that $\alpha_{J,\tau}^{(2)}=0$, since the hydrogen nucleus has no quadrupole moment. For conciseness we will replace $\alpha_{J,\tau}^{(1)}$, $\alpha_{J,\tau}^{(S)}$, $c_{J,\tau}^{(1)}$, and $c_{J,\tau}^{(2)}$ by $\alpha^{(Q)}$, $\alpha^{(S)}$, $c^{(D)}$, and $c^{(H)}$ respectively, with the rotational state energy dependence implied if not indicated by subscripts. Also, we use the $J_{K_a K_c}$ subscript notation for rotational states rather than J_τ . Then, with $J=2$, the hyperfine structure energy matrix for HDO becomes as shown in Table 1, to the approximations discussed in II.

More appropriate for D₂O is the I_2I_1IJFK representation, in which \mathbf{I}_1 and \mathbf{I}_2 are the spins of the two deuterium nuclei ($I_1=I_2=1$). Allowing for the molecular symmetry the matrix elements for $J=2$ and $J=3$, as given by II, equation (53), are as shown in Tables 2 and 3.

The magnetic dipole-dipole interaction terms $\alpha^{(S)}$ occurring in the energy matrices may be computed as constants from II, equation (54), using equilibrium internuclear distances for sufficient accuracy since the zero-point vibrations will not significantly affect the results. We have used (Herzberg 1945, p. 489): $r_e=0.9584 \times 10^{-8}$ cm, and $\angle \text{HOH}=104^\circ 27'$. With the $\langle J_g^2 \rangle$'s calculated from rotational constants given elsewhere (Posener 1953), the dipole-dipole terms become as shown in Table 4.*

TABLE 4
MAGNETIC DIPOLE-DIPOLE INTERACTION CONSTANTS

| HDO | D ₂ O |
|--|---|
| $\alpha_{2_{20}}^{(S)} -25.8 \text{ kc/s}$ | $\alpha_{3_{10}}^{(S)} 7.3 \text{ kc/s}$ |
| $\alpha_{2_{21}}^{(S)} -25.6 \text{ kc/s}$ | $\alpha_{2_{20}}^{(S)} -4.8 \text{ kc/s}$ |

When a diagonalizing transformation \mathbf{R} is applied to these matrices \mathbf{H} , the resulting diagonal matrices $\tilde{\mathbf{R}}\mathbf{H}\mathbf{R}$ give the energy splittings of the rotational levels, and thus the frequency shifts from the "unperturbed" line centres v_0 can be obtained. (The tilde denotes the matrix transpose. In the sequel an unprimed matrix will refer to the lower rotational state, a primed matrix to the upper state.)

Although the hyperfine interactions result in considerable mixing of the "unperturbed" states, so that F_1 (in HDO) and I (in D₂O) are no longer good quantum numbers, it is convenient to retain them as labels for a description of the actual energy levels.

* In II, p. 2, it was incorrectly stated that nuclei have magnetic moments $g_k \mu_N$; this should read $g_k \mu_N I_k$. Because of this error the nuclear g-factor for hydrogen was taken as half its correct value of $g_H = +5.585340$ and the calculations on HDO were actually carried through with values of $\alpha^{(S)}$ half those shown in Table 4. As discussed below (Section IV (c)) it is not now considered that a recalculation is warranted.

(b) Calculation of Relative Intensities

The intensity of a transition $a' \leftarrow a$ is proportional to $|(a | \mu | a')|^2$, where $(a | \mu | a')$ is the dipole moment matrix; the total intensity A of a line is the sum of its components, which in the present case arise only from the degeneracy in M_F . If μ stands for the dipole moment matrix in a representation in which the energy is not diagonal, then in the notation of the previous section

$$(a | \mu | a') = \tilde{R} \mu R', \quad \dots \dots \dots \quad (1)$$

and so

$$A = \sum_{M_F M'_F} |\tilde{R} \mu R'|^2. \quad \dots \dots \dots \quad (2)$$

For the hyperfine structure in HDO and D₂O, in the non-diagonal representations $I_1 J F_1 I_2 F K$ and $I_2 I_1 I J F K$ respectively, we can use II, equation (12), to factor out the dependence on F_1 and F (or I and F) because the dipole moment and the nuclear spin operators commute. Then, omitting irrelevant quantum numbers, we get for the elements of μ ,

$$\begin{aligned} \mu(\text{HDO}) &= (J K M_F : \mu : J' K' M'_F) (J F_1 | J' F'_1) (F_1 F | F'_1 F'), \\ \mu(\text{D}_2\text{O}) &= (J K M_F : \mu : J' K' M'_F) (I J F | I J' F'). \end{aligned} \quad \dots \dots \dots \quad (3)$$

The transformation indicated in (1) is diagonal in F and M_F , so its application to the expressions in (3) does not affect the first factors on the right of these equations. If the now transformed dipole moment matrix is put into (2) and the summation over M_F , M'_F , and the polarizations is carried out (Condon and Shortly 1953, equation 745), and if we then omit factors irrelevant to the hyperfine structure problem, the result can be written as

$$\begin{aligned} A(\text{HDO}) &= |\tilde{R} B(\text{HDO}) R'|^2, \\ A(\text{D}_2\text{O}) &= |\tilde{R} B(\text{D}_2\text{O}) R'|^2, \end{aligned} \quad \dots \dots \dots \quad (4)$$

where

$$\begin{aligned} B(\text{HDO}) &= [(2F+1)\Xi(F, F')]^{\frac{1}{2}} (J F_1 | J' F'_1) (F_1 F | F'_1 F'), \\ B(\text{D}_2\text{O}) &= [(2F+1)\Xi(F, F')]^{\frac{1}{2}} (I J F | I J' F'). \end{aligned} \quad \dots \dots \dots \quad (5)$$

The matrix elements $B(\text{HDO})$ and $B(\text{D}_2\text{O})$ are shown in Tables 5 and 6 respectively.

III. ANALYSIS OF THE OBSERVATIONS

The preceding theory shows that it is possible to calculate the hyperfine structure frequencies and relative intensities for the two molecules in terms of the fairly small number of variables appearing in the Hamiltonian. However, because of the small magnitude of the interactions involved, the observed transitions lie close together and the experimental technique could not completely separate them. As shown in I, only a general profile of the intensity as a function of frequency was measured, with occasionally a prominent peak more completely resolved. Nevertheless, a considerable amount of information is contained in such measurements, so the problem became one of calculating line profiles and

adjusting the variables until adequate agreement with experiment was obtained. Most of the large amount of numerical work required to do this was carried out with the aid of the digital computer SILLIAC* in about 30 hours of computing; about two-thirds of this time was, however, employed on program development and exploratory calculations.

TABLE 5
THE MATRIX $B(\text{HDO})$ FOR $J=2 \leftarrow 2$

| | | 2_{20} | | | | | |
|------------|-------|--------------------|-------------------------|--------------------------|-------------------------|--------------------------|--------------------------|
| | | 1,1/2 | 1,3/2 | 2,3/2 | 2,5/2 | 3,5/2 | 3,7/2 |
| F'_1, F' | | | | | | | |
| 2_{21} | 1,1/2 | $6^{\frac{1}{2}}$ | $-3^{\frac{1}{2}}$ | $-3^{\frac{1}{2}}$ | | | |
| | 1,3/2 | $-3^{\frac{1}{2}}$ | $15^{\frac{1}{2}}$ | $-(3/5)^{\frac{1}{2}}$ | $-(27/5)^{\frac{1}{2}}$ | | |
| | 2,3/2 | $-3^{\frac{1}{2}}$ | $-(3/5)^{\frac{1}{2}}$ | $15^{\frac{1}{2}}$ | $-(5/3)^{\frac{1}{2}}$ | $-(56/15)^{\frac{1}{2}}$ | |
| | 2,5/2 | | $-(27/5)^{\frac{1}{2}}$ | $-(5/3)^{\frac{1}{2}}$ | $(70/3)^{\frac{1}{2}}$ | $-2/15^{\frac{1}{2}}$ | $-4/3^{\frac{1}{2}}$ |
| | 3,5/2 | | | $-(56/15)^{\frac{1}{2}}$ | $-2/15^{\frac{1}{2}}$ | $(640/21)^{\frac{1}{2}}$ | $-(32/21)^{\frac{1}{2}}$ |
| | 3,7/2 | | | | $-4/3^{\frac{1}{2}}$ | $-(32/21)^{\frac{1}{2}}$ | $(288/7)^{\frac{1}{2}}$ |

TABLE 6
THE MATRIX $B(\text{D}_2\text{O})$ FOR $J=3 \leftarrow 2$

| | | 3_{13} | | | | |
|----------|-----|--------------------|--------------------|---------------------|------------------------|------------------------|
| | | 2,1 | 2,2 | 0,3 | 2,3 | 2,4 |
| I', F' | | | | | | |
| 2_{20} | 2,0 | $21^{\frac{1}{2}}$ | | | | |
| | 2,1 | $21^{\frac{1}{2}}$ | $42^{\frac{1}{2}}$ | | | |
| | 0,2 | | | $105^{\frac{1}{2}}$ | | |
| | 2,2 | $-3^{\frac{1}{2}}$ | $30^{\frac{1}{2}}$ | | $72^{\frac{1}{2}}$ | |
| | 2,3 | | $-3^{\frac{1}{2}}$ | | $(63/2)^{\frac{1}{2}}$ | $15/2^{\frac{1}{2}}$ |
| | 2,4 | | | | $-(3/2)^{\frac{1}{2}}$ | $(45/2)^{\frac{1}{2}}$ |

* Adolph Basser Computing Laboratory, University of Sydney.

At first a Lorentz profile was used to calculate the amount each transition contributed to the intensity profile at a given frequency; however, the Doppler contribution to the broadening was of like magnitude, and later calculations took this into account with subsequent improvement in the agreement between calculated and observed profiles. A numerical integration method was used for computation of this combined effect (Posener 1959).

It was initially hoped that the whole problem could be solved automatically on the computer; a program was written to calculate the line profiles for a given set of initial variables, and a "steepest descent" method used to minimize the sum of squares of residuals between observed and calculated ordinates. As an initial approximation, values corresponding to the results of I were used, i.e. $(eqQ)_{OD} = 353$ kc/s and all the $c^{(k)}$ taken as zero. Although it was possible to decrease the sum of squares, the results did not significantly improve agreement with the observed line profiles because the initial approximation was poor and the calculation became trapped in various shallow minima which abound in the multidimensional surface. Similar difficulties arose when other initial approximations were used.

It became clear that, because of the relatively poor initial approximation, the minimization of the sum of squares of the residuals was alone not a sufficiently powerful criterion for automatic solution of the problem. This was then broken into parts, an approach which proved successful. Firstly, a set of $\alpha^{(Q)}$ and $c^{(k)}$ was obtained to fit the HDO profile; secondly, a similar set was found for D₂O; finally, these were combined.

In order to fit the HDO spectrum alone, $\alpha^{(Q)} = 434$ kc/s, corresponding to $(eqQ)_{OD} = 353$ kc/s, was taken as approximately correct, and trial profiles computed for $c^{(D)} = -500(50) + 500$ kc/s, $c^{(H)} = -1000(50) + 1000$ kc/s, a range which ought to cover all reasonably expected values of these parameters. At this stage no distinction was made between parameter values for the upper and lower states, for which the difference should be quite small. It was found that general agreement with the observed profile occurred only in one very restricted area of this net, and by examining this region with smaller mesh sizes a good fit was obtained for $c^{(D)} \sim +10$ kc/s, $c^{(H)} \sim +240$ kc/s.

At this point empirical refinements, such as adjustment of the line "centre" v_0 and of the line-width parameters Δv_L (Lorentz half half-width) and Δv_D (Doppler half half-width) were carried out; subsequently it was found that use of the Doppler-Lorentz profile did not significantly affect the fit in so far as the frequencies of transitions were concerned, although the overall agreement was much better. For Δv_D the value 12.0 kc/s (calculated for the experimental conditions) gave satisfactory results, and trial variations of several kc/s in this value (keeping the total line width constant) did not appear to change the results significantly.

Having now obtained something which looked like the observed profile, i.e. a good initial approximation, more refined techniques could be applied. By examining the individual transitions and, where desirable, shifting them one at a time independently so as to synthesize a profile agreeing somewhat better with the measured one, it became possible to "estimate" the frequencies of the

unresolved transitions with some accuracy. Following this, the effects of small changes in the parameters $\alpha^{(Q)}$ and $c^{(k)}$ on the frequencies of these transitions gave a set of linear equations to which a least squares fit could be made in order to further improve the parameters. The whole process was repeated as necessary until significant improvement ceased to be obtained.

TABLE 7
HDO $2_{20} \leftarrow 2_{21}$ HYPERFINE TRANSITION FREQUENCIES AND RELATIVE INTENSITIES*

| | | 2_{20} | | | | | |
|----------|-------|----------------|----------------|----------------|---------------|----------------|----------------|
| | | 1,1/2 | 1,3/2 | 2,3/2 | 2,5/2 | 3,5/2 | 3,7/2 |
| | | F'_1, F' | F_1, F | | | | |
| 2_{21} | 1,1/2 | — | 172 ± 2 | — | | | |
| | | 244·4 | 168·3 | 76·9 | | | |
| | | 14·58 | 12·17 | 2·42 | | | |
| | 1,3/2 | 320 ± 2 | — | — | 80 ± 1 | — | |
| | | 322·3 | 246·2 | 154·8 | 80·3 | 265·1 | |
| | | 12·48 | 27·05 | 0·48 | 15·27 | 3·04 | |
| | 2,3/2 | — | — | — | — | 354 ± 2 | |
| | | 409·9 | 333·8 | 242·4 | 167·9 | 352·6 | |
| | | 2·10 | 1·11 | 47·19 | 0·00 | 7·93 | |
| | 2,5/2 | 411 ± 1 | — | — | — | — | 331 ± 2 |
| | | 410·2 | 318·8 | 244·3 | 429·0 | 329·7 | |
| | | 15·20 | 0·03 | 60·63 | 0·91 | 10·74 | |
| | 3,5/2 | — | 135 ± 2 | — | — | — | 144 ± 2 |
| | | 225·6 | 134·2 | 59·7 | 244·5 | 145·2 | |
| | | 2·80 | 8·23 | 0·81 | 69·74 | 5·93 | |
| | 3,7/2 | — | 165 ± 2 | 350 ± 2 | — | | |
| | | — | 163·2 | 348·0 | 248·6 | | |
| | | — | 10·79 | 5·88 | 100·00 | | |

* The first line of each row shows the estimated frequency (bold type) and the second line shows the frequency calculated from the best HDO parameters (column (a) of Table 9). All frequencies are in kc/s above 10,278·000 Mc/s. The last line of each row gives the relative intensities (italics).

Estimated (using this word in the sense described above) transition frequencies for HDO are shown in Table 7,* together with the frequencies calculated from the best parameters (listed in Table 9). The corresponding profiles are shown in Figure 1, and, to a larger scale, in Figure 2. The latter may be compared with the spectrogram of Figure 3, which shows the corresponding part of the HDO spectrum at higher gain and was obtained at the same time as the experimental results reported in I.

* All error limits quoted for the present work are r.m.s. errors.

In the case of D₂O, the initial approximation of pure quadrupolar coupling already gave a good fit with the positions of the major transitions approximately known (see I), and again corresponding to $(eqQ)_{OD} = 353$ kc/s there results $\alpha_{3_{15}}^{(Q)} = -661$ kc/s and $\alpha_{2_{20}}^{(Q)} = 263$ kc/s. Since the $c^{(D)}$ were expected to be quite small, a least squares fit was made directly to the estimated transition frequencies in a manner similar to that used for HDO, and subsequently improved as far as possible.

Frequencies and parameters resulting from this analysis of D₂O are shown in Tables 8 and 9, with the profiles drawn in Figure 4.

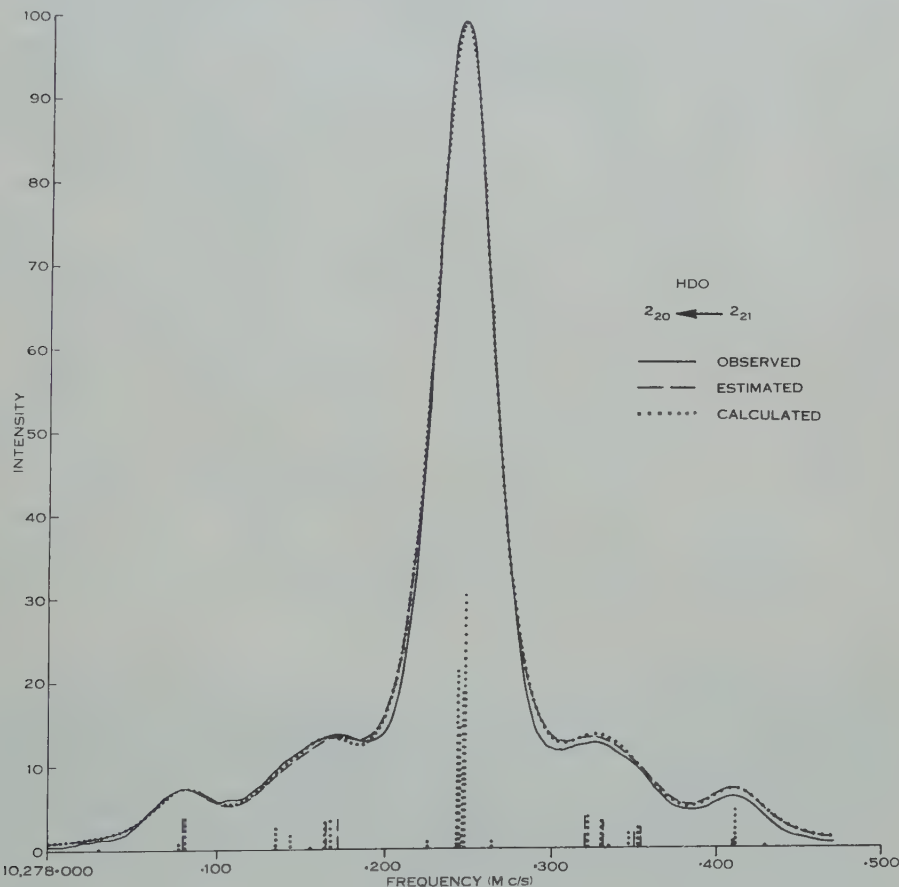


Fig. 1.—Line profiles in the $2_{20} \leftarrow 2_{21}$ transition of HDO. The "estimated" profile was computed using the "estimated" frequencies of Table 7, while the "calculated" profile was obtained using the frequencies computed from final values of the parameters (column (a) of Table 9).

IV. RESULTS AND DISCUSSION

The major difficulty in the present analysis was to account for the unresolved structure in the HDO spectrum in the region of ± 90 kc/s from the line centre; it can perhaps be regarded as fortunate that agreement could be obtained only for one specific set of values of $c^{(D)}$ and $c^{(H)}$ out of the initial set of 861 trial values.

The magnitude of $e^{(H)}$ (~ 240 kc/s) gives rise to frequency shifts of up to 100 kc/s (Fig. 5), which is in the order of that observed in formaldehyde (Okaya 1956). Thus it is apparent that in any molecule in which some or all of the hyperfine

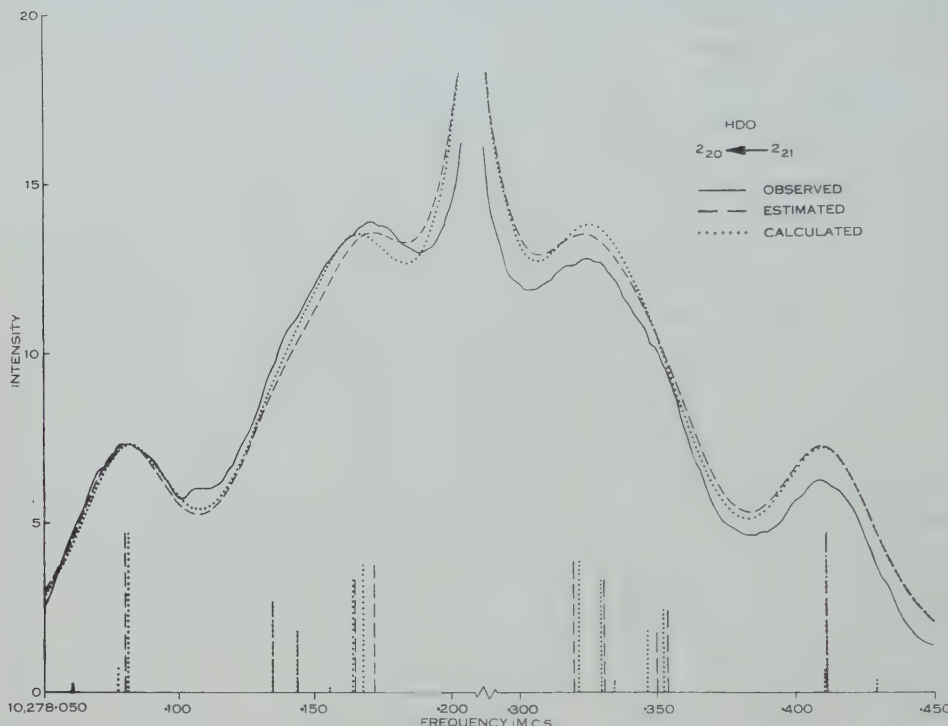


Fig. 2.—Line profiles in the $2_{20} \leftarrow 2_{21}$ transition of HDO. This diagram shows part of Figure 1 with a magnified intensity scale.

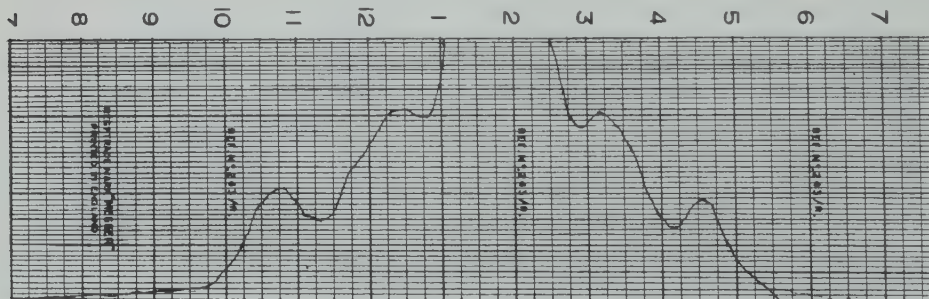


Fig. 3.—High-gain spectrogram of part of the HDO $2_{20} \leftarrow 2_{21}$ transition.

structure is due to both deuterium and hydrogen, both will contribute about equally.

For D₂O the magnetic frequency shifts are much smaller (Fig. 6), and no difficulty was experienced in fitting the spectrum.

The agreement of the final calculated frequencies with the estimated ones to within a few kc/s appears satisfactory. In fact, this agreement is rather better than might have been expected from consideration of the unresolved observations.

TABLE 8
 $D_2O\ 3_{13} \leftarrow 2_{20}$ HYPERFINE TRANSITION FREQUENCIES AND RELATIVE INTENSITIES*

| | | 3_{13} | | | | | |
|----------|-----|--------------|--------------|--------------|--------------|-----|-----|
| | | 2,1 | 2,2 | 0,3 | 2,3 | 2,4 | 2,5 |
| I, F | | | | | | | |
| | | | | | | | |
| | 2,0 | 258±2 | | | | | |
| | | 257.7 | | | | | |
| | | 12.73 | | | | | |
| | | — | — | | | | |
| | 2,1 | 303.9 | 362.1 | | | | |
| | | 12.73 | 25.45 | | | | |
| | | — | — | 300±1 | | | |
| | 0,2 | 300.9 | 359.2 | 300.6 | 469.6 | | |
| | | 0.85 | 8.52 | 54.23 | 0.04 | | |
| 2_{20} | | — | — | — | 604±1 | | |
| | 2,2 | 434.3 | 492.6 | 433.9 | 603.0 | | |
| | | 0.97 | 9.67 | 2.38 | 50.63 | | |
| | | — | 412±2 | — | 521±1 | | |
| | 2,3 | 470.7 | 412.0 | 581.1 | 522.3 | | |
| | | 1.82 | 6.71 | 12.38 | 68.18 | | |
| | | — | — | 462±2 | 355±1 | | |
| | 2,4 | 352.0 | 521.1 | 462.2 | 354.2 | | |
| | | 0.32 | 0.59 | 13.64 | 100.00 | | |

* The first line of each row shows the estimated frequency (bold type) and the second line shows the frequency calculated from the best D_2O parameters (column (a) of Table 9). All frequencies are in kc/s above 10,919.000 Mc/s. The last line of each row gives the relative intensities (italics)

The small r.m.s. errors quoted on the variables are those obtained by applying mechanically the usual theory of random errors (see e.g. Brunt 1931). The possible effects of systematic errors are vividly illustrated in the present problem; in I for D_2O it was assumed that $c^{(D)}=0$, leading to a good least squares fit ($eqQ_{OD}=+353\pm 4$ kc/s (P.E.)). The seriousness of the neglect of $c^{(D)}$ and $\alpha^{(S)}$ is shown by the values now obtained of $(eqQ)_{OD}=+315\pm 7$ kc/s (r.m.s. error), somewhat outside the previously estimated error limits.

In view of the good fit of calculated and observed profiles it is now profitable to go on to a consideration of the results shown in Tables 8 and 9. In fact, the

relatively large computational effort involved in this analysis was undertaken in the hope that significant results of importance to molecular theory could be obtained, since the possession by nuclei of quadrupole and magnetic moments allows them to act as test probes by means of which we can in principle measure at their geometrical locations the electromagnetic effects of the molecular charge distribution.

TABLE 9
PARAMETERS

| | Best Parameters* (a) (kc/s) | Calculated Parameters† (b) (kc/s) |
|-------------------------|--------------------------------------|--|
| HDO | | |
| ν_0 | 10,278,245.5 ± 1 | |
| $\Delta\nu_0$ | 21.6 | |
| $\Delta\nu_D$ | 12.0 | |
| $\Delta\nu_L$ | 14.2 | |
| $\alpha_{2_{20}}^{(Q)}$ | 434.4 ± 10 | 428.3 |
| $\alpha_{2_{21}}^{(Q)}$ | 419.1 ± 10 | 424.1 |
| $c_{2_{20}}^{(D)}$ | 6.7 ± 3 | |
| $c_{2_{21}}^{(D)}$ | 9.0 ± 3 | |
| $c_{2_{20}}^{(H)}$ | 242.0 ± 6 | |
| $c_{2_{21}}^{(H)}$ | 252.0 ± 6 | |
| D_2O | | |
| ν_0 | 10,919,422.5 ± 0.6 | |
| $\Delta\nu_0$ | 18.2 | |
| $\Delta\nu_D$ | 12.0 | |
| $\Delta\nu_L$ | 10.0 | |
| $\alpha_{3_{12}}^{(Q)}$ | -659.5 ± 7 | -660.5 |
| $\alpha_{2_{20}}^{(Q)}$ | 261.8 ± 3 | 261.8 |
| $c_{3_{12}}^{(D)}$ | 42.0 ± 4 | |
| $c_{2_{20}}^{(D)}$ | 20.1 ± 3 | |

* The parameters in this column were obtained for each molecule separately.

† The quadrupolar parameters were calculated from the variables shown in Table 10.

(a) Interpretation of the Quadrupole Coupling Constants

The $\alpha^{(Q)}$ are defined by II, equation (54), as linear combinations of $\chi_{gg} = eQ\langle\partial^2V/\partial g^2\rangle$, where the g refer to principal inertial axes of the molecule. Because of Laplace's equation only two of the χ_{gg} are independent. Thus measurements on a single molecule do not completely define the quadrupole coupling tensor,* and it is usual to make some simplifying assumption such as

* Unless certain second-order effects are observable (Kikuchi, Hirota, and Morino 1959).

that the bond direction is a principal axis of this tensor, i.e. that the cross-product terms $\chi_{gg'}$ ($g' \neq g$) vanish. Sometimes the stronger assumption of cylindrical symmetry about the bond axis is also made (as in I) so that the spectra can be explained in terms of only one quadrupolar coupling constant, that along the bond direction.

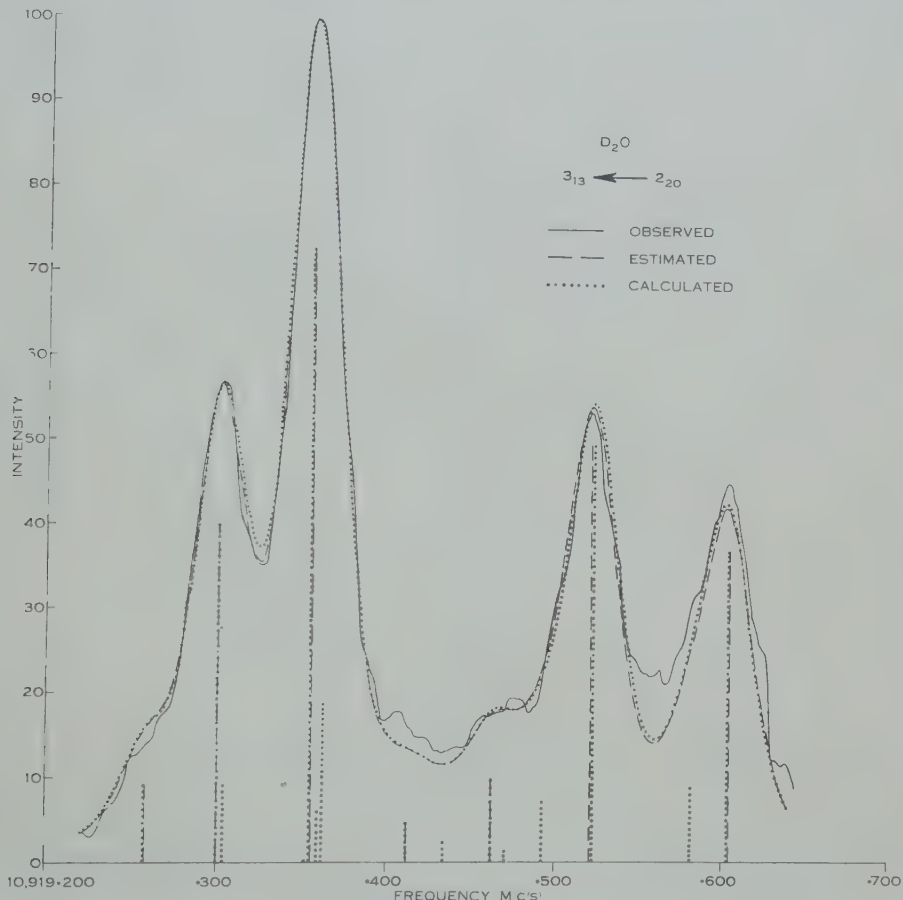


Fig. 4.—Line profiles in the $3_{13} \leftarrow 2_{20}$ transition of D_2O . The "estimated" profile was computed using the "estimated" frequencies of Table 8, while the "calculated" profile was obtained using the frequencies computed from final values of the parameters (column (a) of Table 9).

In the present problem we can obtain the χ_{gg} for two isotopic molecules whose principal inertial axes are rotated with respect to one another; the relationship between the two sets of χ_{gg} involves the usually neglected cross-product terms, and thus allows of a complete determination of the tensor. There is, of course, an approximation also involved here, the supposition that the electronic distribution in the two molecules is the same, so giving rise to the same electric field gradient at the deuterons. This is not strictly true, because of the different zero-point vibrations over which the field gradient should be averaged (Newell 1950). However, it is known that in the methyl halides for

example (Simmons and Goldstein 1952), substitution of deuterium for hydrogen changes the observed halogen quadrupole coupling constant by less than 1 per cent., while Newell (1950) has shown that the calculated difference between the electric field gradients in D_2 and in HD is similarly small. Thus it is reasonable to assume that the electric field gradients in HDO and in D_2O will be the same to within about 1 per cent.

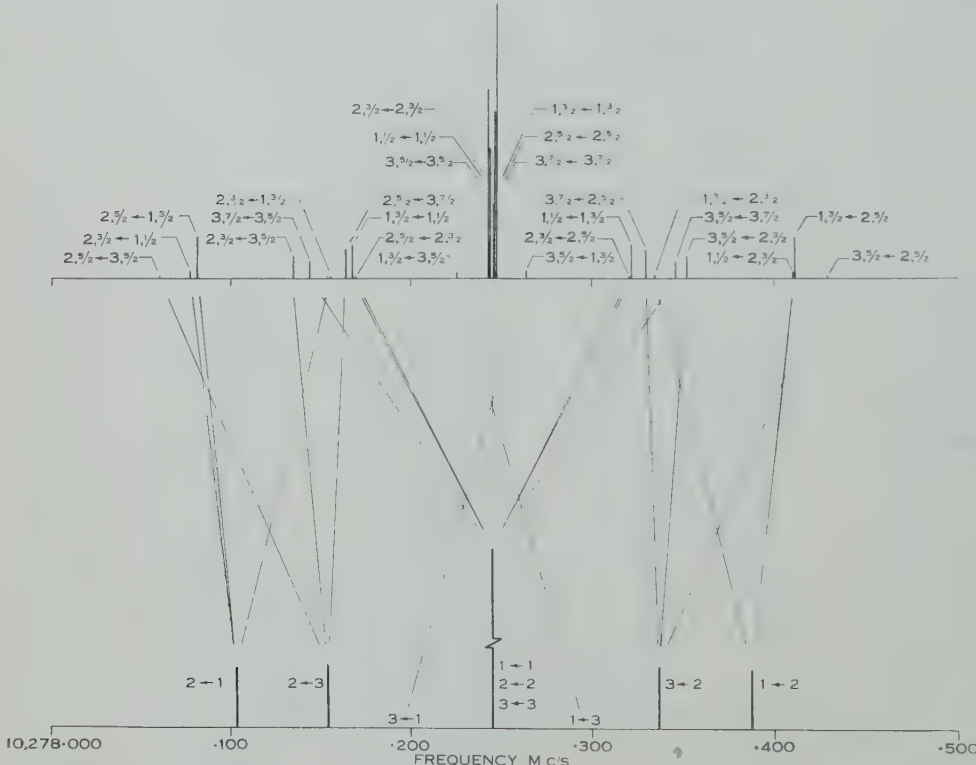


Fig. 5.—Calculated frequencies and relative intensities in the $2_{20} \leftarrow 2_{21}$ transition of HDO. The lower diagram shows the large frequency errors that occur when the magnetic effects are neglected.

If ξ , η , and ζ form a set of right-handed orthogonal axes with the ξ -direction along an OD bond and the η -direction in the molecular plane and pointing towards the bisector of the angle HOH, then, by using standard transformations together with a knowledge of the molecular geometry, we can express the four χ_{gg} (two from each molecule) in terms of three independent variables $\chi_{\xi\xi}$, $\chi_{\xi\eta}$, and $\chi_{\eta\eta}$, which completely specify the quadrupole coupling tensor ; we find

$$\begin{aligned}\alpha_{2_{20}}^{(Q)}(\text{HDO}) &= 1.4996\chi_{\xi\xi} - 0.7446\chi_{\xi\eta} + 0.3658\chi_{\eta\eta}, \\ \alpha_{2_{21}}^{(Q)}(\text{HDO}) &= 1.3769\chi_{\xi\xi} - 0.8233\chi_{\xi\eta} + 0.1231\chi_{\eta\eta}, \\ \alpha_{3_{11}}^{(Q)}(\text{D}_2\text{O}) &= -3.6007\chi_{\xi\xi} + 0.6060\chi_{\xi\eta} - 3.4446\chi_{\eta\eta}, \\ \alpha_{3_{20}}^{(Q)}(\text{D}_2\text{O}) &= 1.1746\chi_{\xi\xi} - 1.2343\chi_{\xi\eta} + 0.8566\chi_{\eta\eta}.\end{aligned}\quad \dots \quad (6)$$

Use of these equations with the $\alpha^{(Q)}$ of column (a) in Table 9 then gives the planar components of the quadrupole coupling tensor, as listed in Table 10, and these in

turn give the principal values of this tensor shown in Table 11; back-substitution in the equations (6) gives the values of the $\alpha^{(Q)}$ shown in column (b) of Table 9.

From the accepted value of the quadrupole moment of the deuteron $Q_D = (2.738 \pm 0.014) \times 10^{-27} \text{ cm}^2$ (Kolsky *et al.* 1952; Quinn *et al.* 1958), the principal values of the electric field gradient at the position of the hydrogen nuclei can be derived. Their magnitudes are also given in Table 11, where comparison is made with quantities computed theoretically by R. Bersohn (1960) from the best available estimate of the electron distribution in the water molecule (Ellison and Shull 1955).

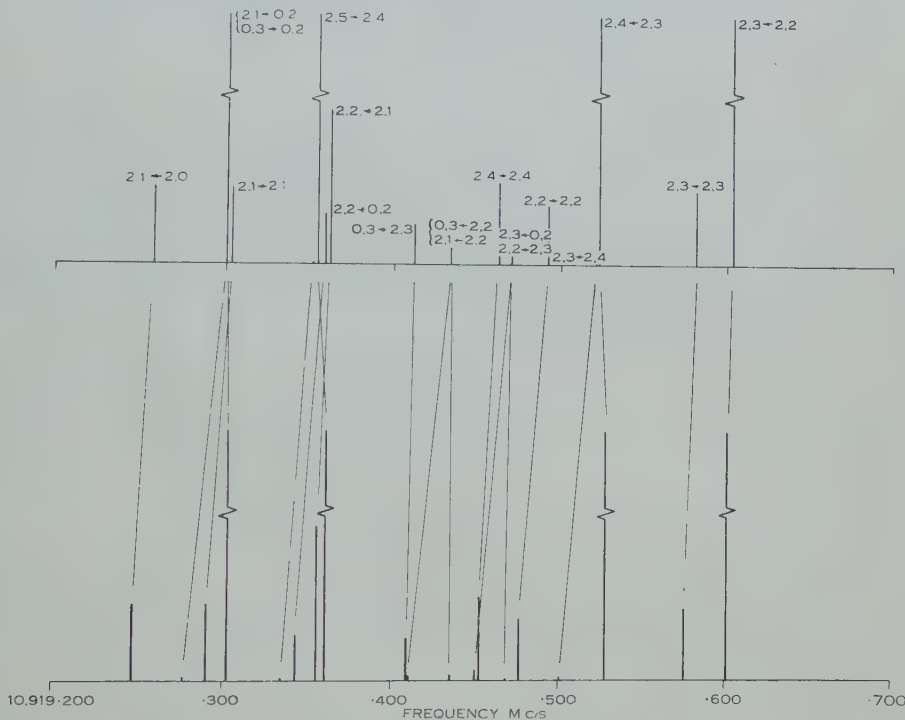


Fig. 6.—Calculated frequencies and relative intensities in the $3_{13} \leftarrow 2_{20}$ transition of D_2O . The lower diagram shows that when magnetic effects are neglected small but significant errors occur in calculating the frequencies.

It will be observed that, within the experimental error, the bond direction is in fact a principal axis of the quadrupole coupling tensor in this molecule.

A determination of the electric field gradient in a molecule is usually used to provide some information on the relation of the chemical bond to the nucleus under consideration. In the present case, however, the field gradient arises essentially from the superposition of a number of comparatively small effects, and, without detailed calculation based on better information than is currently available, it is not possible to draw any significant conclusions about the OH bond. The magnitudes of the tensor components, however, give quantitative data which must be accounted for by any complete theory of electron distribution, and to that end they provide a guide for the theoreticians.

(b) Interpretation of the Magnetic Coupling Constants

The $c^{(k)}$ are also defined by II, equation (54), and are linear combinations of the $M_{gg}^{(k)}$ of II, equation (3). Partly because the published expression for the $M_{gg}^{(k)}$ is incorrect and partly because of complications in carrying out the required vibrational averaging, it is proposed to discuss the magnetic coupling constants in a later paper.

TABLE 10
QUADRUPOLAR COUPLING TENSOR COMPONENTS

| | |
|--|---------------------------------|
| $\chi_{\xi\xi} = eQ_D V_{\xi\xi} = eQ_D (\partial^2 V / \partial \xi^2)$ | $= 315.2 \pm 7.7 \text{ kc/s}$ |
| $\chi_{\xi\eta} = eQ_D V_{\xi\eta} = eQ_D (\partial^2 V / \partial \xi \partial \eta)$ | $= -8.8 \pm 8.7 \text{ kc/s}$ |
| $\chi_{\eta\eta} = eQ_D V_{\eta\eta} = eQ_D (\partial^2 V / \partial \eta^2)$ | $= -139.3 \pm 7.0 \text{ kc/s}$ |

(c) Comparison with Other Work

Since the completion of the above work Thaddeus and Loubser (1959) have used maser techniques to resolve more completely the hyperfine structure of the HDO transition.* Their experimental results show that the frequencies of lines near $10,278.150 \text{ Mc/s}$ and $10,278.350 \text{ Mc/s}$, unresolved here, lie further

TABLE 11
PRINCIPAL VALUES OF THE QUADRUPOLE COUPLING TENSOR AND OF THE ELECTRIC FIELD GRADIENT TENSOR*

| Quadrupole Coupling Tensor (kc/s) | Electric Field Gradient Tensor (e.s.u.) | |
|-----------------------------------|---|------------------------|
| | Measured | Calculated† |
| $\chi_{XX} = 315 \pm 7$ | $\partial^2 V / \partial X^2 = 1.59 \pm 0.04 \times 10^{15}$ | 3.27×10^{15} |
| $\chi_{YY} = -140 \pm 7$ | $\partial^2 V / \partial Y^2 = -0.70 \pm 0.04 \times 10^{15}$ | -1.49×10^{15} |
| $\chi_{ZZ} = -175 \pm 10$ | $\partial^2 V / \partial Z^2 = -0.89 \pm 0.06 \times 10^{15}$ | -1.78×10^{15} |
| | $ \eta = 0.115 \pm 0.061$ | 0.092 |

* X is rotated $1^\circ 7' \pm 1^\circ 10'$ from the ξ -direction towards the bisector of the $\angle \text{HOH}$ (calculated† -9.5°).

† Bersohn (1960); Bersohn's x, y, z , and Z correspond to our Z, Y, X , and ξ respectively.

from our assigned values than we had estimated; it is for this reason that the footnote in Section II (a) asserts that there is no point to carrying out a recalculation now. However, the overall agreement is very satisfactory since Thaddeus and Loubser find $\alpha^{(Q)}(\text{HDO}) = 411.1 \pm 3.2 \text{ kc/s}$, $(eqQ)_{\text{OD}} = 312.5 \text{ kc/s}$, $|\eta| \leq 0.15$, $c^{(\text{D})}(\text{HDO}) = 12.0 \pm 1.2 \text{ kc/s}$, and $c^{(\text{H})}(\text{HDO}) = 259.8 \pm 2.4 \text{ kc/s}$, in close agreement

* The D_2O line does not seem to be suitable for this type of experimental investigation (Thaddeus, personal communication).

with the results presented here. When Thaddeus and Loubser's values are used to compute a profile for HDO, we find no better agreement with our experimental results than that previously obtained, indicating that the major source of the discrepancies probably lies in our measurement technique.

The combination of Thaddeus and Loubser's value of $\alpha^{(Q)}$ (HDO) with the $\alpha^{(Q)}$'s obtained here for D₂O leads to values for $\chi_{\xi\xi}$ and χ_{xx} of about 305 kc/s.

V. ACKNOWLEDGMENTS

The author wishes to thank Mr. W. E. Smith for many valuable discussions and suggestions, and Dr. R. Bersohn, Mr. P. Thaddeus, and Mr. J. Loubser for making available their results prior to publication.

VI. REFERENCES

- BERSOHN, R. (1960).—*J. Chem. Phys.* **32**: 85-8.
BRUNT, D. (1931).—“The Combination of Observations.” (Cambridge Univ. Press.)
CONDON, E. U., and SHORTLEY, G. H. (1953).—“The Theory of Atomic Spectra.” (Cambridge Univ. Press.)
ELLISON, F. O., and SHULL, H. (1955).—*J. Chem. Phys.* **23**: 2348-65.
HERZBERG, G. (1945).—“Infrared and Raman Spectra of Polyatomic Molecules.” (Van Nostrand: New York.)
KIKUCHI, Y., HIROTA, E., and MORINO, Y. (1959).—*J. Chem. Phys.* **31**: 1139-40.
KOLSKY, H., PHIPPS, T. E., JR., RAMSEY, N. F., and SILSBEY, H. B. (1952).—*Phys. Rev.* **87**: 395-403.
NEWELL, G. P. (1950).—*Phys. Rev.* **78**: 711-4.
OKAYA, A. (1956).—*J. Phys. Soc. Japan* **11**: 258-63.
POSENER, D. W. (1953).—M.I.T. Research Laboratory of Electronics Tech. Rep. No. 255.
POSENER, D. W. (1957).—*Aust. J. Phys.* **10**: 276-85.
POSENER, D. W. (1958).—*Aust. J. Phys.* **11**: 1-17.
POSENER, D. W. (1959).—*Aust. J. Phys.* **12**: 184-96.
QUINN, W. E., BAKER, J. M., LA TOURRETTE, J. T., and RAMSEY, N. F. (1958).—*Phys. Rev.* **112**: 1929-40.
SIMMONS, J. W., and GOLDSTEIN, J. H. (1952).—*J. Chem. Phys.* **20**: 122-4.
THADDEUS, P., and LOUBSER, J. (1959).—*Nuovo Cim.* **13**: 1060-4.

SHORT COMMUNICATIONS

CROSS SECTIONS FOR THE INTERACTION OF 14·5 MeV NEUTRONS WITH MANGANESE AND COBALT*

By E. WEIGOLD†

Cross sections for (n,p) , $(n,2n)$, and (n,α) reactions have been extensively investigated for neutron energies near 14 MeV. However, there are still some gaps, and the present investigations were undertaken to provide neutron cross-section data for nuclei near the proton number 28. Although manganese and cobalt are both monoisotopic elements and, therefore, relatively simple to study by activation techniques, very few measurements have, in fact, been reported.

The target samples in these experiments were in the form of thin circular disks of diameter 0·5 in. sandwiched between a pair of similar copper disks. The sandwiches were irradiated for known periods, shorter than the half-life of the activity to be measured, in a steady flux of $(14\cdot5 \pm 0\cdot5)$ MeV neutrons produced by the ${}^3\text{H}(d,n){}^4\text{He}$ reaction.

After irradiation the activated samples were removed to a heavily shielded scintillation spectrometer employing a 2 in. high by $1\frac{3}{4}$ in. diameter NaI(Tl) crystal, where γ -ray counting was carried out in constant geometry. For ease of calibration of the system only counts in the photo-peak were used. Photo-peak efficiencies, relative to the efficiency for annihilation quanta, were measured experimentally using ${}^{58}\text{Co}$ and ${}^{22}\text{Na}$ to give calibration points close to the energies of the detected γ -rays. The flux at the manganese or cobalt foil was taken to be the mean of the front and back copper monitor foils, whose activities were determined by counting the annihilation quanta emanating from 9·9 min ${}^{62}\text{Cu}$. The radioactive isotopes produced were identified by their radiations and half lives.

The cross sections obtained are relative to a value of (522 ± 20) mbarn for the ${}^{63}\text{Cu}(n,2n){}^{62}\text{Cu}$ reaction (the weighted mean of several published values : Forbes 1952 ; Paul and Clarke 1953 ; and Yasumi 1957) or, in the case of the longer lived activities, relative to a measured value of (1030 ± 95) mbarn for the reaction ${}^{65}\text{Cu}(n,2n){}^{64}\text{Cu}$.

Five or more independent measurements were made for each cross section determined, and the results given below represent the weighted mean of these measurements.

Reaction ${}^{65}\text{Cu}(n,2n){}^{64}\text{Cu}$

Foils of natural copper were irradiated and the annihilation quanta from 12·87 hr ${}^{64}\text{Cu}$ were detected and counted after the 9·9 min ${}^{62}\text{Cu}$ monitoring activity had decayed. Positrons are emitted in 19 per cent. of the ${}^{64}\text{Cu}$

* Manuscript received December 9, 1959.

† Department of Nuclear Physics, Australian National University, Canberra.

disintegrations (Strominger, Hollander, and Seaborg 1958). The cross section relative to the $^{63}\text{Cu}(n,2n)^{62}\text{Cu}$ cross section of (522 ± 20) mbarn was found to be (1030 ± 95) mbarn.

This may be compared with the values of (964 ± 78) mbarn reported by Rayburn (1959) relative to a $^{63}\text{Cu}(n,2n)^{62}\text{Cu}$ cross section of 500 mbarn, (954 ± 130) mbarn by Paularikas and Fink (1959) relative to a $^{63}\text{Cu}(n,2n)$ cross section of 556 mbarn, and (1087 ± 170) mbarn by Paul and Clarke (1953), who find the ^{63}Cu cross section to be (482 ± 70) mbarn.

Reaction $^{55}\text{Mn}(n,2n)^{54}\text{Mn}$

The reaction cross section was obtained by counting the 0.84 MeV γ -rays emitted by 291 day ^{54}Mn , and is (825 ± 185) mbarn.

Reaction $^{55}\text{Mn}(n,\alpha)^{52}\text{V}$

By detecting the 1.43 MeV γ -rays following the β -decay of 3.76 min ^{52}V , the cross section was found to be (27 ± 5) mbarn.

Paul and Clarke (1953) measured a 3.9 min β -activity and attributed the resulting cross section of (52 ± 8) mbarn to the (n,α) reaction. However, the (n,p) reaction leads to 3.6 min ^{55}Cr , a pure β -emitter with end point energy of 2.85 MeV compared to 2.5 MeV for ^{52}V . Paul and Clarke identified their β -activities from half-lives given in the National Bureau of Standards Circular 499 (1952); the 3.6 min ^{55}Cr has been reported subsequently. Their observed β -activity therefore should be due to both the (n,p) and (n,α) reactions. Thus subtraction indicates a value of approximately 25 mbarn for the (n,p) reaction.

Reaction $^{59}\text{Co}(n,2n)^{58}\text{Co}$

Radioactive ^{58}Co is formed both in the 71 day ground state and a 9 hr isomeric state which decays to the ground state. The ground state decays to ^{58}Fe by electron capture or positron emission, followed by a 0.80 MeV γ -ray in 99.5 per cent. of the disintegrations (Strominger, Hollander, and Seaborg 1958). The $^{59}\text{Co}(n,\alpha)$ reaction leads to 2.58 hr ^{56}Mn , whose decay scheme includes a 0.84 MeV γ -ray. By following the 0.8 MeV activity until all the ^{56}Mn and the 9 hr ^{58}Co isomer had decayed, it was found that (45 ± 25) per cent. of the $^{59}\text{Co}(n,2n)$ reactions went through the 9 hr isomeric state.

Measurements of the $(n,2n)$ cross section were made by detecting and counting the 0.80 MeV γ -activity after the decay of the 9 hr isomer. The weighted mean of five independent measurements gives the value of (855 ± 165) mbarn for this cross section.

Reaction $^{59}\text{Co}(n,p)^{59}\text{Fe}$

Heath, Proctor, and Reich (1959) reported that 55.6 per cent. of the disintegrations of 45 day ^{59}Fe were followed by a 1.10 MeV γ -ray, and 44.1 per cent. by a 1.29 MeV γ -ray. Measurement of these γ -ray activities gives an (n,p) cross section of (80 ± 23) mbarn.

Reaction $^{59}\text{Co}(n,\alpha)^{56}\text{Mn}$

The γ -ray activity was corrected for the presence of the 0.8 MeV γ -rays from the $(n,2n)$ reaction. The resulting (n,α) cross section was found to be

(29 ± 6) mbarn relative to the $^{65}\text{Cu}(n,2n)$ cross section. This is in good agreement with the value of (31 ± 3) mbarn relative to a $^{56}\text{Fe}(n,p)$ cross section of 110 mbarn reported by Blosser, Goodman, and Handley (1958).

It is a pleasure to acknowledge the many helpful discussions the author had with Professor E. W. Titterton and Dr. R. N. Glover during the course of this work.

References

- BLOSSER, H. G., GOODMAN, C. D., and HANDLEY, R. H. (1958).—*Phys. Rev.* **110**: 531.
 FORBES, S. G. (1952).—*Phys. Rev.* **88**: 1309.
 HEATH, R. L., PROCTOR, D. G., and REICH, C. W. (1959).—*Bull. Amer. Phys. Soc.* **4**: 278.
 NATIONAL BUREAU OF STANDARDS (1952).—Nuclear data. Circular 499.
 PAUL, E. B., and CLARKE, R. L. (1953).—*Canad. J. Phys.* **31**: 267.
 PAULARIKAS, A., and FINK, R. W. (1959).—*Phys. Rev.* **115**: 989.
 RAYBURN, L. A. (1959).—Reports to the AEC Nuclear Cross Sections Advisory Group : Wash-1018 (March 1959). p. 2.
 STROMINGER, D., HOLLANDER, J. M., and SEABORG, G. T. (1958).—*Rev. Mod. Phys.* **30**: 634.
 YASUMI, S. (1957).—*J. Phys. Soc. Japan* **12**: 443.

A RELATION BETWEEN IONOSPHERIC DRIFTS AND ATMOSPHERIC DYNAMO CURRENT SYSTEMS*

By L. H. HEISLER†

Travelling ionospheric disturbances have been studied at this laboratory over a considerable period using fixed frequency observations on 5·8 Mc/s. They are observed as anomalies in height on ionospheric records at three stations, spaced approximately 40 km apart. Munro (1950) has used normal triangulation techniques to determine speeds and directions and has shown (Munro 1958) that their average speed is 7 km/min with median directions 30° east of north during the winter and 120° east of north by day, during the summer months. In both seasons there is a marked easterly component. However, in recent sunspot maximum years during summer, a predominant westerly component is evident on certain days.

Martyn (1955) has intimated that east-west ionization drifts in the F_2 region are produced by a north-south electrostatic field, communicated from the main conducting region of the ionosphere by the highly conducting path along the lines of magnetic force. Moreover, he suggests that there should be a consequent reversal in direction of drift, depending on the position of the observing station relative to the centres of the atmospheric dynamo current systems. This

* Manuscript received December 16, 1959.

† Radio Research Board Laboratory, Electrical Engineering Department, University of Sydney.

has recently been confirmed by Rao and Rao (1958) and Skinner, Hope, and Wright (1958), who have found drift directions near the magnetic equator, towards the west during the day and towards the east at night, in complete contrast to observations at higher latitudes by Briggs and Spencer (1954).

It seemed probable, therefore, that the observed reversal in east-west component at Sydney ($33^{\circ} 52' S.$, $151^{\circ} 11' E.$) is due to a shift in position of the current focus relative to the observing station. The transitional latitude of

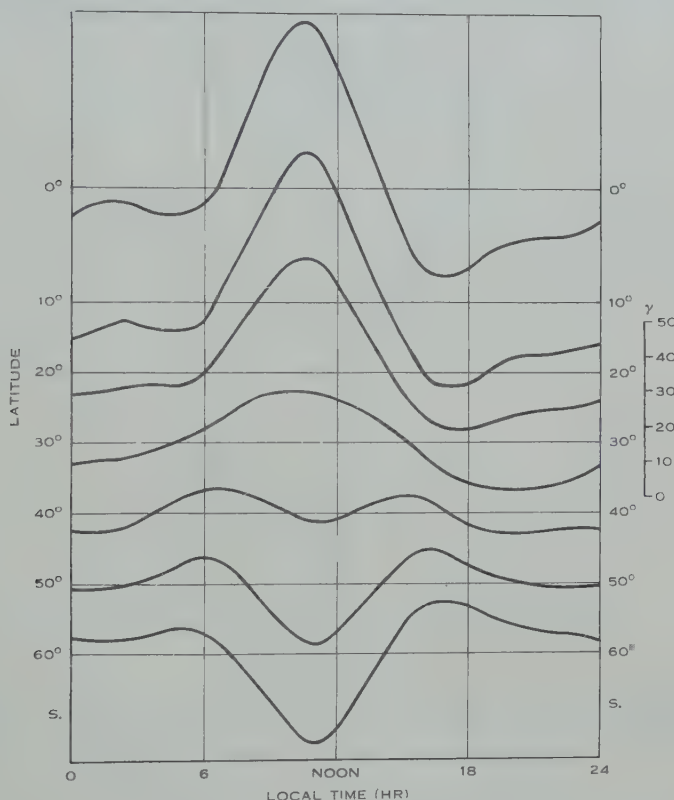


Fig. 1.—Solar daily variation of the north component of the terrestrial field at latitudes 10° apart at the equinoxes in the sunspot-minimum year 1902 (after Chapman and Bartels).

this current centre can change markedly from day to day or even from hour to hour, as shown by Bartels (1932) or in a very complete analysis by Hasegawa (1936). Its relative position can be determined, approximately, from curves expressing the quiet-day diurnal variation of the X component of the Earth's magnetic field for southern latitudes 10° apart during sunspot minimum equinox 1902 (after Chapman and Bartels 1940) as shown in Figure 1. It will be noticed that above 40° the X component displays a maximum, while at high latitudes there is a pronounced minimum in the X component curve. The transition occurs at 40° , the approximate current focus centre. If, therefore, the diurnal

curve of X component shows a maximum, the current focus is south of the observing station and vice versa.

Figure 2 is a set of curves of variation in H , the horizontal component of the Earth's magnetic field at Watheroo ($30^{\circ} 19' S.$, $115^{\circ} 52' E.$), for the magnetically quiet days January 15, 24, 26, 1955. Since variation in declination is very small, these are effectively graphs of the north component of the Earth's field, X . There were numerous disturbances recorded on all days and the median values of the east-west component of the disturbance velocity are 4.3, 3.3, and 4.3 km/min east respectively. The curves are consistent with a current

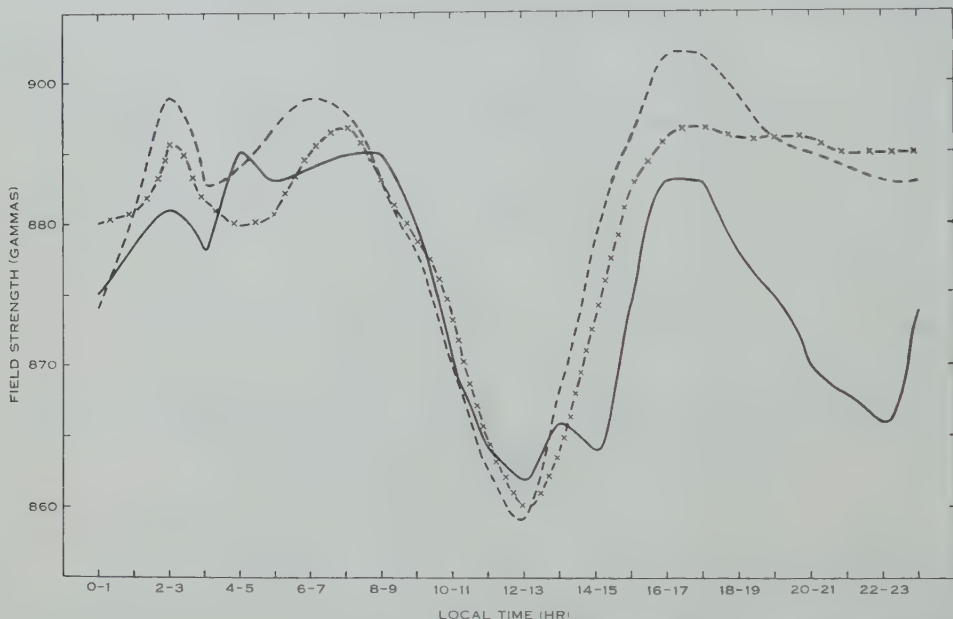


Fig. 2.—Variation in the horizontal component of the Earth's magnetic field at Watheroo for the magnetically quiet days January 15, 24, 26, 1955.

--- January 15, —— January 24, -x-- January 26.

focus travelling to the north of Watheroo and subsequently to the north of Sydney, since Sydney is approximately at the same geographical latitude. A similar set of curves in Figure 3 for the magnetically quiet days January 5, 13, and 14, 1957 are consistent with a current focus travelling to the south of Sydney. Again there were numerous disturbances on all days, but in this case median component velocities were 6.3, 6.4, and 4.4 km/min west respectively. These observed drift directions agree with those suggested by Martyn for the same relative positions of current focus.

Munro (1958) also reports a marked change of directions towards the west after midday during the summer months of the sunspot maximum years 1956–1957. This again is probably due to a southerly movement of the current focus after 1200 hr local time, due to some form of solar control only evident at sunspot maximum.

Observations show that disturbances always have a dominant north-south component. The east-west component, which has a diurnal reversal (Munro 1958), can be explained by the drift hypothesis of Martyn discussed above. The north-south component, however, reverses with season and is apparently independent of geomagnetic control.

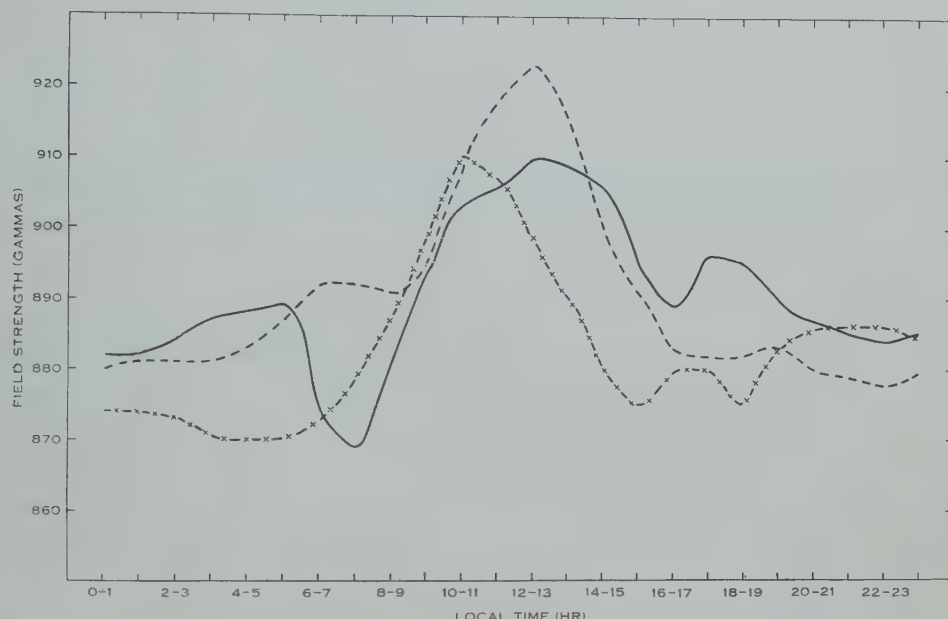


Fig. 3.—Variation in the horizontal component of the Earth's magnetic field at Watheroo for the magnetically quiet days January 5, 13, 14, 1957.
 —×— January 5, - - - January 13, — January 14.

Observation of east-west drift is only possible because of perturbations in the medium. It seems probable, therefore, that the observed directions and velocities of travelling ionospheric disturbances are due to perturbations travelling north-south in an ionized medium which is drifting east-west.

References

- BARTELS, J. (1932).—*Terr. Magn. Atmos. Elect.* **37**: 291-302.
- BRIGGS, B. H., and SPENCER, M. (1954).—*Rep. Progr. Phys.* **17**: 245-80.
- CHAPMAN, S., and BARTELS, J. (1940).—“Geomagnetism.” (Clarendon Press: Oxford.)
- HASEGAWA, M. (1936).—*Proc. Imp. Acad. Japan* **12**: 80-90, 225-8, 277-80.
- MARTYN, D. F. (1955).—“The Physics of the Ionosphere.” pp. 163-5. (Phys. Soc.: London.)
- MUNRO, G. H. (1950).—*Proc. Roy. Soc. A* **202**: 208-23.
- MUNRO, G. H. (1958).—*Aust. J. Phys.* **11**: 91-112.
- RAO, B. R., and RAO, E. B. (1958).—*Nature* **181**: 1612.
- SKINNER, N. J., HOPE, J., and WRIGHT, R. W. (1958).—*Nature* **182**: 1363.

COMMENT ON MULTILAYER DIELECTRIC FILTERS*

By H. L. ARMSTRONG†

A recent note by Gascoigne (1959) on transmission in multilayer dielectric filters is interesting as an example of an adoption to a given problem of a result from an entirely different problem, namely, the Kronig-Penney model for metal lattices. However, one may wonder whether, in the long run, it would not be more economical of time, especially for students, to notice that the multilayer filter, the Kronig-Penney lattice, and for that matter many other problems, are all essentially forms of the same thing.

That is to say, they are all cases in which there are several regions of different properties superimposed. The behaviour of a function is specified in each region, and across the boundaries between regions there is the condition that the function and its gradient be continuous (or, instead of the gradient, there may be something analogous ; e.g. in electromagnetic problems one has the quantities E and H). But this situation is analogous to the cascading of electrical four-terminal networks, where voltage and current are continuous across the junction between adjacent four-terminals. Just as the problem of cascading networks is handled neatly by multiplying matrices, so can the problem involving superimposed layers be handled also by matrices.

In this case one would have two by two matrices relating the values of the function and of its gradient (or of E and H in the electromagnetic problem) at each surface of the layer. There would be one such matrix for each layer, and the superposition of layers would be represented by multiplying the matrices. It has already been shown (Armstrong 1956*a*, 1956*b*) how such a representation can be applied to a great variety of problems. In case the layers happen to be of two kinds placed alternately (and the Kronig-Penny model could be considered as such a situation) one will have results involving powers of matrices, and there are some special relations available to be applied to these (Pease 1952 ; Armstrong 1953, 1956*b* ; Mielenz 1959).

In conclusion, then, the writer would like to suggest that it might be more advantageous for students to become familiar with the general methods of dealing with cascaded or iterated structures by using matrices, rather than by considering every such problem as a special case, for which special methods have to be developed.

It is interesting that, about the same time that Gascoigne's article appeared, there was another, about half-way around the world (Mielenz 1959) dealing with much the same problem. In this latter article matrix analysis is used, as well as some special ways of dealing with powers of matrices.

* Manuscript received December 22, 1959.

† Queen's University, Kingston, Ontario, Canada.

References

- ARMSTRONG, H. L. (1953).—*Proc. Inst. Radio Engrs., N.Y.* **41**: 667.
 ARMSTRONG, H. L. (1956a).—*Matrix & Tensor Quart.* **7**: 11.
 ARMSTRONG, H. L. (1956b).—*I.R.E. Trans. CT-3*: 136, 138.
 GASCOIGNE, S. C. B. (1959).—*Aust. J. Phys.* **12**: 296.
 MIELENZ, K. D. (1959).—*J. Res. Nat. Bur. Stand.* **63A**: 297.
 PEASE, M. C. (1952).—*Proc. Inst. Radio Engrs., N.Y.* **40**: 709.

ON THE FLOW AND EXCHANGE DIFFUSION OF ELECTRONS AND NEGATIVE IONS FORMED BY MOLECULAR ATTACHMENT*

By W. G. KAUMAN†

Formation of negative ions by attachment of electrons to molecules was first recognized by Thomson (1916). Huxley (1959) recently discussed the steady-state structure of a stream of electrons and ions drifting and diffusing in a gas, taking account of ionization by molecular attachment.

In general, there is a finite probability of de-ionization by detachment of electrons, particularly at high ratios of applied field to pressure or when attachment results in a short-lived excited state (Loeb 1955). With detachment non-negligible, the process may be considered as an example of "exchange diffusion"‡ (Kauman 1959) and treated by a method developed for electrodiffusion (Bak and Kauman 1958, 1959). In the present communication we shall show that this method permits separation of the rates of ionization and de-ionization and may be readily applied to non-steady states, alternating fields, and systems with a variety of boundary conditions.

Using Huxley's notation but putting k_1 (instead of $f\nu$) for the rate of ionization and k_2 for the rate of de-ionization, assuming first-order reactions, and neglecting, for simplicity, paired production of positive ions and electrons, we have

$$\partial n / \partial t = D_n \nabla^2 n - \vec{W}_n \cdot \nabla n - k_1 n + k_2 N, \quad \dots \dots \dots \quad (1)$$

$$\partial N / \partial t = D_N \nabla^2 N - \vec{W}_N \cdot \nabla N - k_2 N + k_1 n, \quad \dots \dots \dots \quad (2)$$

where n =number of electrons per unit volume,
 N =number of negative ions per unit volume,
 D_i =diffusion coefficient ($i=n, N$),
 $W_i=em_iE$ =drift velocity,
 e =electronic charge,
 m_i =mobility,
 E =electric field (antiparallel to z -axis).

* Manuscript received December 23, 1959.

† Division of Forest Products, C.S.I.R.O., Melbourne.

‡ "Exchange diffusion" occurs when two species of particles (M_1, M_2), reacting according to $M_1 \rightleftharpoons M_3$, diffuse in an external force field.

The system (1), (2) may be solved by first calculating the result for an instantaneous point source of electrons at $R=0$, $t=0$ and then integrating with respect to time to convert to a continuous source of strength s (electrons per unit time) at the origin (cf. Crank 1956). Neglecting small transient terms and terms above the second order in E , the non-steady-state solution for $\lambda^2 \mathcal{D}_z t \ll 1$ and $\tilde{\lambda}^2 \tilde{\mathcal{D}}_z t \ll 1$ is

$$n \approx \frac{s}{4\pi\kappa} \left[\frac{k_2}{\mathcal{D}^{3/2}} e^{\lambda z} \left\{ \frac{1}{R} \operatorname{erfc} R/2\sqrt{t} - \frac{\lambda^2 \mathcal{D}_z R}{4\sqrt{\pi}} \Gamma(-\frac{1}{2}, R^2/4t) \right\} + \frac{k_1}{\tilde{\mathcal{D}}^{3/2}} e^{\tilde{\lambda} z} \left\{ \frac{1}{\tilde{R}} \operatorname{erfc} \tilde{R}/2\sqrt{t} - \frac{\tilde{\lambda}^2 (\tilde{\mathcal{D}}_z + \kappa) \tilde{R}}{4\sqrt{\pi}} \Gamma(-\frac{1}{2}, \tilde{R}^2/4t) \right\} \right], \quad \dots (3)$$

where

$$\begin{aligned} \mathcal{D}^3 &= \mathcal{D}_x \mathcal{D}_y \mathcal{D}_z, & \tilde{\mathcal{D}}^3 &= \tilde{\mathcal{D}}_x \tilde{\mathcal{D}}_y \tilde{\mathcal{D}}_z, \\ \mathcal{D}_x = \mathcal{D}_y &= [k_2 D_n + k_1 D_N]/\kappa, & \tilde{\mathcal{D}}_x = \tilde{\mathcal{D}}_y &= [k_1 D_n + k_2 D_N]/\kappa, \\ \mathcal{D}_z &= \mathcal{D}_x + \mathcal{D}(E), & \text{with } \mathcal{D}(E) &= [(m_n - m_N)eE]^2 k_1 k_2 / \kappa^3, \\ \tilde{\mathcal{D}}_z &= \tilde{\mathcal{D}}_x - \mathcal{D}(E), & \tilde{R}^2 &= x^2/\mathcal{D}_x + y^2/\mathcal{D}_y + z^2/\mathcal{D}_z, \\ R^2 &= x^2/\mathcal{D}_x + y^2/\mathcal{D}_y + z^2/\mathcal{D}_z, & \tilde{\lambda} &= [k_1 m_n + k_2 m_N]eE/2\mathcal{D}_z \kappa, \\ \lambda &= [k_1 m_n + k_2 m_n]eE/2\mathcal{D}_z \kappa, & & \\ \kappa &= k_1 + k_2. & & \end{aligned}$$

In the steady state, the solution is

$$n = \sum_{r=0}^{\infty} a_{nr} z^r R^{-(r+\frac{1}{2})} K_{r+\frac{1}{2}}(\lambda R \sqrt{\mathcal{D}_z}) + \sum_{r=0}^{\infty} b_{nr} z^r \tilde{R}^{-(r+\frac{1}{2})} K_{r+\frac{1}{2}}(\tilde{\lambda} \tilde{R} \sqrt{(\tilde{\mathcal{D}}_z + \kappa/\tilde{\lambda}^2)}), \quad \dots \dots \dots (4)$$

where $K_{r+\frac{1}{2}}$ are modified Bessel functions of the second kind of order $r+\frac{1}{2}$. The first terms of the series in (4) are

$$n = \frac{s}{4\pi\kappa} \left[\frac{k_2}{\mathcal{D}^{3/2} R} \exp \lambda(z - R \sqrt{\mathcal{D}_z}) + \frac{k_1}{\tilde{\mathcal{D}}^{3/2} \tilde{R}} \exp \tilde{\lambda}(z - \tilde{R} \sqrt{(\tilde{\mathcal{D}}_z + \kappa/\tilde{\lambda}^2)}) \right]. \quad \dots \dots \dots (5)$$

The solutions for N are similar to the above, except that in the absence of a source of negative ions, the sign of the term in $\exp(\tilde{\lambda}z)$ is negative and k_2 in the leading term is replaced by k_1 , with corresponding changes in the coefficients in (4). Assuming an appropriate image source (cf. Huxley 1959), we can make $n=N=0$ at $z=h$ by subtracting from each term in (3), (4), (5) a similar term with z replaced by $2h-z$.

The electronic current to an infinite plane electrode at $z=h$ is, to a first approximation,

$$i_{n\infty} = \frac{es}{\kappa} [k_2 + k_1 \exp \tilde{\lambda}h \{1 - \sqrt{(1 + \kappa/\tilde{\lambda}^2 \tilde{\mathcal{D}}_z)}\}]. \quad \dots \dots \quad (6)$$

If $W \gg 4D_n k_1$, $k_1 \gg k_2$, and $m_n \gg m_N$, (5) and (6) reduce to Huxley's equations (9) and (11).

If the applied field alternates with frequency $\omega/2\pi$, the results are of the same form as above, but the series terms are more complicated and depend also on ω , and $\mathcal{D}(E)$ (cf. equation (3)), averaged over a cycle, is

$$\tilde{\mathcal{D}}_i(E) = -\frac{E_0^2}{8\kappa} \left\{ \frac{4\omega^2 m_i^2}{\omega^2 + \kappa^2} - (m_n + m_N)^2 \left(1 - \frac{(k_1 - k_2)^2}{\omega^2 + \kappa^2} \right) \right\}, \quad \dots \quad (7)$$

where $E_0/\sqrt{2}$ = root-mean-square field. Further, $\lambda = [(m_n + m_N)eE_0 \cos \omega t]/2\mathcal{D}_z$, and similarly for $\tilde{\lambda}$.

The general equations (1) and (2) may also be solved with finite boundary conditions, for instance $n(0,t) = N(0,t) = \frac{1}{2}C_0$, $n(h,t) = N(h,t) = \frac{1}{2}C_h$, $(C_0 - C_h)/h = g \ll C_0$. The one-dimensional steady-state solution for $k_1 = k_2 = k$, $|m_n - m_N| \ll k$ is then of the form

$$\begin{aligned} n \approx & \frac{1}{2}g(h-z) + \frac{1}{2}C_h + \frac{gm_e E}{4k} \left\{ 1 - e^{-\Lambda z} - e^{\Lambda(z-h)} \right\} \\ & + \frac{gm^2 e^2 E^2}{4k\sqrt{2kD}} \left\{ \frac{2z}{h} - 1 + e^{-\Lambda z} - e^{\Lambda(z-h)} \right\} + 0[(m_n - m_N)/k], \quad \dots \quad (8) \end{aligned}$$

where $\Lambda \sim meE/D$ and D, m are mean values.

It is important to note that in the systems described, the divergence of the electric field is finite, and the drift velocity of the particles therefore is not constant. For instance, the electric field corresponding to the system described by equation (8) is of the order

$$E \approx E_a + (e/\epsilon)C_h(\frac{1}{2}h - z), \quad \dots \dots \dots \quad (9)$$

where E_a = applied field, ϵ = permittivity. The effect of the divergence of E may be taken into account by perturbation procedures. In the presence of a species of positive ions not taking part in the exchange diffusion, the divergent term of the field is, to a first approximation, $\{eE_a(C_0 - C_h)/2h(C_0 + 3C_s)\}(z - \frac{1}{2}h)$, where C_s is the concentration of the positive ions. The electric current in this case is

$$I \approx -e^2 \frac{m_n + m_N}{2} \left\{ 2C_s + C_0 - \frac{ge(m_n - m_N)E_a}{2k} \right\} E_a. \quad \dots \dots \quad (10)$$

With an alternating field, I is the form $I(\text{alt.}) = I_0 + I_1 \sin \omega t + I_2 \cos 2\omega t$, where I_0 and I_2 are independent of C_s but depend on k, m , and ω with a cut-off frequency given by $\omega = 2k$ (Kauman and Bak 1959).

The present method not only permits a complete description of the behaviour of electrons and ions formed by molecular attachment, but is also amenable to the treatment of other electronic exchange processes, for instance transport of carriers in semiconductors (cf. van Roosbroeck 1950; Shockley 1950). It may be extended to more than two ionic species by iteration procedures.

References

- BAK, T. A., and KAUMAN, W. G. (1958).—*J. Chem. Phys.* **28**: 509.
 BAK, T. A., and KAUMAN, W. G. (1959).—*Trans. Faraday Soc.* **55**: 1109.
 CRANK, J. (1956).—“The Mathematics of Diffusion.” p. 30. (Clarendon Press: Oxford.)
 HUXLEY, L. G. H. (1959).—*Aust. J. Phys.* **12**: 171.
 KAUMAN, W. G. (1959).—Contribution à la théorie de l'électrodiffusion. Thèse, Université Libre de Bruxelles.
 KAUMAN, W. G., and BAK, T. A. (1959).—*Acad. Roy. Belg., Cl. Sci. (5)* **45**: 278.
 LOEB, L. B. (1955).—“Basic Processes of Gaseous Electronics.” (Univ. of Cal. Press.)
 VAN ROOSBROECK, W. (1950).—*Bell Syst. Tech. J.* **29**: 560.
 SHOCKLEY, W. (1950).—“Electrons and Holes in Semiconductors.” (Van Nostrand: New York.)
 THOMSON, J. J. (1916).—*Phil. Mag.* **30**: 321.

MAGNETIC ANISOTROPY OF DISPERSED POWDERS*

By F. D. STACEY†

It is well known that in most rocks the ferromagnetic fraction occurs as small grains dispersed in a solid, magnetically inert matrix. Recently the magnetic anisotropy of rocks and of chondritic meteorites has been subjected to detailed study by the torque-meter method, and, in an attempt to obtain a physical understanding of the shape and crystal alignments of grains which cause magnetic anisotropy in these natural bodies, a number of artificial specimens have been prepared. Iron, nickel, and magnetite powders were mixed into solidifying media and allowed to set in a cylindrical mould in a 10 kilo-oersted field. The torque curves of the resulting specimens reveal a surprising result. It appears that single crystal magnetic grains tend to string together along lines of force, thus producing strongly anisotropic specimens, only when the first magnetocrystalline anisotropy constant of the ferromagnetic material is positive.

The Torque-meter Experiment

Torque meters are generally used to measure magnetic anisotropy, and Bozorth (1951) has summarized the method and the results which have been obtained with single crystals. For measurements on rocks the simple instrument shown in Figure 1 is adequate. The torsional suspension T is a 7.5 cm length

* Manuscript received December 30, 1959.

† Geophysics Department, Australian National University, Canberra.

of 0·45 mm diameter phosphor-bronze wire, hanging from a needle *N*, which can be turned by hand round a 360° scale *H* in a horizontal plane. A brass rod *R* with an adjustable mirror *M* clipped to it is soldered to the lower end of the suspension; cylindrical specimens are stuck to this rod with wax and hang freely. Only very strongly magnetic, light specimens need to be weighted. The torque meter is placed so that the specimens hang symmetrically in the field gap of an electromagnet (Stacey 1959), which is used in this experiment with 10·8 cm

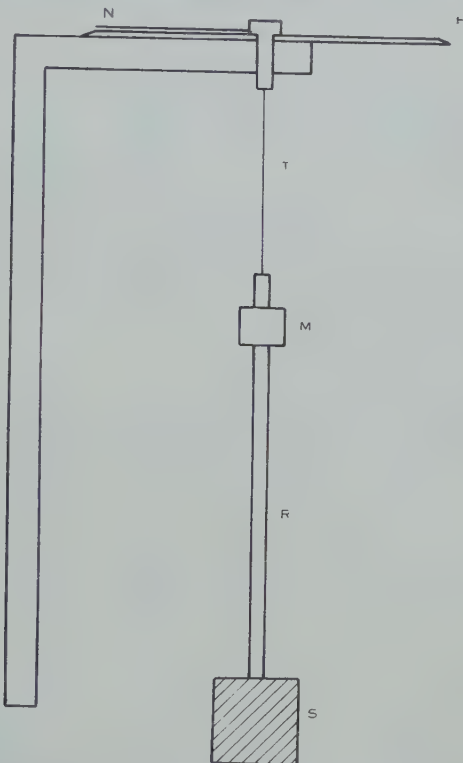


Fig. 1.—Simple torque meter for anisotropy measurements on rocks. The magnetic field is applied perpendicular to the plane of the diagram.

plane pole faces and normally operated at 10·6 kilo-oersteds over a gap of 4·0 cm. The mirror is used with a galvanometer lamp and scale for sensitive observations of the angle of the specimen.

To make a measurement the needle is set to a predetermined angle θ and the mirror adjusted to bring the light spot into the middle of the scale. The field is switched on and the rotation of the specimen is compensated by turning the needle through an angle $\Delta\theta$ to return the light spot to its original position. Then $\Delta\theta$ is the angle through which the suspension has been twisted to oppose exactly the magnetic torque on the specimen. This process is repeated at $\theta=0^\circ$, 10° , 20° , . . . , to 180° , and sometimes to 360° as a check. Then $T=\alpha\Delta\theta$ versus θ is the torque curve of the specimen, where α is the torsional constant of the

TABLE I
ANALYSED COMPONENTS OF TORQUE CURVES
All measurements at 10.6 kilo-oersteds except where noted for specimen 3. Amplitudes T_2 , T_4 , T_6 are in dyne-cm.

| Specimen | Material | Type | Quantity (mg) | Matrix | Total | | | Per cm ³ of Ferromagnetic | T_4/T_2 |
|----------|-----------|--------------------------|---------------|---|--------------------------|---|--------------------|--------------------------------------|---|
| | | | | | T_2 | T_4 | T_6 | | |
| 1 | Steel | Two balls | 32.6 | Houssehol'd cement | $(\pm 0.1) \times 10^3$ | $(-1.0) \times 10^3$ $(\pm 0.1) \times 10^3$ | 0.17×10^3 | 14.4×10^5 | -2.3×10^5 0.4×10^5 -0.16 ± 0.02 |
| 2 | Iron | Mond carbonyl grade MCP | 100 | Plaster of paris | $(\pm 0.5) \times 10^3$ | $(-3.3) \times 10^3$ $(\pm 0.5) \times 10^3$ | 17.1×10^5 | -2.6×10^5 | -0.15 ± 0.03 |
| 3 | Iron | Mond carbonyl grade MCP | 50 | Plaster of paris | $(\pm 0.15) \times 10^3$ | $(-1.3) \times 10^3$ $(\pm 0.15) \times 10^3$ | 0.3×10^3 | 17.1×10^5 | -2.0×10^5 0.4×10^5 -0.12 ± 0.02 |
| 3* | | | | | $(\pm 0.15) \times 10^3$ | $(-1.5) \times 10^3$ $(\pm 0.15) \times 10^3$ | 0.4×10^3 | 14.5×10^5 | -2.4×10^5 0.7×10^5 -0.16 ± 0.02 |
| 4 | Iron | Mond carbonyl grade MF | 50 | Plaster of paris | $(\pm 0.06) \times 10^3$ | $(-0.63) \times 10^3$ $(\pm 0.06) \times 10^3$ | 0.12×10^3 | 7.17×10^5 | -1.0×10^5 0.2×10^5 -0.14 ± 0.15 |
| 5 | Nickel | Mond carbonyl grade A | 150 | Plaster of paris | $(\pm 0.03) \times 10^3$ | -30 ± 30 | | 0.24×10^5 | -0.02×10^5 -0.07 ± 0.07 |
| 6 | Nickel | Serritt-Gordon grade C50 | 150 | Plaster of paris | | < 10 | < 10 | $< 0.006 \times 10^4$ | $< 0.006 \times 10^4$ — |
| 7 | Nickel | Serritt-Gordon grade C50 | 200 | Benzoic acid + pyrex powder (solidification point 122 °C) | $(\pm 0.4) \times 10^3$ | $(-4.8) \times 10^3$ $(\pm 0.4) \times 10^3$ | 1.4×10^3 | 11.0×10^5 | -2.1×10^5 0.6×10^5 -0.19 ± 0.15 |
| 8 | Nickel | Serritt-Gordon grade C50 | 50 | " Armo wax " + pyrex powder (solidification point 132 °C) | $(\pm 0.5) \times 10^3$ | $(-7.3) \times 10^3$ $(\pm 0.5) \times 10^3$ | | 57.0×10^5 | -12.9×10^5 — |
| 9 | Magnetite | BDH artificial powder | 100 | Plaster of paris | 50 ± 20 | < 10 | | 0.02×10^5 | $< 0.005 \times 10^5$ — |

* Same specimen at 6.5 kilo-oersteds.

suspension. $\Delta\theta$ can be measured to about 0.2° , which is somewhat less than 1 per cent. of the maximum normally usable deflection. For very weakly anisotropic specimens the direct observation of $\Delta\theta$ is inaccurate and a more sensitive method uses calibrated deflections of the light spot without movements of the needle.

For convenience the artificial specimens are set in the torque meter so that their known axes of anisotropy coincide with the field direction when the scale reading is zero. Their torque curves can then be resolved into even harmonics in θ :

$$T(\theta) = T_2 \sin 2\theta + T_4 \sin 4\theta + T_6 \sin 6\theta + \dots \quad \dots \quad (1)$$

Small disturbing terms T_0 and $T_1 \sin(\theta + \varphi)$, (φ representing arbitrary phase) may also appear. The T_0 term is due to rotational hysteresis and is generally observable only at low fields (a specimen at $\theta + 10^\circ$ tends to "remember" the magnetization it acquired at θ and thus experience a torque independent of θ). The T_1 term may be observed with specimens having unevenly distributed magnetic material, suspended asymmetrically in the field. It has been noticed with a few rocks, but with none of the artificial specimens.

Experimental Results

It is to be expected that spherical, polycrystalline grains of ferromagnetic material, immersed in a non-magnetic paste and exposed to a strong magnetic field, will tend to align themselves in strings along the lines of force. The specimen which is formed when the paste has set will have a magnetic anisotropy which may be simulated by a pair of individually isotropic ball-bearings stuck together as specimen 1 (see Table 1). The similarity of the torque curves of the other specimens to that obtained with specimen 1 is a strong indication that the observed anisotropies were principally due to the stringing together of magnetic particles.

However, in spite of the similarity of shape of all the torque curves, their amplitudes differ most remarkably. The specimens of nickel and magnetite powder, which were mixed with about 1000 times their own volume of plaster of paris (5, 6, and 9), wetted, and allowed to set in the field for about 5 hr, exhibited very little or no anisotropy, whereas the iron specimens (2, 3, and 4), prepared in the same way, were strongly anisotropic.

We may consider the behaviour of a specimen containing single (cubic) crystal magnetic particles which rotate in the setting field to give [100] crystal alignment with the field and random crystal directions in the perpendicular plane. Neglecting the stringing effect it would have a torque curve given by

$$T = K_1 \left(\frac{1}{8} \sin 2\theta + \frac{7}{16} \sin 4\theta \right) + K_2 \left(\frac{1}{128} \sin 2\theta + \frac{1}{32} \sin 4\theta - \frac{3}{128} \sin 6\theta \right), \quad \dots \quad (2)$$

where K_1 and K_2 are the first and second magnetocrystalline anisotropy constants of the material. Since for iron $K_1 \sim +4 \times 10^5$ ergs cm^{-3} and K_2 is negligible for this purpose, it is apparent that the sign of the $\sin 4\theta$ term in the measured

torque curves is opposite to that which would result from crystal alignment. Further, no distinction can be made between the shapes of the torque curves for the specimens containing iron (2, 3; and 4) and the curve for the pair of ball-bearings (specimen 1), so that crystal alignment does not contribute to the anisotropy of the iron specimens. This is expected from the polycrystalline nature of carbonyl iron powder (Pfeil 1947).

The torque exerted on specimen 3 with its axis of anisotropy at a fixed angle (30°) to a variable field H was measured over the range $3.9\text{--}11.5$ kilo-oersteds. It showed the normal linear variation in $1/H$ above about 8 kilo-oersteds and extrapolated to a value at $(1/H=0)$ 18 per cent. higher than at $H=10.6$ kilo-oersteds. Comparison of the torque curves of specimen 3 at 6.5 and 10.6 kilo-oersteds showed that it is only the $\sin 2\theta$ term which increases with increasing field. The $\sin 4\theta$ and $\sin 6\theta$ terms decrease in magnitude. The decrease in T_6 is so strong that this term extrapolates to zero at $(1/H=0)$ within the limits of experimental error. The extrapolated ratio T_4/T_2 is approximately -0.07 . However, the striking, qualitative difference between the torque curves of the iron and nickel specimens is not influenced by the magnitude of the field in which the measurements are made.

There is another experimentally variable parameter in the particular case of nickel, in which the first magnetocrystalline anisotropy constant is negative at room temperature but becomes positive (iron-like) above about 100°C . Specimens 7 and 8 were made by mixing weighed samples of nickel powder with pyrex powder and either benzoic acid or "Armo wax" (Armour Chemical Division) to form a thick paste at about 150°C ; the specimens were then allowed to cool in beakers in the 10.6 kilo-oersted field, so that they solidified well above 100°C (see Table 1). The anisotropies of the specimens of nickel powder set in this way were more than 1000 times stronger than for the same grade of powder set in plaster at room temperature.

Discussion

The shape of the torque curves can be explained almost entirely in terms of a stringing together of grains. It is surprising therefore that of the specimens which had been set at room temperature only those containing iron showed this effect. A correlation with magnetocrystalline anisotropy is indicated by the torque curves of specimens containing nickel powder which had been set above 100°C (7 and 8) and which showed very strong anisotropy similar to that of the iron specimens. Above about 100°C the first magnetocrystalline anisotropy constant becomes positive (iron-like) (Honda, Masumoto, and Shirakawa 1935; Bozorth 1951).

A physical difference between the iron and nickel powders must be noted. Carbonyl iron powders are polycrystalline, but when nickel powder is produced "the particles tend to be single crystals and to possess an idiomorphic shape" (Pfeil 1947). Microscopic examination of the magnetite grains used in specimen 9 showed that these also had irregular but characteristic shapes indicative of single crystals. The conclusion may therefore be advanced that polycrystalline magnetic particles (iron, specimens 2, 3, 4) or single crystals with positive magneto-

crystalline anisotropy (nickel set above 100 °C, specimens 7, 8) tend to string together along lines of force when exposed to a magnetic field. Single crystals with negative magnetocrystalline anisotropy (nickel below 100 °C, specimens 5, 6, and magnetite, specimen 9) do not show this effect. No mechanical explanation for this difference in behaviour can be offered at present.

The torque curves can also be examined for details indicative of micro-crystalline alignment. For material with positive magnetocrystalline anisotropy this would be most apparent as an increase in the $\sin 4\theta$ term in the torque curve by the addition of a term having the form of equation (2) to the curve due to the stringing effect. This means a decrease in magnitude of the negative coefficient T_4 relative to the magnitude of T_2 . Experimental uncertainty in determining the ratio T_4/T_2 (see Table 1) does not permit any distinction to be made between specimens 2, 3, and 4, so that carbonyl iron powders of grades MCP and MF are evidently both polycrystalline, as mentioned above.

The occurrence of a magnetocrystalline term in the torque curves of specimens 7 and 8 appears possible, particularly in the latter. At high temperatures the nickel powders would experience [100] crystal alignment in the field, so that with this alignment frozen in at room temperature the addition to the torque curve of a term having the form of equation (2) with negative K_1 will increase the magnitude of the negative T_4 term relative to T_2 . The increase in $(-T_4/T_2)$ which was observed for specimen 8 is well outside experimental error and is consistent with crystal alignment in the nickel powders at high temperatures.

The difference between specimens 5 and 6 is evidently the result of a real physical difference between the nickel powders used. The Sherritt-Gordon grade C50 powder gave no measurable anisotropy at all, whereas exactly the same treatment of a sample of Mond carbonyl grade A powder resulted in a specimen of very small but readily measurable anisotropy. If the foregoing conclusion that anisotropy will only appear if the grains are polycrystalline or have positive magnetocrystalline anisotropy is correct, then it appears that the Sherritt-Gordon powder is entirely composed of single crystal grains, but that the Mond powder contains a small but noticeable fraction of polycrystalline grains.

Powders for these experiments were provided by the Mond Nickel Company, London, and Sherritt-Gordon Mines Ltd., Alberta, Canada.

References

- BOZORTH, R. M. (1951).—"Ferromagnetism." (D. Van Nostrand : New York.)
HONDA, K., MASUMOTO, H., and SHIRAKAWA, Y. (1935).—*Sci. Repts. Tohoku Imp. Univ.* **24** : 391.
PFEIL, L. B. (1947).—The nature, properties and applications of carbonyl iron powder. Symposium on powder metallurgy. (Iron and Steel Institute : London.)
STACEY, F. D. (1959).—*J. Sci. Instrum.* **36** : 328.

ELECTRON BACKGROUND IN NUCLEAR EMULSIONS*

By V. D. HOPPER† and JEAN E. LABY†

Since 1951 supplies of Ilford G5 electron sensitive nuclear emulsions have been flown by air to Australia. In 1954 it was observed that some batches, when developed soon after arrival, showed an excess electron background which made them unsuitable for the cosmic ray work for which they were imported.

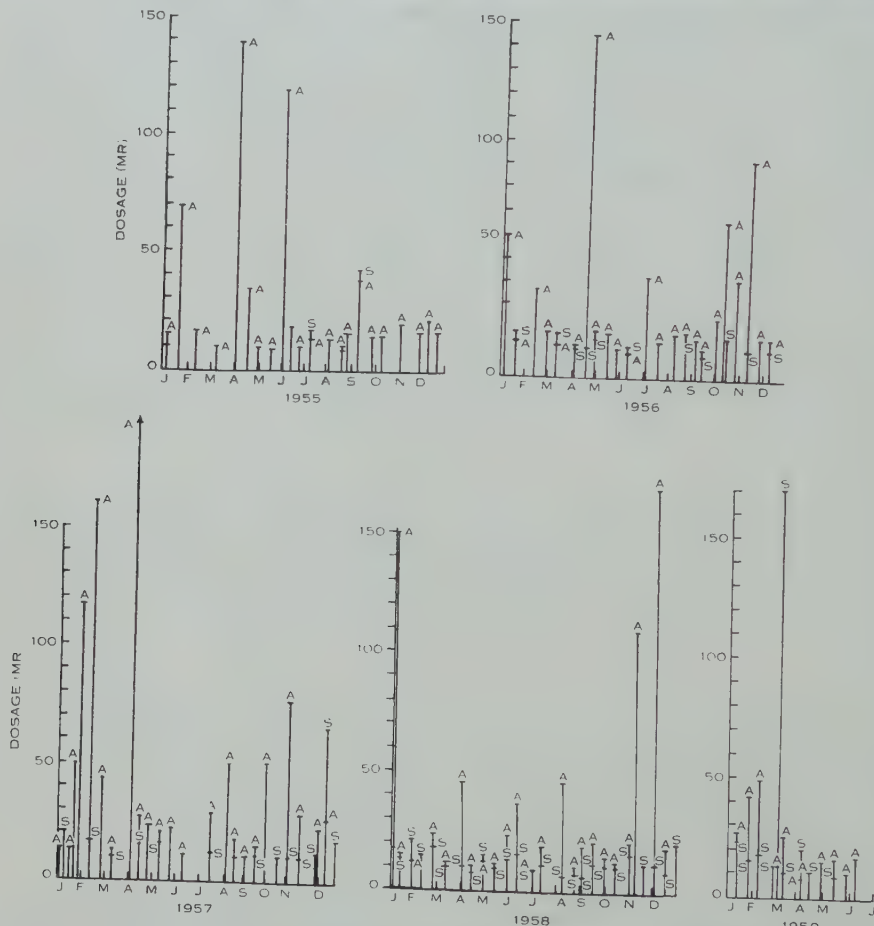


Fig. 1.—Dosage in milliröntgens received by electron sensitive emulsions arriving by air from England (A), and arriving by ship (S) over the period 1955 to 1959 (June).

It was then decided that a test development was required for all emulsions before they could be safely used in the high altitude studies. It was also considered necessary to import samples by ship to determine whether emulsions would be more suitable if imported by this means.

* Manuscript received January 5, 1960.

† Physics Department, University of Melbourne.

Results of the dosage received by samples arriving throughout the period January 1955–June 1959 are given in Figure 1, where plates sent by air are marked A and those by sea S. The electron background dosage in milliröntgens calibrated as described earlier[†] is plotted against the approximate date of manufacture. Correlation of the heavy dosage samples with radioactive rainfall in France was noted earlier.*

The emulsions consisted of 600 micron thick Ilford G5 emulsion on glass backing. The size of the plates was 3 by 2 in., and these were packed in cardboard packets holding 6 or 12 plates. The packets were in turn protected with a layer of wood shavings placed inside wooden boxes. These boxes were labelled photographic material and the label specified that the packet should be kept 10 ft from any radioactive material. Comments regarding radiation due to instrument panels etc. are made in the previous communication on this subject. The same method of packing has been made throughout the duration of this test.

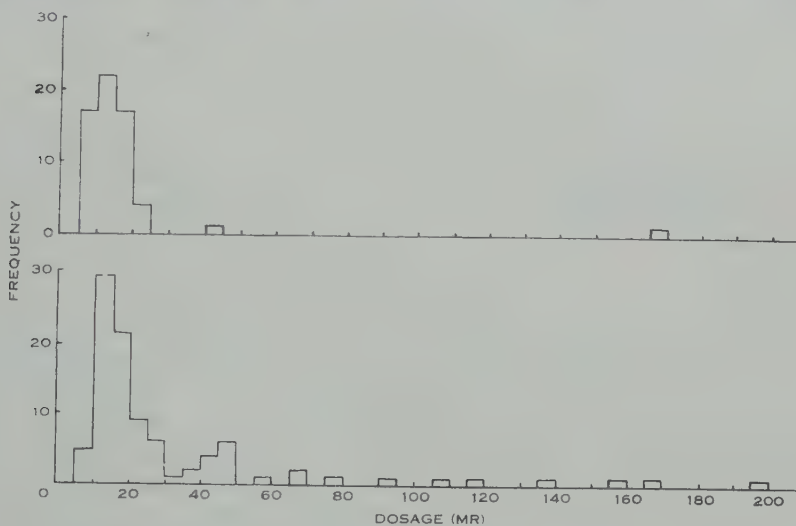


Fig. 2.—Histogram showing the frequency of dosage: (above) plates arriving by ship, (below) plates arriving by air.

It has been the standard practice of Ilford Ltd. to dispatch plates within about 3 days of manufacture and to mark the manufacture date on the box carrying the plates.

Figure 2 shows the histograms for plates arriving by sea and by air and clearly shows that air-flown samples are more prone to excess radiation damage than those arriving by sea. (The mean air transport time was 38 hr at 10,000–20,000 ft, climbing and descending time about 8 hr.)

Only two samples out of 60 of those arriving by sea showed an exposure exceeding 25 mr. One sample was manufactured in September 1955 and the corresponding sample which arrived by air also showed excessive exposure.

* HOPPER, V. D., and LABY, JEAN E. (1955).—*Aust. J. Phys.* 8 : 557.

The other sample, manufactured on March 2, 1959, showed a very high exposure (170 mr), whereas the corresponding sample arriving by air showed low exposure (13 mr). The reason for this difference has not been determined.

Results show that it is advisable to import nuclear emulsion plates by sea rather than by air, although there is still some chance of excessive exposure. The use of the electron sensitive emulsions in radiation measurements is also shown to be useful for determination of low dosages, particularly as the electron tracks can be distinguished from darkening produced by other means such as exposure to light and chemical fogging due to excess temperatures. Further tests are being carried out with the method on aircraft travelling on different routes in the southern and northern hemispheres.

RELATIVE INTENSITY OF THE 17·2 AND 14·3 MEV GAMMA RAYS FROM THE ${}^7\text{Li}(p,\gamma){}^8\text{Be}$ REACTION*

By B. MAINSBIDGE†

Radiation from proton capture in ${}^7\text{Li}$ is known to consist of two principal components of energy $(17\cdot2 + \frac{7}{8}E_p)$ and $(14\cdot3 + \frac{7}{8}E_p)$ MeV, corresponding to transitions to the ground state and first excited state of ${}^8\text{Be}$ respectively (Walker and McDaniel 1948). Resonances in the reaction are known to exist at $E_p = 441$ keV, 1·03 and 2·1 MeV (Bonner and Evans 1948; Kraus 1954; Price 1954) and the relative intensity of the two γ -rays is known to vary in the neighbourhood of the 441 keV resonance (Campbell 1956). It is not known if the intensity ratio varies in the region of the 1030 keV resonance and this experiment was designed to repeat the measurements of Campbell and extend the investigation to the higher resonance.

Experimental

The detector was a 5 in. diameter by 4 in. long NaI(Tl) crystal mounted, with the cylindrical axis vertical, at 90° to the proton beam and 9·5 in. from a $\frac{3}{16}$ in. diameter natural lithium target. The γ -radiation was collimated into the crystal centre by a conical hole through a lead block 3 in. thick. The collimator was tapered so that the detector observed, through a solid angle of 0·074 steradians, a $\frac{3}{16}$ in. diameter spot at the target. A 5 in. diameter Dumont 6364 photomultiplier was mounted on the crystal and the output was amplified and fed to a 100 channel pulse-height analyser, biased at 6 MeV γ -ray energy.

* Manuscript received March 7, 1960.

† Research School of Physical Sciences, Australian National University, Canberra.

The targets, prepared by the evaporation of natural lithium metal onto silver-plated brass backings, were mounted on a water-cooled holder and inclined at 20° to the proton beam. The deposits were as thin as experimental conditions would allow and were less than 5 keV thick for measurements between $E_p = 430$ and 450 keV. Up to $E_p = 600$ keV, 5–10 keV thick targets were used and in the remaining energy regions they were 20 keV thick except for the measurements below 300 keV, where the low yield required targets 60 keV thick.

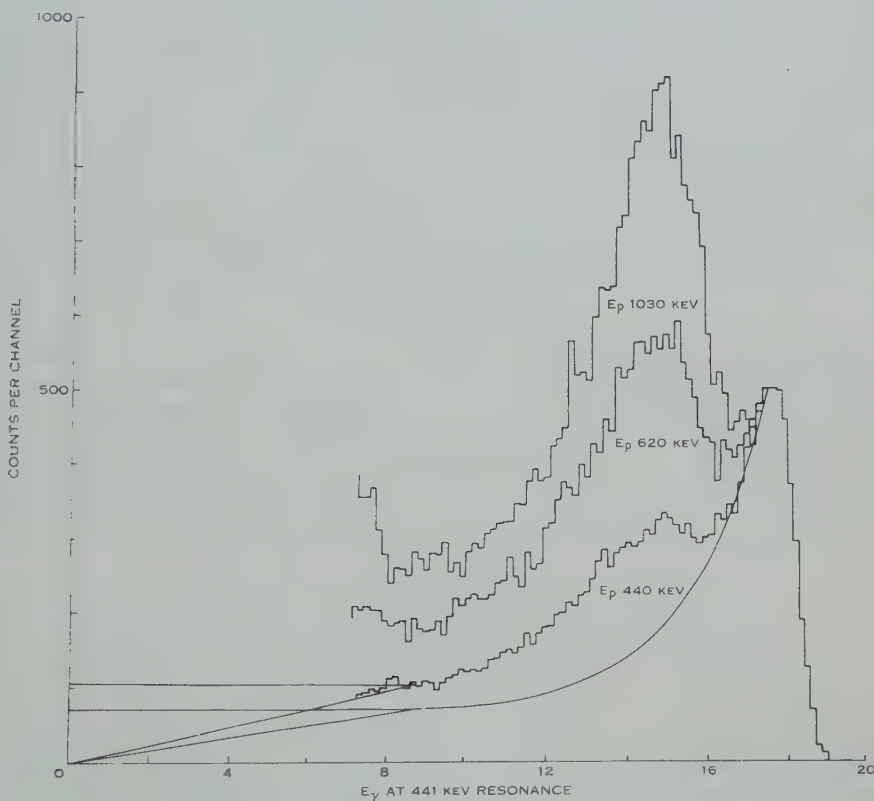


Fig. 1.—Pulse-height distributions of the ${}^7\text{Li}(p,\gamma){}^8\text{Be}$ radiation at $E_p = 440$, 620, and 1030 keV.

Beam currents of 10–15 μA were used and the charge was measured on a current integrator. In the region of the 441 keV resonance, the current was reduced to limit counting rates to 100 p.p.s.

The bias and gain of the pulse-height analyser were fixed during the measurement so that the peak of the 17.6 MeV γ -ray always occurred in the same channel of the display. The cosmic ray background was measured by running the electronics for 2–3 hr with the accelerator switched off.

Figure 1 shows typical spectra obtained in the measurement after correction for cosmic ray background and normalizing to a common peak height at 17.6 MeV.

Pulse-height Distribution of the 17·6 MeV γ -Ray

The pulse-height distributions of the two γ -rays cannot be obtained directly from the spectra of Figure 1 because of the overlap in the two components. The separation is complicated by the 2 MeV width of the 14·8 MeV γ -ray.

The 17·6 MeV component is monochromatic and investigations of the response of 5 in. diameter by 4 in. long NaI(Tl) crystals to monochromatic radiation between 10 and 20 MeV suggest there is little change in the pulse-height distributions in this energy range (Kockum and Starfelt 1959). A comparison of the pulse-height distributions of the 16·6 and 20·3 MeV γ -rays from proton capture in ^{11}B and ^3H respectively, measured with the apparatus of the present investigation, showed the line shapes to be identical and it was assumed that the

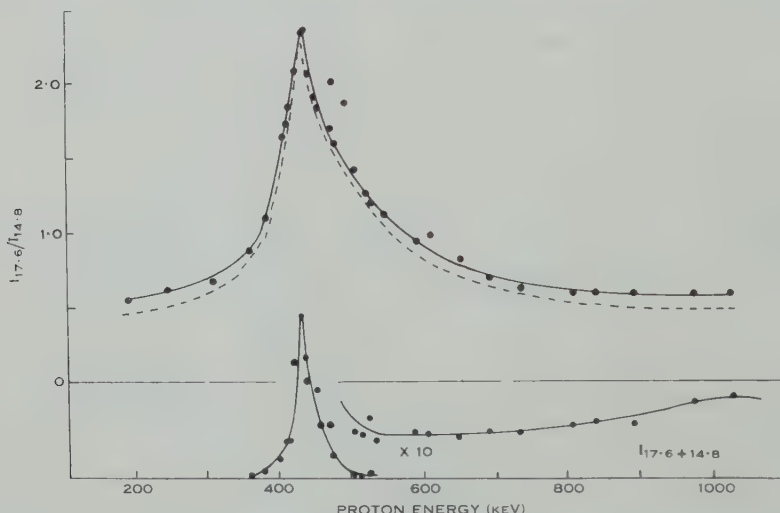


Fig. 2.—Variation of the intensity ratio with proton energy, measured at 90° to the proton beam.

pulse-height distribution of the 20·3 MeV γ -ray could be used to represent that of the 17·6 MeV γ -ray. This was obtained by replacing the lithium target with one of tritium absorbed in zirconium and bombarding with 850 keV protons. The gain of the photomultiplier was altered so that the peak of the 20·3 MeV γ -ray coincided with that of the 17·6 MeV component and the line shape is included in Figure 1.

Line Shape below $E_\gamma=8\cdot5 \text{ MeV}$

The pulse-height distributions do not indicate the line shape below $E_\gamma=8\cdot5 \text{ MeV}$. In this region, contributions from the $^{19}\text{F}(p,\alpha,\gamma)^{16}\text{O}$ reactions are mixed with low energy γ -rays from scattered radiation. Many of these events arise from scattering material outside the detector and some are due to the escape of a fraction of the incident γ -ray energy from the detector. The actual line shape between 0 and 8·5 MeV depends on the escape loss and is partly determined by the dimensions of the collimator. It was inferred from

the investigations of Kockum and Starfelt (1959) that the line shape for the geometry of the present experiment was between the limits in the extrapolations to zero energy in Figure 1.

Calculation of the Intensity Ratio

Each spectrum was summed between $E_\gamma = 8.5$ and 19.5 MeV and the cosmic ray background was subtracted. The assumed pulse-height distribution of the 17.6 MeV γ -ray was normalized to fit each spectrum and the intensity of the 14.8 MeV component was obtained by subtraction. Small corrections were made for the calculated efficiency of the detector to 14.8 and 17.6 MeV γ -rays, 82.9 and 84.5 per cent. respectively. The ratio of the intensity of the two components $I_{17.6}/I_{14.8}$ is shown as a function of proton energy in Figure 2. The excitation function was derived from the ratio of the total number of events between 8.5 and 19.5 MeV and the current integrator counts. Four targets of varying thickness were used in the measurements and, since the yield from each target at the 441 keV resonance has been normalized to a common value, the excitation function is only approximate.

Absolute Value of the Ratio

The experimental points in Figure 2 are based on the pulse-height distributions above $E_\gamma = 8.5$ MeV. The errors in the absolute values of the ratio, due to the uncertainty in the line shapes below this energy, have been calculated by considering the extrapolations of Figure 1. The absolute value lies between the experimental curve and the broken curve of Figure 2.

TABLE 1
MEASUREMENTS OF THE INTENSITY RATIO AT THE 441 keV RESONANCE

| E_p | Target Thickness | Angle | $I_{17.6}/I_{14.8}$ | Reference |
|-------|------------------|-------------------------------|---------------------|-----------------------------|
| 450 | 10–20 keV | $0^\circ, 90^\circ$ | 2 ± 0.2 | Devons and Lindsey (1950) |
| 460 | 150 keV | 0° | 2 | Walker and McDaniel (1948) |
| 500 | thick | $0^\circ, 35^\circ, 70^\circ$ | 1.7 ± 0.2 | Stearns and McDaniel (1951) |
| 441 | 5 | 90° | 2.30 ± 0.04 | Present work |

Discussion

The points at $E_p = 480$ and 500 keV show higher values of the ratio than neighbouring points and this effect is attributed to non-uniformity of the target deposit where a small portion may be thick enough to contribute some resonance radiation with a larger cross section and a higher value of the ratio. In this case, the target was discarded and the measurement was repeated. The results are in general agreement with the measurements by Campbell (1956). The improved resolution of the larger detector used in the present investigation limits the errors due to uncertainty in the line shape of the two γ -rays and allows the ratio to be measured directly without reference to measurements by other workers.

At the 441 keV resonance, the value of 2.3 ± 0.04 is higher than values reported by other workers using pair spectrometers (Table 1), but, since those measurements were made with thicker targets, a small contribution from the non-resonant radiation would tend to reduce the value.

Above 800 keV, the ratio remained constant at 0.54 ± 0.08 and no departures from this value were observed at the 1030 keV resonance.

Measurements of the angular distributions of the two γ -rays have shown the intensity ratio to be in addition a function of the angle of observation above and below the 441 keV resonance and in the neighbourhood of the 1030 keV resonance and is the subject of further investigation.

The author wishes to thank Professor E. W. Titterton for his interest in the programme and the Australian Atomic Energy Commission for a grant which made the work possible.

References

- BONNER, T. W., and EVANS, J. E. (1948).—*Phys. Rev.* **73**: 666.
CAMPBELL, J. G. (1956).—*Aust. J. Phys.* **9**: 156.
DEVONS, S., and LINDSEY, G. R. (1950).—*Proc. Phys. Soc. Lond. A* **63**: 1202.
KOCKUM, J., and STARFELT, N. (1959).—*Nucl. Instrum.* **4**: 171.
KRAUS, A. A. (1954).—*Phys. Rev.* **93**: 1308.
PRICE, P. C. (1954).—*Proc. Phys. Soc. Lond. A* **67**: 849.
STEARN, M. B., and McDANIEL, B. D. (1951).—*Phys. Rev.* **82**: 450.
WALKER, R. L., and McDANIEL, B. D. (1948).—*Phys. Rev.* **74**: 315.

NOTICE TO CONTRIBUTORS

1. **GENERAL.**—Papers will be considered for publication irrespective of the organization to which the authors are attached. Intending contributors, in preparing papers for submission, should follow the general style adopted in this Journal. A "Guide to Authors" may be obtained on application to the Editor.

Papers, which should be written as concisely as possible, should be double-space typed on one side of the paper only and with liberal side margins. Every page, including those carrying tables and illustrations, should be numbered. Lengthy manuscripts should be accompanied by a table of contents with headings appropriately numbered. The organization to which the author is attached should be indicated in a footnote.

The original typescript and one carbon copy should be forwarded.

2. **SUMMARY.**—A short summary, which may be paragraphed, should precede the introduction to the paper. It should be of an informative character and written in such a way that it can be used by abstracting journals without amendment.
3. **REFERENCES.**—References are to be cited in the text by the year of publication, e.g. Thomson (1948), and are to be arranged alphabetically, giving the author's name and initials followed by the year of publication, title of the paper (if desired), title of the periodical, volume, and pages, thus:

Thomson, G. P. (1948).—*Proc. Phys. Soc. Lond.* **61**: 403-16.

Abbreviations of titles of periodicals should conform to those used in "A World List of Scientific Periodicals".

4. **ILLUSTRATIONS.**—Line drawings should be made with Indian ink on white drawing paper (preferably bristol board), tracing paper, or graph paper. Only blue or very pale grey ruled graph paper should be used as yellow, green, and red lines are difficult to screen out. Blue liner should not be used. Lines should be sufficiently thick and symbols sufficiently large to allow of reduction to a page size of $7\frac{1}{2}$ by 5 in. (or less). It is suggested that figures be drawn approximately twice the width at which they are to be printed. Lettering and numbering should only be pencilled on the drawings as the appropriate type will be substituted before the blocks are made. Original drawings should be submitted but, where possible, photographic copies or blue-prints of the originals should also be forwarded.

Half-tone photographs, which should be included only where essential, should be on glossy paper and show as much contrast as possible.

5. **REPRINTS.**—Individual authors receive 40 copies of each paper free, two authors receive 30 each, and three or more authors receive 20 each, but additional copies may be purchased.

CONTENTS

PAGE

| | |
|---|-----|
| Measurements of $n\gamma$ Coincidences in the Reaction $^{10}\text{B}(d,n\gamma)^{11}\text{C}$. By J. A. McDonell, D. G. Sargood, J. R. Moroney, and J. R. Prescott .. | 99 |
| Alpha-particles from the Reaction $^7\text{Li}(p,\gamma)^8\text{Be}(\alpha)^4\text{He}$. By D. S. Gemmell | 116 |
| Measurements of Changes in the Phase Path of Radio Waves reflected from the Ionosphere at Normal Incidence. By R. W. E. McNicol and J. A. Thomas | 120 |
| Experimental Relations Between Ionospheric True Height, Group Height, and Phase Height. By J. A. Thomas and R. E. W. McNicol .. | 132 |
| The Lifetime and Cell Size of the Granulation in Sunspot Umbrae. By R. E. Loughhead and R. J. Bray | 139 |
| The Characteristic Electron Energy Loss Spectra of Aluminium-Magnesium and Aluminium-Copper Alloys. By C. J. Powell | 145 |
| Ionospheric Refraction in Radio Astronomy. I. Theory. By M. M. Komesaroff | 153 |
| Hyperfine Structure in the Microwave Spectrum of Water. II. Effects of Magnetic Interactions. By D. W. Posener | 168 |

Short Communications

| | |
|---|-----|
| Cross Sections for the Interaction of 14.5 MeV Neutrons with Manganese and Cobalt. By E. Weigold | 186 |
| A Relation Between Ionospheric Drifts and Atmospheric Dynamo Current Systems. By L. H. Heisler | 188 |
| Comment on Multilayer Dielectric Filters. By H. L. Armstrong .. | 192 |
| On the Flow and Exchange Diffusion of Electrons and Negative Ions Formed by Molecular Attachment. By W. G. Kauman .. | 193 |
| Magnetic Anisotropy of Dispersed Powders. By F. D. Stacey .. | 196 |
| Electron Background in Nuclear Emulsions. By V. D. Hopper and Jean E. Laby | 202 |
| Relative Intensity of the 17.2 and 14.3 MeV Gamma Rays from the $^7\text{Li}(p,\gamma)^8\text{Be}$ Reaction. By B. Mainsbridge | 204 |